Technical Note N- 1113

THE SPHERICAL ACRYLIC PRESSURE HULL FOR HYDROSPACE APPLICATION; PART II - EXPERIMENTAL STRESS EVALUATION OF PROTOTYPE NEMO CAPSULE

By

J. D. Stachiw and K. L. Mack

October 1970

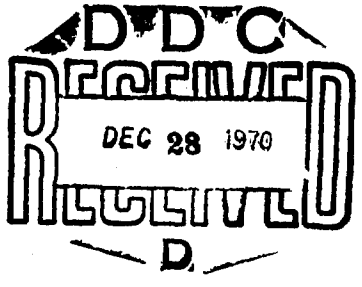

NAVAL CIVIL ENGINEERING LABORATORY
Port Hueneme, California 93041

'70

THE SPHERICAL ACRYLIC PRESSURE HULL FOR HYDROSPACE APPLICATION; PART II EXPERIMENTAL STRESS EVALUATION OF PROTOTYPE NEMO CAPSULE

Technical Note N- 1113

YF 38.535.005.01.006

by

J. D. Stachiw and K. L. Mack

ABSTRACT

The prototype 66-inch diameter spherical hull of NEMO* with 2.5 inch wall thickness has been subjected to a series of hydrostatic tests under simulated hydrospace environment to determine its structural integrity. After repeated long term and cyclic tests in the 220 to 2400 foot depth range, the hull was tested to implosion at 4150 feet. The magnitude of strains measured on the hull during cyclic and long term loadings, as well as the short term implosion depth of 4150 feet indicate that the hull satisfies the 1000 foot design depth requirement and can be without any further tests incorporated into any man-rated system approved for operation in the 0 to 600 foot depth range.

* Naval Experimental Manned Observatory

BLANK PAGE

INTRODUCTION

A spherical acrylic plastic capsule (Figure 1) has been developed[1] to serve as a pressure resistant hull in a manned observatory (Figure 2) for conducting underwater research and exploration along the continental shelf. The 66-inch external diameter spherical hull of the observatory was fabricated using twelve identical regular spherical pentagons of 2½ inch thick acrylic plastic, bonded together with an acrylic cement. The individual spherical pentagons were thermo-formed in an oven from flat commercial stock using a circular vacuum mold having the required spherical curvature, then machined to their proper shape and dimension, and, finally, annealed prior to assembly and bonding. Two openings of identical diameter were provided at opposite poles of the sphere. To allow entry to and exit from the interior of the sphere, a stainless steel hatch was inserted into the top opening of the sphere (Figure 3). A stainless steel plate mounted in the same manner as the hatch and 180° from it allows penetrations to be made into the hull to accomodate electrical and hydraulic connections.

One of the subjects to be investigated in the development of the capsule was the structural adequacy of the hull when subjected to water pressure and an upward buoyancy force resulting from its submergence to continental shelf depths. To this end, two studies were undertaken, one being a theoretical stress analysis[2] and the other being an experimental stress analysis. This report is concerned with the experimental stress analysis study of the prototype. The theoretical stress analysis and the comparison of experimental to theoretical stress values are discussed in a separate report.[3]

TESTING PROCEDURE

The hydrostatic pressure on the hull exterior due to its being lowered to various depths in the sea was simulated in the Laboratory's 72-inch diameter pressure vessel using seawater compressed by an electric motor-driven positive displacement pump. Prior to being placed in the pressure vessel, the hull was mounted inside a cage (Figure 4) on a support pedestal using brackets attached to the bottom steel plate (Figure 5). The cage offered protection to the test specimen during handling in and out of the pressure vessel. The support pedestal served not only to support the hull when it rested on deck but also served as an anchor to resist the 4,000 pound upward acting buoyancy force created by the hull's displacement in water.

The hydrostatic test program, which took approximately fifty days to complete, was divided into six phases (Table 1), each phase

following the other in consecutive order. All phases of the test were completed before the prototype acrylic plastic capsule was tested to implosion inside the pressure vessel. The first five test phases that underlie the experimental stress analysis are:

Phase I consisted of a series of eight tests performed in uninterrupted sequence with the hull in the vessel. For the first test, hydrostatic pressure was applied at the rate of 100 psi/min until 100 psi pressure was reached, stopping at every 50 psi interval to take strain readings. Approximately 90 seconds were required for strain recording and balancing unit to record in digital form - 87 channels of strain data. Upon reaching 100 psi, the pressure was held constant for 24 hours. During the first hour, strain and pressure readings were taken every ten minutes. Thereafter, strain and pressure readings were taken only hourly for the remaining 23 hours. The pressure was then dropped to 0 psi at a rate of 100 psi/min. During the depressurizing cycle, pressure and strain readings were taken at 50 psi intervals. When 0 psi was reached, strain gage readings were taken every ten minutes during the first hour that the pressure was zero, and, then, hourly until strain relaxation ceased. This was considered to have occurred when the strain rate decreased to a value of 50 micro inches/inch or less in a 12 hour period. For the succeeding seven tests, the hull was successively subjected to maximum pressures of 200, 300, 400, 500, 600, 700 and 800 psi, repeating the above noted procedure used for the 100 psi maximum pressure test.

Phase II of the testing program was made up of a series of five identical tests, each test following the other in a fixed sequence. Hydrostatic pressure was applied to the exterior of the hull at a rate of 100 psi/min until a pressure of 500 psi was reached. Pressurization was stopped momentarily at each 100 psi level at which time strain gage readings were taken. Once the 500 psi level was reached, the pressure was held constant for a period of 6 hours during which strain gage readings were taken every 10 minutes during the first hour and every hour for the remaining 5 hours. The pressure was then dropped to 0 psi at a rate of 100 psi/min. The depressurization was stopped momentarily at each 100 psi interval to allow strain gage readings to be taken. Once 0 psi was reached, strain gage readings were taken every 10 minutes during the first hour and then hourly for the period of 18 hours. At the end of the 18 hour period, the test cycle was repeated. After the fifth test cycle was completed, the hull was allowed to relax in the vessel for about 3 days before Phase III of the test program was begun.

Phase III of the test program consisted of a series of consecutively-run pressure cycles. All five cycles of Phase III test series were completed in one day. During each cycle the hull was pressurized to 500 psi at a 100 psi/minute rate. At 100 psi intervals the pressurization

Table 1. SUMMARY OF TESTS FOR EXPERIMENTAL STRESS EVALUATION

Pressure Range psi	Test Designation	Duration of Loading	Duration of Relaxation
Phase I			
0-100	I-1	24 hours	70 hours
0-200	I-2	24	72
0-300	I-3	24	44
0-400	I-4	24	45
0-500	I-5	24	96
0-600	I-6	24	188
0-700	I-7	24	144
0-800	I-8	24	275
Phase II			
0-500	II-1	6	18
0-500	II-2	6	18
0-500	II-3	6	18
0-500	II-4	6	18
0-500	II-5	6	66*
Phase III			
0-500	III-1	1	1
0-500	III-2	1	1
0-500	III-3	1	1
0-500	III-4	1	1
0-500	III-5	1	1
			60*
Phase IV			
0-500	IV-1	15 min.	15 min.
0-500	IV-2	15	15
0-500	IV-3	15	15
0-500	IV-4	15	15
0-500	IV-5	15	15
0-500	IV-6	15	15
0-500	IV-7	15	64*

Table 1. (cont'd)

Pressure Range psi	Test Designation	Duration of Loading	Duration of Relaxation
Phase V			
0-500	V-1	2	2
0-500	V-2	2	2
0-500	V-3	2	2
0-500	V-4	2	2
0-500	V-5	2	2
0-500	V-6	2	2
0-500	V-7	2	2
0-500	V-8	2	2
0-500	V-9	2	2
0-500	V-10	2	2
0-500	V-11	2	2
0-500	V-12	2	2

* Time elapsed from the end of one phase to the beginning of the next phase, hours.

was stopped and strain gage readings were taken. The pressure was held constant at 500 psi for one hour. Strain gage readings were taken every 10 minutes. The pressure was then dropped to 0 psi at 100 psi/min. Depressurization was interrupted and strain gage readings were taken at 100 psi intervals. The relaxation period lasted one hour at which time strain gage readings were taken every 10 minutes.

This procedure was repeated until all 5 cycles had been completed. A period of 60 hours was allowed to elapse after completion of the Phase III test before the Phase IV series of tests were begun.

Phase IV of the test program was accomplished with seven identical consecutively-run tests and took approximately one day to complete. Again, the exterior of the hull was pressurized from 0 psi to 500 psi at a rate of 100 psi/min. As in previous phases, strain gage readings were taken at each 100 psi interval. The pressure was held constant at 500 psi for a period of 15 minutes, with strain gage readings being taken every 5 minutes. The pressure was then released and allowed to return to 0 psi, with strain gage readings being taken at each 100 psi level as before. Zero pressure was maintained for 15 minutes during which time strain gage readings were taken every 5 minutes prior to beginning the next identical test cycle. After the series of seven test cycles were completed, the hull was then allowed to relax in the closed vessel at atmospheric pressure for 64 hours before commencing Phase V of the test program.

Phase V consisted of twelve identical consecutively-run tests which took approximately one day to complete. Hydrostatic pressure was applied to the exterior of the hull at a rate of 100 psi/min until a pressure of 500 psi was reached. Pressurization was stopped momentarily at each 100 psi level to allow strain gage readings to be taken. The 500 psi pressure was held approximately 2 minutes. After strain gage readings were made the pressure was dropped to 0 psi at a rate of 100 psi/min. At each 100 psi drop in pressure, the pressure was held constant to allow strain gage readings to be taken. Upon reaching 0 psi the hull was permitted to relax for 2 minutes during which strain readings were taken. After 2 minutes of relaxation, the next cycle was begun. After completion of 12 cylces the hull was allowed to relax at psi pressure for 48 hours with strain gage readings being taken hourly.

After completion of the five test phases, the hull was removed from the pressure vessel, the strain gage leads were retraced to confirm their locations, and the hull examined for cracks, joint irregularities, and inclusions. Before and during all phases of the test, the interior of the hull was vented to the atmosphere, and the temperature inside and outside the pressure vessel as well as that inside and outside of the hull was stabilized to and maintained between 68°F and 70°F.

Phase VI. After extensive inspection of the hull, it was subjected to many other hydrostatic tests (Table 2). Since no strain readings were taken during Phase VI tests, they are not discussed in this report. (For detailed discussion of these tests see Reference 1). Only the last test during which the hull was pressurized to implosion is discussed in this report as it substantiates some of the findings made solely on the basis of experimental stress analysis.

INSTRUMENTATION

The hull was instrumented using SR-4, type FAER-50D-12S13L, strain gages attached to the surfaces of the hull with epoxy Epy-150. Budd's Gagecoat #2 and #5 were used to waterproof the gages. Three strain gages wired independently and placed in the configuration of a wye constituted a rosette. A total of 29 rosettes were used to instrument the hull (Figure 6), giving a total of 87 channels of readout. Seven rosettes were placed on the bottom stainless steel plate, four being placed on the interior surface and three being placed on the exterior surface (Figure 7). A total of 22 rosettes were placed on the acrylic plastic portion of the hull, eight being located on the interior surface and fourteen on the exterior surface of the hull. Most of the rosettes placed on the exterior surface of the hull had a corresponding rosette oppositely placed on the interior surface (Figure 8). In order to have a common base of reference so that a comparison may be made in the future between the theoretical analysis and experimental results, all of the rosettes were mounted along the same meridian line at points whose relative position with respect to the polar axis of the capsule was recorded in degrees of latitude. One of the legs of the wye making up a rosette was always placed on this meridian line, and the individual strain gage readings at any particular rosette location were always taken in the same given order and referenced to this meridian mounted strain gage to insure proper interpretation of the strain gage readings. The rosettes were numbered beginning with number one at the bottom stainless steel plate (Figure 9) and extended through number eighteen near the top of the hull. As a further identification as to location, rosettes mounted on the exterior surface of the hull were assigned the letter A following their number while those rosettes mounted on the interior surface of the hull have the letter B following their number. The thickness and sphericity of the hull at each rosette and the location of each rosette with respect to a joint were also recorded to aid in subsequent reduction of strain data (Figure 10).

Leads from a thermocouple and the strain gages mounted inside the hull were led to watertight bulkhead connectors which screwed into threaded holes provided for that purpose in the bottom stainless steel plate. After passing through the bottom stainless steel plate (Figure 11), these leads together with those from the exterior gages and a thermocouple inside the pressure vessel were connected to a penetrator assembly in the pressure vessel's head (Figure 12) which allowed passage

Table 2. MISCELLANEOUS TESTS CONDUCTED ON NEMO
AFTER CONCLUSION OF EXPERIMENTAL STRESS ANALYSIS TESTS

Number of Tests	Maximum Pressure (psi)	Duration of Sustained Loading	Temperature (°F)	Damage Observed
1	250	6 hours	68 - 70°F	None
1	500	6 hours	68 - 70°F	None
1	750	6 hours	68 - 70°F	None
1	500	4 hours	38°F	None
1	600	7 hours	36°F	None
1	700	5.5 hours	43°F	None
1	750	8 hours	42°F	None
1	850	8 hours	41°F	None
20	500	4 hrs. per test	32 - 75	None
15	550	1 hr. per test	32 - 40	None
13	550	0.5 hr. per test	32 - 40	None
11	500	1 minute per test	32 - 40	None
1	1070	10 minutes	34	None
1	1850	None	70	Gen. Implosion

of the leads out of the pressure vessel to a 90 channel multiple digital strain indicator and digital temperature indicators (Figure 13).

To monitor leakage of water into the interior of the hull, a 0.250 inch diameter copper tube was inserted through the bottom stainless steel plate flush with the plate's inside surface and sealed against water pressure with an epoxy compound. The tube was connected to a fitting in the vessel head penetrator assembly from where it was connected to an empty graduate. Since the graduate was open to the atmosphere, the atmospheric pressure prevailed at all times in the interior of the acrylic plastic hull. Only once a day when the hull was under pressure, air at a pressure of about 10 psi was introduced into the tube and, consequently, into the interior of the hull. The air pressure was held momentarily after which it was released. The pressurized air was then allowed to escape from the interior of the hull through the tube. The air ejected any water accumulated in the hull ahead of it. Any water forced out of the hull was collected in a graduate and its amount recorded. The amount of water leakage averaged about 5 quarts per day and was caused by an improperly molded plastic penetrator located in the bottom stainless steel plate. The faulty penetrator was not replaced during the testing program as the penetrator would also require the replacement of the custom made cable whose procurement time was approximately 6 months. There was no evidence of leakage from any other source.

Periodically the NEMO capsule was removed from the pressure vessel and inspected for any indications of damage like local yielding or cracking of hull material. Some selected locations on the hull were also photographed each time for later reference.

REDUCTION OF DATA

For any combination of stresses at a point in a stressed body, three mutually perpendicular planes passing through the point can be found on which only normal stresses exist; the normal stresses on these planes on which there are no shearing stresses are called principal stresses. There exist two types of stress fields when one considers the hollow spherical shape. On the interior surface only two principal stresses are present creating what is called a biaxial stress condition. However, on the exterior surface a state of triaxial stress is found.

Biaxial Principal Stresses

The two dimensional stress field was assumed to consist of normal stresses, σ_1, σ_2, at right angles to each other. The third stress, σ_3, is zero since there is no internal or external pressure being exerted at right angles to the plane on which the strains are being measured.

Rosettes in a wye configuration were used to measure the strains on the interior and exterior of the acrylic hull, as mentioned earlier. The strain readings were designated ε_a, ε_b, and ε_c, where ε_a was always

oriented along the meridian on the sphere.

The maximum and minimum principal strain were found by using the conventional Mohr circle theory and the three strain gage readings ε_a, ε_b, and ε_c.

$$\varepsilon_{\substack{max \\ min}} = \frac{\varepsilon_a + \varepsilon_b + \varepsilon_c}{3} \pm \sqrt{\left(\varepsilon_a - \frac{\varepsilon_a + \varepsilon_b + \varepsilon_c}{3}\right)^2 + \left(\frac{\varepsilon_b - \varepsilon_c}{\sqrt{3}}\right)^2} \qquad \text{(Eq. 1)}$$

The stresses were calculated using E, the modulus of elasticity, and μ, Poisson's ratio:

$$\sigma_{max} = \frac{E}{1 - \mu^2}\left(\varepsilon_{max} + \mu\varepsilon_{min}\right) \qquad \text{(Eq. 2)}$$

$$\sigma_{min} = \frac{E}{1 - \mu^2}\left(\varepsilon_{min} + \mu\varepsilon_{max}\right) \qquad \text{(Eq. 3)}$$

The angle was measured from the meridional axis to the axis along which the maximum principal strain was oriented.

$$\theta = \frac{1}{2}\tan^{-1}\frac{\frac{1}{\sqrt{3}}\left(\varepsilon_b - \varepsilon_c\right)}{\varepsilon_a - \left(\frac{\varepsilon_a + \varepsilon_b + \varepsilon_c}{3}\right)} \qquad \text{(Eq. 4)}$$

This angle lies in the plane of the sphere's surface.

Triaxial Principal Stresses

On the exterior surface of the sphere the third principal stress, σ_3, is not zero, thereby creating a triaxial stress condition. The stress, σ_3, represents the hydrostatic pressure being applied to the hull. This stress generates a radial strain, but its magnitude cannot be measured on the sphere's surface by conventional strain gages as they lie in a plane at right angle to the radial strain. Although the magnitude of the radial strain cannot be measured, the magnitude of the stress causing the radial strain is known, as it is numerically equal to the external hydrostatic pressure. Thus, it is possible to calculate the magnitude of the three principal stresses if the two principal strains on the external surface of the sphere and the radial stress are known.

Using the system of three equations that describe the relationship between three principal stresses in the three dimensional stress field

$$\sigma_1 = \frac{E}{(1+\mu)(1-2\mu)} \left[(1-\mu)\,\varepsilon_{max} + \mu\,(\varepsilon_{min} + \varepsilon_3)\right] \qquad \text{(Eq. 5)}$$

$$\sigma_2 = \frac{E}{(1+\mu)(1-2\mu)} \left[(1-\mu)\,\varepsilon_{min} + \mu\,(\varepsilon_{max} + \varepsilon_3)\right] \qquad \text{(Eq. 6)}$$

$$\sigma_3 = \frac{E}{(1+\mu)(1-2\mu)} \left[(1-\mu)\,\varepsilon_3 + \mu(\varepsilon_{max} + \varepsilon_{min})\right] \qquad \text{(Eq. 7)}$$

and the values of ε_{max} and ε_{min} calculated (Equation 1) from strains measured on the surface of the sphere the values of σ_1, σ_2, and σ_3 have been calculated. In the equations above σ_1 and σ_2 denote principal stresses in the plane of the sphere's external surface, while σ_3 represents the principal stress at right angle to the plane in which σ_1 and σ_2 are acting.

Shear Stresses for Biaxial and Triaxial Loadings

The evaluation of shear stress in the triaxial loading condition was accomplished by using the octahedral shearing stress theory. It is possible by using Mohr's circle to resolve a system of three dimensional stresses into two systems acting on the eight octahedral planes. One system is represented by shearing stresses τ_G, and the other by equal normal stresses σ_G.

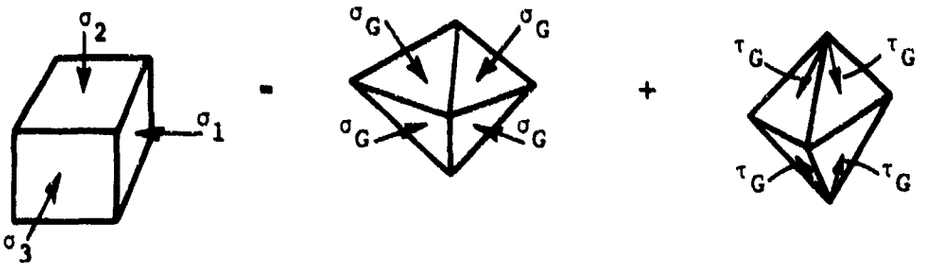

It is postulated that the equal compressive (or tensile) stresses, σ_G, do not initiate yielding of the material but may produce fracture. Therefore, the octahedral shearing stresses are assumed by this theory to be entirely responsible for initiation of yielding in the material. The octahedral shear theory postulates further that yielding at any point in a body under any combination of stresses is initiated only when the octahedral shearing stress τ_G becomes equal to $\sqrt{2}/3\ \sigma_y$, where σ_y is

the tensile or compressive elastic strength of the material as determined by the standard uniaxial test. This value can be found by having a uniaxial stress condition in which $\sigma_2 = \sigma_3 = 0$ (Equation 8). The octahedral shearing stress on each octahedral plane may be expressed:

$$\tau_G = \pm \frac{1}{3} \sqrt{(\sigma_1 - \sigma_2)^2 + (\sigma_2 - \sigma_3)^2 + (\sigma_3 - \sigma_1)^2} \qquad \text{(Eq. 8)}$$

where σ_1, σ_2, and σ_3 are the three principal stresses determined by Equations (5, 6, 7, 8).

The evaluation of shear stress in the biaxial loading condition was accomplished by Mohr's circle. The maximum shear stress was calculated using the Mohr circle:

$$\tau_{max} = \frac{\sigma_1 - \sigma_2}{2} = \frac{\sigma_{max} - \sigma_{min}}{2} \quad \text{where } \sigma_{max} \text{ and } \sigma_{min} \text{ are} \qquad \text{(Eq. 9)}$$

obtained from Equations (2) and (3).

In the calculation of stress values under both the biaxial and triaxial states of stress the modulus of elasticity, E, and Poisson's ratio, μ, were assumed to be 4.5×10^5 psi and 0.35 for the acrylic and 28×10^6 psi and 0.26 for the steel, respectively. The properties of both materials are described at length in Reference 1. It suffices here to state that the yield point of 316 Type stainless steel is in 25,000 - 30,000 psi range while for Plexiglas G acrylic plastic under short-term loading it is 10,000 psi. The strain readings from each rosette were converted to principal strains, principal stresses and octahedral shear stresses by means of an IBM 1620, Model 2 computer.

Since the reduction of all the experimental data into principal stresses and shear stresses would be too voluminous for inclusion into the report and because the validity of some calculated stresses (under long-term creep for example) is doubtful because of necessary simplifications in assumptions underlying the analytical calculations, all experimental data was chosen for reduction to principal strains, but only some for reduction to stresses.

The data that was chosen for reduction to stresses pertained only to short-term loading conditions when NEMO was pressurized repeatedly to 100, 500, and 800 psi sustained pressure levels (Phase I tests Nos. 1, 5, and 8). The reasons for choosing only these test conditions are:

1. Equations (2) through (8) describe accurately only the behavior of isotropic materials in the linear range of elastic deformations. Since the deformation of acrylic plastic can be postulated to represent that of an isotropic material in the linear portion of the elastic strain range only under short-term loading at stress levels less than 8000 psi

calculations of stresses in NEMO under short-term hydrostatic loading can be considered reasonably accurate. The visco-elastic and visco-plastic behavior of the material with the associated time dependent change of modulus of elasticity and Poisson's ratio makes the calculation of stresses in NEMO under long-term loading a very complex operation beyond the scope of this report.

2. The 100, 500, and 800 psi short-term loadings were chosen for calculation of stresses because they represent the minimum, proof and 200% overload test conditions. During the pressurization to the 100 psi pressure level, the lowest sustained pressure loading to which NEMO was subjected, the distribution of stresses (Figures 14a, 15a, 15b, 16a, and 16b) is probably indicative of the true elastic conditions as the stress levels are so low that virtually no visco-elastic or visco-plastic deformations would have been present. The stresses, on the other hand, found during the loading to the 500 psi pressure level are of interest (Figures 14b, 15a, 15b, 17a and 17b) as a comparison between them and those generated by the test to the 100 psi pressure level will clearly show whether any serious yielding of the NEMO hull took place when it was subjected to the proof test. Finally, the stresses recorded during the loading to 800 psi level are important (Figures 14c, 15a, 15b, 18a-20d) because they should show some occurrence of yielding in the steel hatches, or the acrylic plastic material around them at this 200% overload level.

Other data that has been reduced to show only principal strains and is included in this report pertains to (1) sustained loading at 100, 200, 300, 400, 500, 600, 700, and 800 psi pressure levels (Figures 21a-24b),and (2) cyclic loading to 500 psi pressure level (Figures 25-32b). Since inclusion of graphs depicting this data for all of the rosettes would make this report too voluminous, some selectivity was exercised in the presentation of data. For some tests, like the long-term loading to 100, 500 and 800 psi pressure levels principal strains are shown for five rosettes while for the cyclic tests only summaries of the strain distribution and strains from the equatorial rosettes are shown (Figures 25-32).

Although the exclusion of most of the data generated during the hydrostatic testing of the NEMO capsule from this report makes it somewhat less than complete, it was felt that the data selected for inclusion in this report is more than sufficient to support the findings made in the report and that the inclusion of all the generated experimental data would only make the report unwieldly as in most cases the strains generated by the many rosettes in the cyclic and long-term tests were similar, if not identical, and thus most of the data would have been repetitive.

FINDINGS

Short-Term Loading

Acrylic Plastic. The stresses measured on the acrylic plastic hull (Figures 15 and 19) varied from one strain gage rosette to another depending on their location. For all rosettes on the acrylic plastic stresses were higher on the interior of the hull. At the equator of the hull maximum and minimum principal stresses in the plane of the hull's surface were approximately the same. As one progressed, however, from the equatorial rosettes to those located near the polar penetrations in the hull, the difference between maximum and minimum principal stresses in the plane of the hull's surface increased. At the edge of the penetration the highest principal stress was in the meridional direction and its magnitude on the exterior of the hull was approximately the same as the maximum principal stress at the equator, while the least principal stress was in the hoop direction and its magnitude was approximately 45 percent less.

The relationship between the hydrostatic pressure and stresses on the acrylic was linear and approximately the same for the short-term portions of all Phase I tests. This indicates that no yielding of the acrylic occurred under short-term loading at any of the locations where the strain gage rosettes were located even when the NEMO hull was hydrostatically loaded to 800 psi (Figure 19). At 500 psi the maximum principal stress recorded on the external surface in equatorial region was -3008 psi while on the interior it was -3423 psi. No higher stresses than 3423 psi were recorded at any other rosette location on the acrylic hull at 500 psi loading.

It is interesting to note that considerable shifting of principal stress directions occurred during short-term pressurization of the acrylic hull. The magnitude of direction shift varied from rosette to rosette, and from one pressure level to another. The major shifts occurred in the equatorial region while in the vicinity of the polar opening there was almost no change in direction of principal stress axis from one pressure level to another. This indicates that the steel plate presents such a major structural discontinuity with associated well defined stress field in the spherical hull that small changes in acrylic hull deflections are not able to change the orientation of the stress field significantly. This substantiates the findings made previously on 15-inch NEMO models that at the very edge of the penetration in acrylic the meridional stresses are substantially higher than hoop stresses and thus constitute a well defined stress pattern that minor readjustments in hull deflections cannot shift. The presence of major shifts in the principal stress axis orientation on the equatorial region indicates on the other hand that the magnitudes of both meridional and hoop stresses are so well matched that even a minor local change in hull deflections can radically change the direction of principal stress axis. It also shows that because the sphere is made up of 12 non-

identical structural modules the stresses will redistribute themselves in a stepwise manner as each increment in pressure will differently affect each pentagon and the interrelationship between them.

Steel. The stresses measured on steel surfaces of the NEMO hull were considerably higher than on acrylic surfaces. The highest stresses measured at 500 psi were on the interior of the steel plate at rosette locations #4 and #3. The direction of the -26,700 psi maximum principal stress at location #3 was in the meridional direction, while at location #4 the -24,050 psi maximum principal stress was in hoop direction. Although for rosettes #3 and #4 the relationships between hydrostatic pressure and stress were quasi-linear (Figure 20) for each of the individual short-term portions of Phase I hydrostatic tests, they were not identical. Thus, for example, in the Phase I-1 (0 to 100 psi) test the maximum principal stress at rosette #3 at 100 psi hydrostatic pressure was -11,790 psi, in the Phase I-5 (0 to 500 psi) test the same principal stress at 100 psi pressure was -8240 psi, while in the Phase I-8 (0 to 800 psi) test it became at 100 psi pressure -2580 psi. It thus appears that the stress magnitude for a given hydrostatic pressure level like 100 psi at rosette locations #3 and #4 progressively decreased from one hydrostatic test to another. After seven long-term tests the stress magnitude under 100 psi hydrostatic loading at rosette #3 was less than 25 percent of its value measured during the first test.

The reasons for this behavior are many and their inter-relationship not well understood. Three major factors are at work here that cause the stress-strain relationship of the steel bottom plate at locations #3 and #4 to change from one test to another.

Factor A is the change in relative position between the steel plate and the penetration in acrylic. During pressurization, the plate is forced deeper into the opening. Upon depressurization the surface friction between steel and acrylic does not often permit the steel plate to return to its original location in the opening. Because of this, the steel remains under compressive preload whose magnitude increases from test to test by approximately 100 microinches. Since in the calculation of stresses the strain reading at the beginning of each test is taken as the zero datum the determination of residual stresses after each test was not accomplished by comparing stresses from different tests but by comparing the magnitude of residual strains after completion of relaxation periods at the end of all Phase I tests (Figures 21 and 22) with the magnitude of residual strain at the completion of relaxation period following the long-term loading at 100 psi.

Factor B is plastic deformation of the acrylic at the very edge of the penetration. Its magnitude, and the pressure level at which it occurs, has not been accurately determined as no strain gages were located on the acrylic at the very edge of the penetration. Extrapolating the readings taken at rosette #18, the closest one to the edge, indicates that the first permanent set occurred at the edge of the penetration only after the Phase I-4 (0 to 600 psi) test.

the viscoelastic yield point at any of rosette locations so long as the duration of the individual loading cycle was equal to, or less than, 6 hours.

Steel. The strains measured on the steel plate did not change significantly from one pressure cycle to another, or from one cycling program to another. It is interesting to note, however, that the magnitude of strains in steel generated during the pressure cycling to 500 psi is noticeably less than the strains generated previously during the first short-term loading to 500 psi (Phase I-5). It is surmised that this has been caused by cold working the steel plate past its yield point, as well as plastically deforming the acrylic plastic hull adjacent to the steel plate during the long-term loading to 800 psi (Phase I-8).

Miscellaneous Loadings

After completing the test Phases I through V the NEMO hull was subjected to an assorted group of miscellaneous tests whose objectives were the determination of (1) displacement change during various kinds of hydrostatic loading, and (2) the rate of heat transfer from the interior of the hull when diving in waters with widely varying ambient temperatures. Since the findings of these tests were thoroughly discussed in another report[1] and since these tests have little bearing on the evaluation of the hull's structural adequacy, they will not be further discussed.

Destructive Testing

The final test in the structural evaluation program of NEMO hull #0 was the short-term implosion testing in which by the observation of fragments and magnitude of loading at which the failure took place some of the postulates formed during previous non-destructive testing could be confirmed or modified.

The implosion that occurred at 1850 psi under 50 psi/minute loading rate was of general, rather than local nature indicating that the ultimate strengths of the acrylic hull and the steel penetration closures were fairly well matched. This finding is supported by the fact that not only was the acrylic hull broken into several orange peel shaped fragments, but also that the metallic closures were severely dished in (Figure 33). If only the hull had failed, there would not have been any signs of concave dishing in on the initially convex closures as fragmentation of the sphere is incapable of producing such deformations in the metallic end-closures. If on the other hand the metallic end-closures alone had failed, general fragmentation of the hull would not have taken place but just some fracturing and spalling around the edges of the penetration in acrylic.

Since the hull was filled with water, that was vented to atmosphere during the implosion testing, a failed metal plate could not serve as a high-speed projectile that by impacting the interior of the acrylic hull would fracture it into many fragments.

The acrylic fragments resulting from the implosion were in the shape of orange peels with the fracture lines cutting in all cases across bonded joint lines. The ends of fragments that butted previously against the bottom steel plate (Figure 34) were severely spalled indicating serious deformation of the steel bearing surface at the time that the sphere imploded. The ends of fragments that butted against the top hatch ring did not show severe spalling but only radial in plane of hull racking (Figure 35). When one observes the deformed steel end-closures of the hull it becomes immediately very clear why only the acrylic bearing surface in contact with the bottom plate showed such extensive damage while the top one did not.

The deformation of the bottom plate was of such nature (complete reversal of spherical curvature) that the beveled bearing flange rotated (Figure 36) about its line of attachment to the dished head. The rotation of the flange caused it to bear extra hard on the inner half of the acrylic bearing surface while almost completely relieving the bearing stress against the outer half of the acrylic plastic bearing surface. The rotation of the flange was so large that the resulting bearing pressure on the inner half of the acrylic hull caused it to shear off at the bearing surface. The shearing plane formed approximately a 45° angle with the inner surface of the hull.

This was not the case with the upper steel closure. Although the hatch deformed severely like the bottom plate by completely reversing the curvature of the hatch the effect of this buckling process on the acrylic bearing surface was minimal. The reason for this difference is that the hatch ring between the deforming hatch and the acrylic bearing surface formed a rigid barrier which the buckled hatch could not deform. Thus, the acrylic bearing surface in contact with the hatch ring did not experience at any time the uneven bearing pressure that would be exerted by a rotating hatch flange if it was in contact with the acrylic bearing surface without the intervening hatch ring barrier.

The failure mode of the bottom plate also illuminates quite well the strain readings on it during the Phase I tests. The reason that rosette #3B recorded the highest strains on the plate becomes quite obvious. The rosette was mounted at the location where the plastic hinge for the dishing of the plate was located. Since the rosette #3B was on the compression side of the plastic hinge, the compressive flexure strains would be superimposed on the compressive membrane strains in the meridional direction to exceed the strains recorded at rosette 1A and B, 2A and B, and 4B. This is the location where probably yielding also took place first on the bottom plate, and only after formation of the plastic hinge did the plate flange rotate bringing uneven pressure to bear upon the acrylic bearing surface.

Tensile specimens were cut from the acrylic plastic hull fragments to establish the tensile strength of joints after the hull was subjected to the extensive hydrostatic testing program. The tensile strength of the PS-18 bonded joints was found to be in the same range (9220-7350 psi) as the strength of the PS-18 joints in test blocks (8280-5150 psi) tested immediately after fabrication of the NEMO hull #0. This substantiates the claim of the adhesive supplier that long-term submersion in seawater, as well as repeated compressive straining of joints bonded with PS-18, does not decrease its mechanical strength.

No evidence was found of cracks initiating at the many bubbles and discontinuities present in the bonded joints (Figure 37). This substantiates the postulate[1] made at the beginning of the program by the designers of NEMO hull that bubbles and other similar discontinuities in the joints will not act as sources of incipient cracks so long as the bonded joints have not been subjected to (1) tensile stresses, or (2) compressive stresses of such magnitude that plastic deformation of the joint filler material takes place (at approximately 15,000 psi compressive stress). Elimination of the bubbles and discontinuities in the joints is, however, a desirable objective for future NEMO hulls because (1) their presence is unsightly, (2) they may constitute a source of leakage, and (3) they restrict the use of NEMO hulls solely to external pressure loadings.

CONCLUSIONS

The hydrostatic testing program as well as the subsequent experimental stress analysis have conclusively shown that the prototype 66-inch OD x 61-inch ID Plexiglas G plastic NEMO hull #0 bonded with PS-18 adhesive and equipped with 316 Type stainless steel penetration closures has met the design objectives of (1) collapse depth in excess of 3000 feet, (2) design depth of 1000 feet, and (3) operational depth of 600 feet for manned dives.

RECOMMENDATIONS

1. Further experimentation should be conducted on bonding of spherical pentagons to obtain an adhesive system and bonding technique superior to the PS-18 bonding system so that less bubbles and discontinuities are present in the hull joints.

2. For diving operations in excess of 600 feet the Type 316 stainless steel should be replaced in penetration closures with Inconel 625 that has superior corrosion resistance and mechanical strength. If the cost of Inconel 625 end-closures proves to be excessive, SAE 4130 cadmium plated steel may be substituted for it providing the projected life of the system is short.

REFERENCES

1. J. D. Stachiw, "Development of a Spherical Acrylic Plastic Pressure Hull for Hydrospace Application," U. S. Naval Civil Engineering Laboratory, Technical Report R-676, April 1970.

2. R. C. DeHart, "NEMO Stress Analysis and Material Investigation," Technical Report Contract No. N00123-67-C-2123, Southwest Research Institute, San Antonio, Texas, March 1968.

3. H. Ottsen, "The Spherical Acrylic Pressure Hull for Hydrospace Application; Part III - Comparison of Experimental and Analytical Stress Evaluations for Prototype NEMO Capsule" (to be published by NCEL).

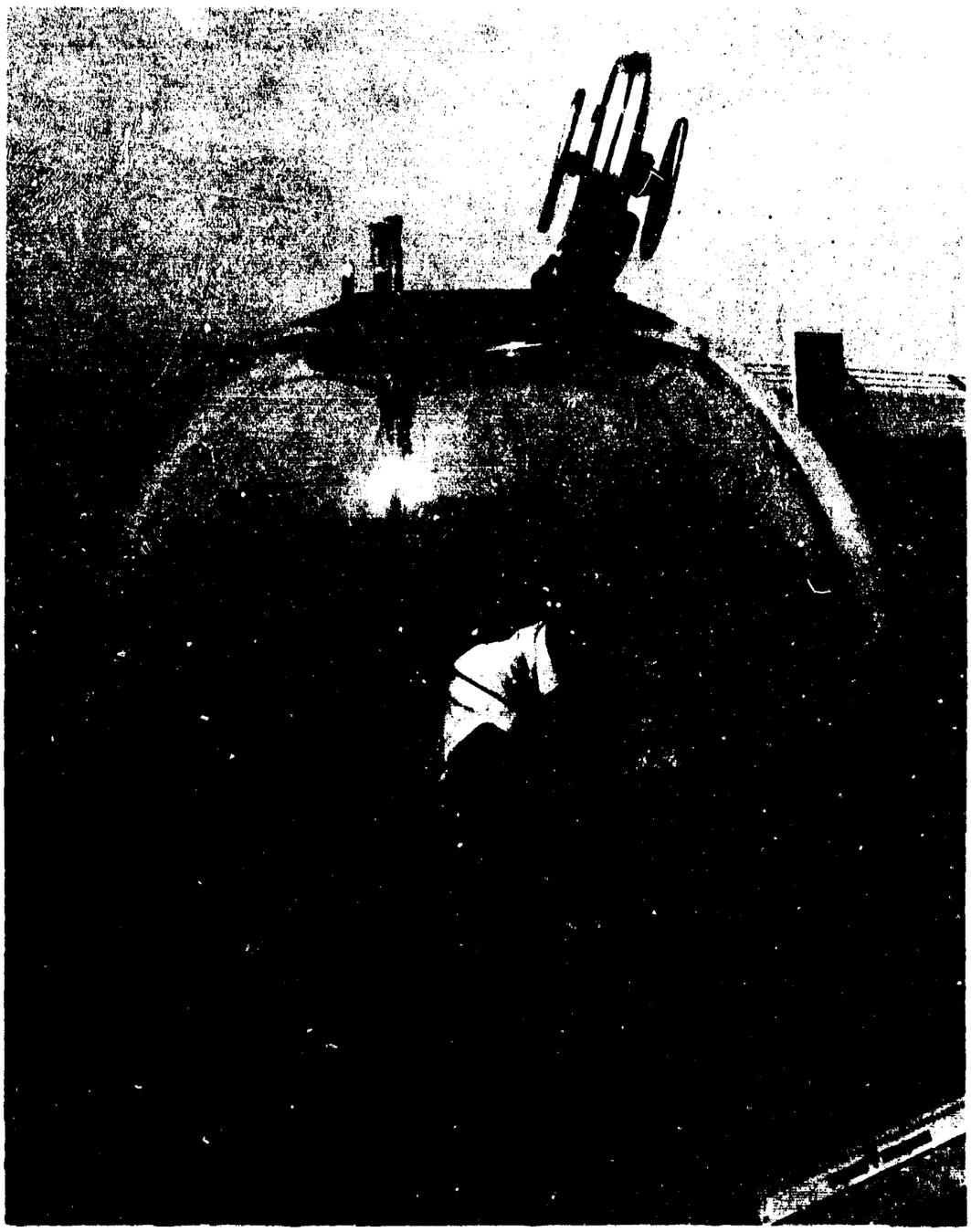

Figure 1. Prototype 66-inch OD x 61-inch ID acrylic plastic NEMO capsule.

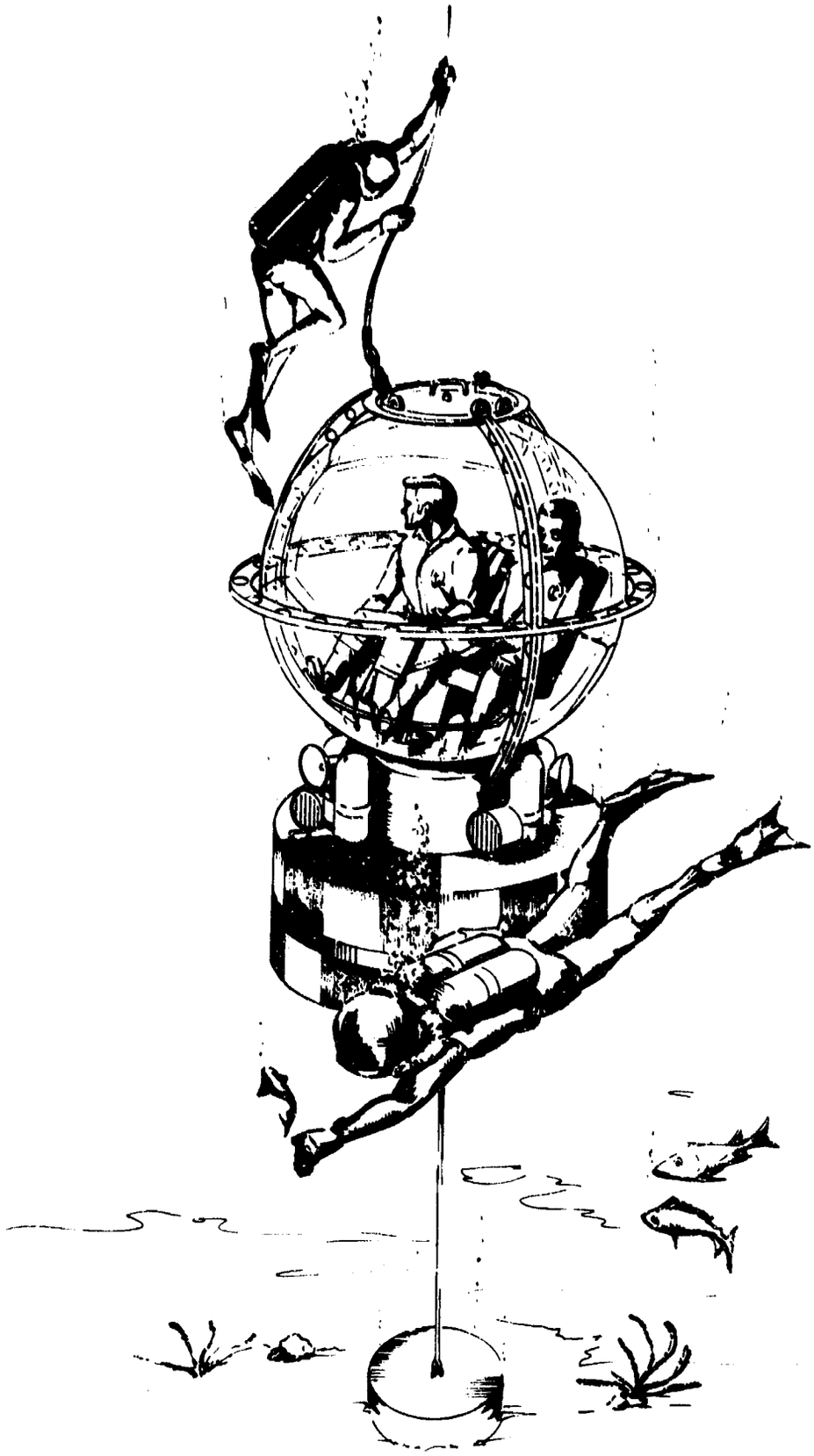

Figure 2. NEMO capsule in tethered self-winching diver control center.

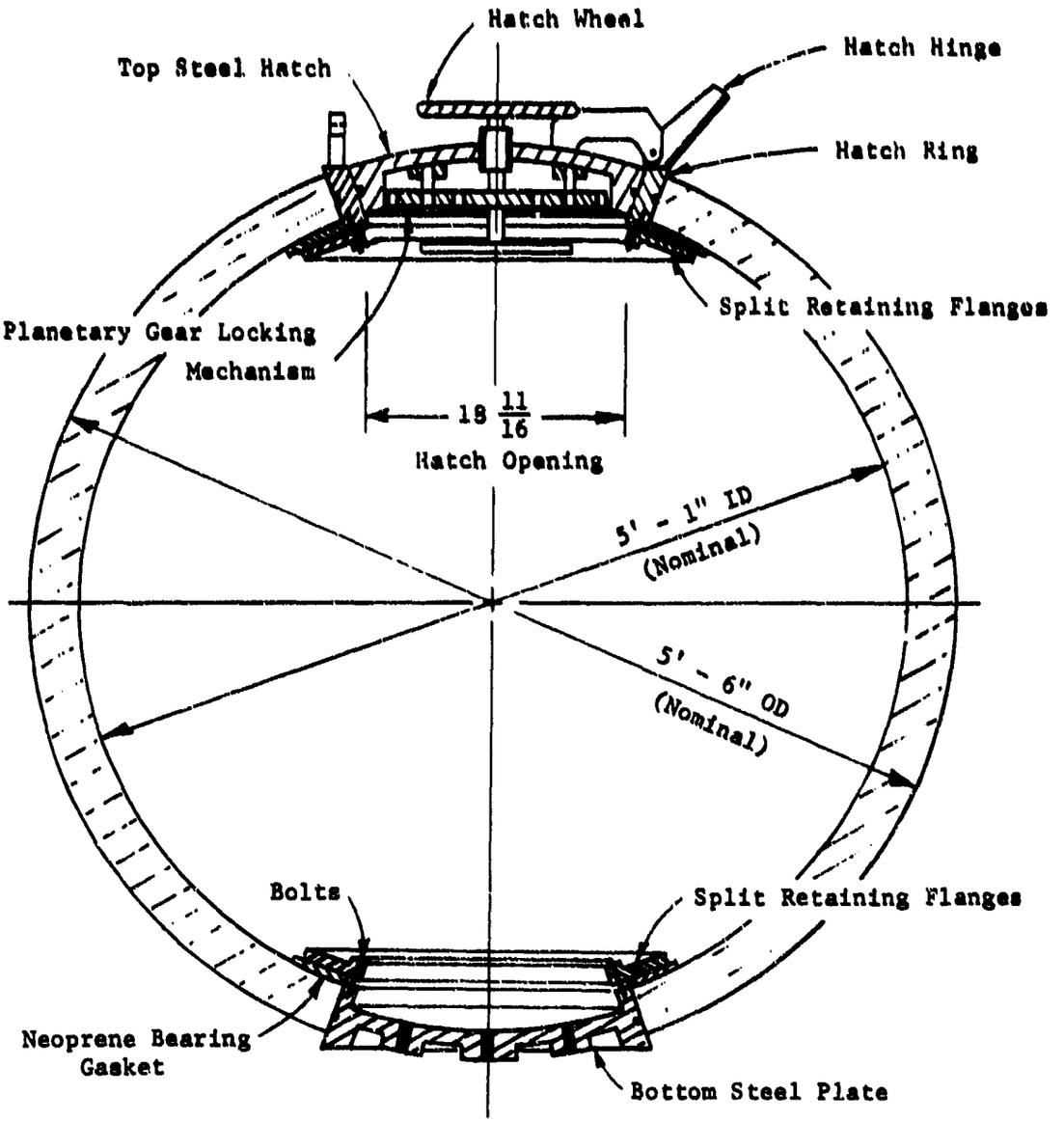

Figure 3. NEMO Hull Cross Section.

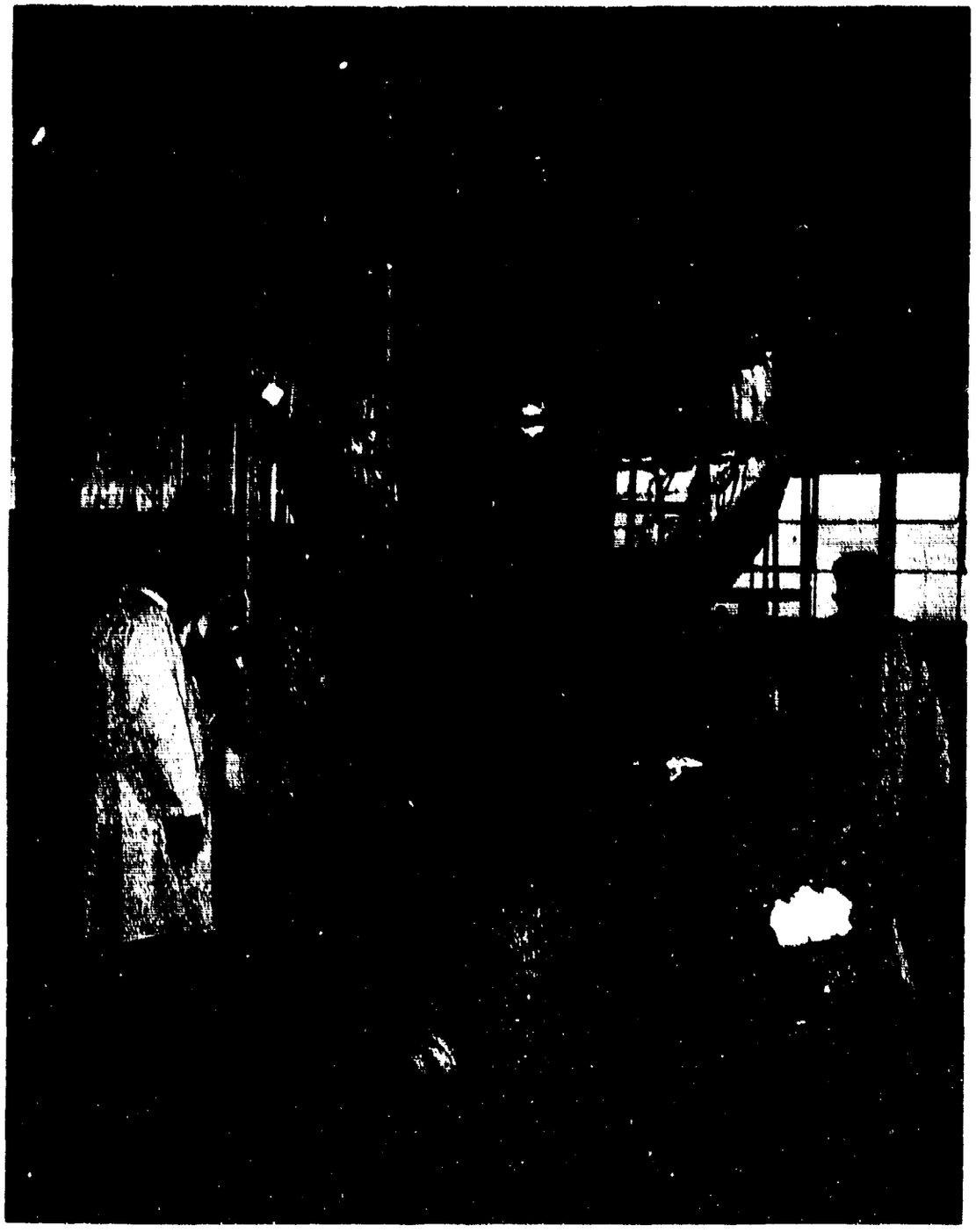

Figure 4. NEMO capsule being lowered into the Deep Ocean Simulation Facility pressure vessel; note the protective cage and support pedestal.

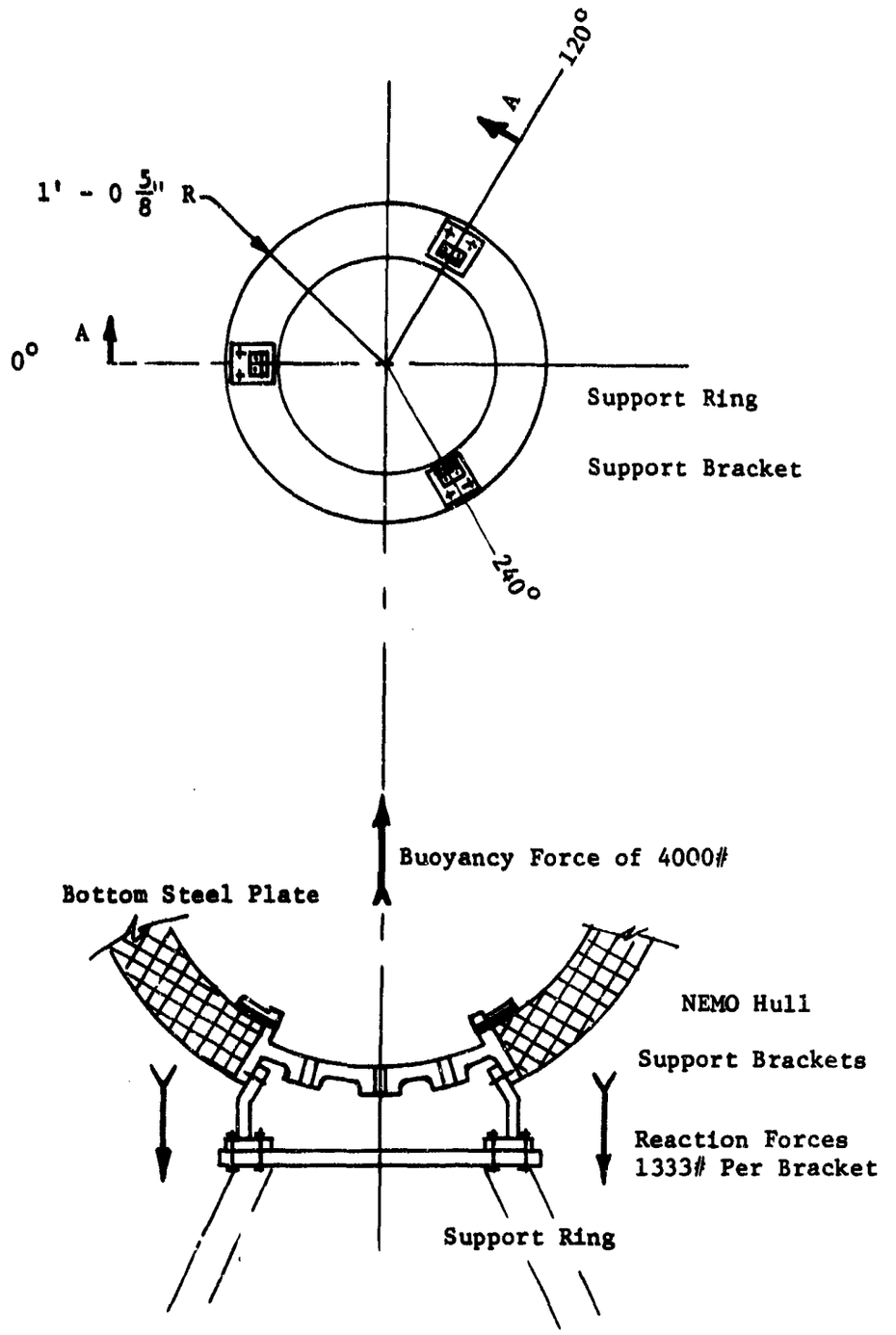

SECTION A-A

Figure 5. Method of attaching capsule's bottom steel plate to cage support pedestal.

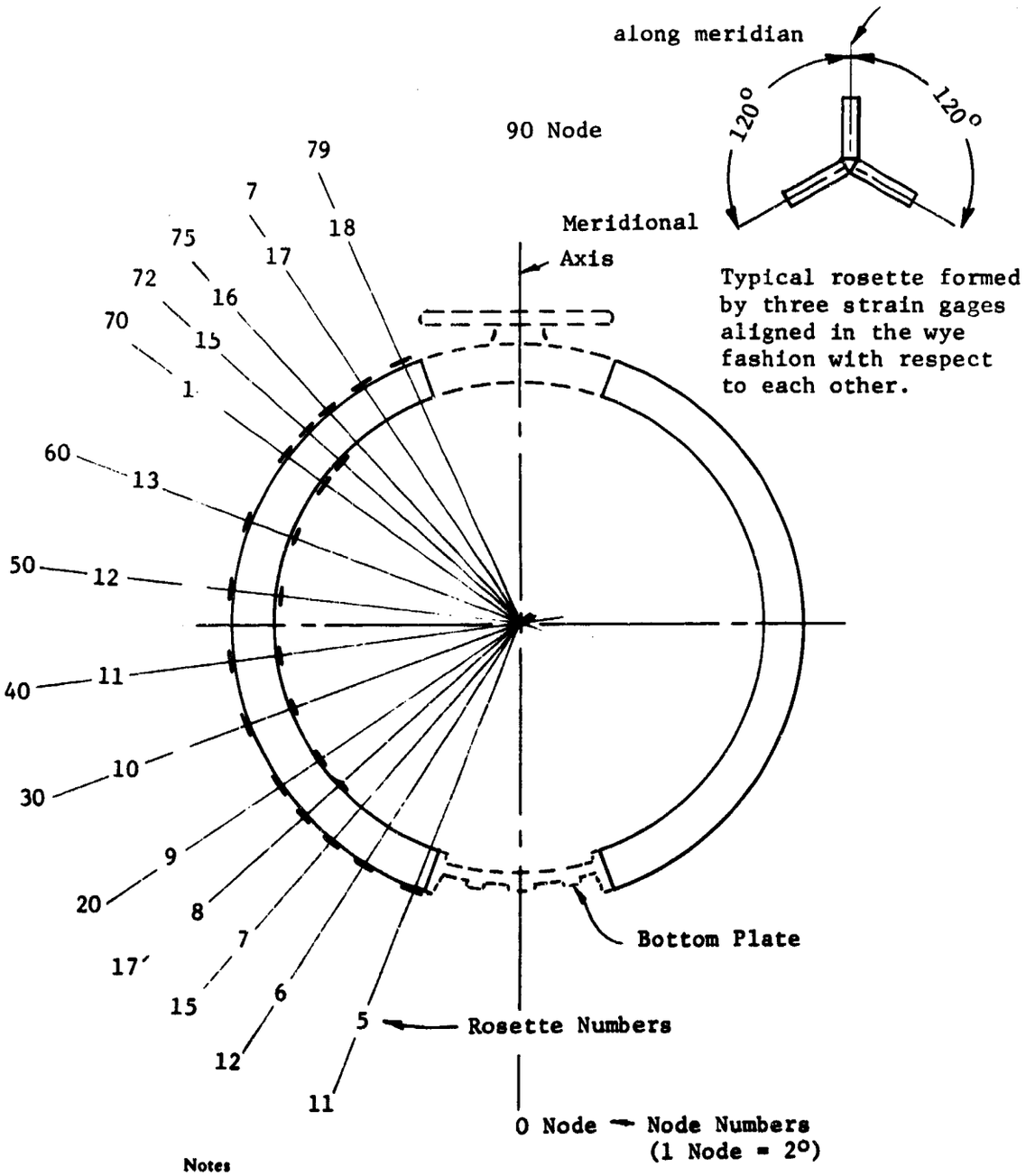

Notes

1. Rosettes on hull exterior have the Suffix A following the number. Likewise, interior rosettes have B for the Suffix. (e.g. 10A and 10B)

2. Node locations have been determined by dividing the sphere into 2 degree increments. Numbering of nodes began on the bottom just as the numbering of the rosettes and continues to the top.

Figure 6. Rosette locations on the acrylic portion of the capsule.

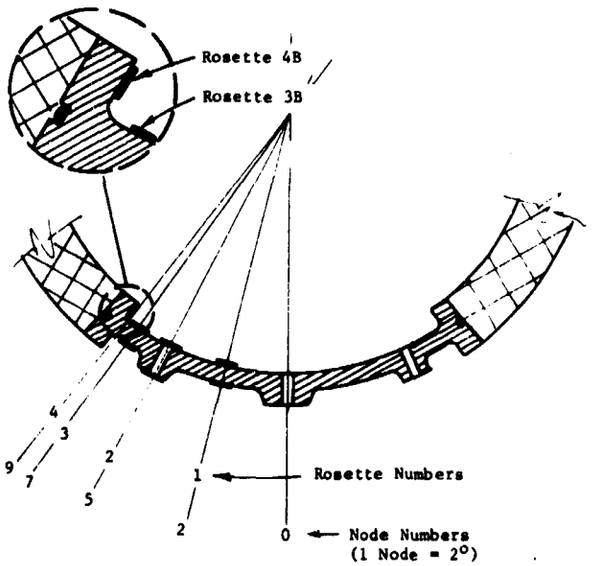

Figure 7. Location of and numbering system for rosettes on the stainless steel plate portion of the capsule.

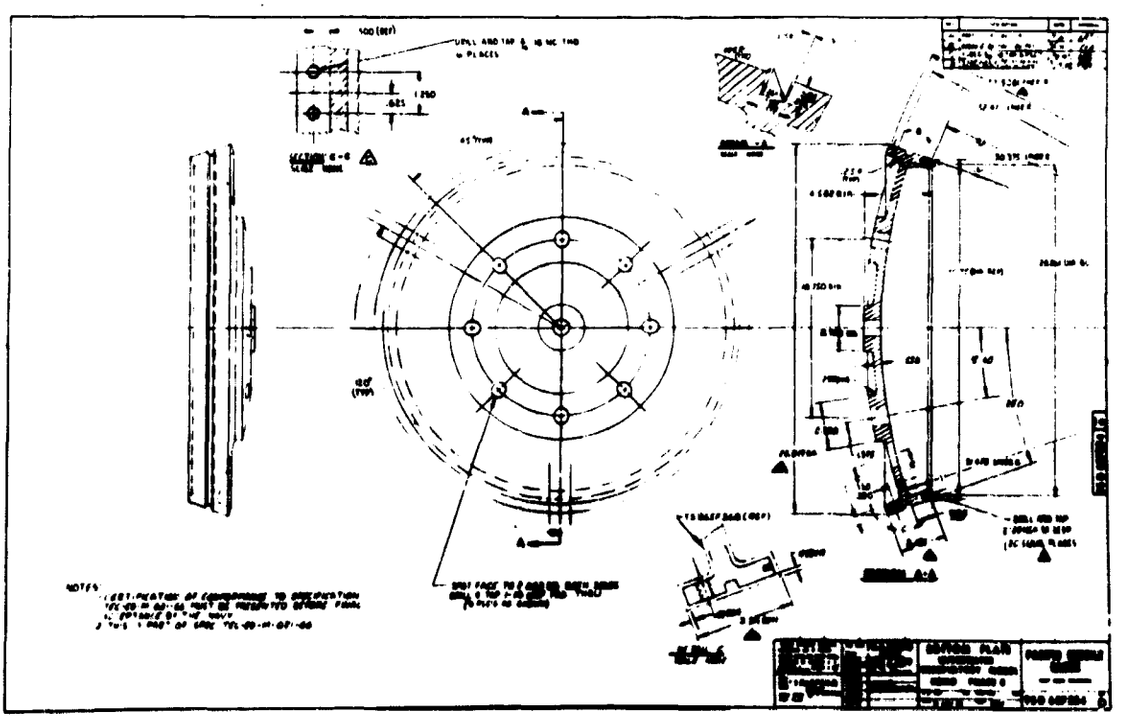

Figure 7a. Detailed dimensions of the bottom steel plate for prototype NEMO fabricated from 316 Type stainless steel.

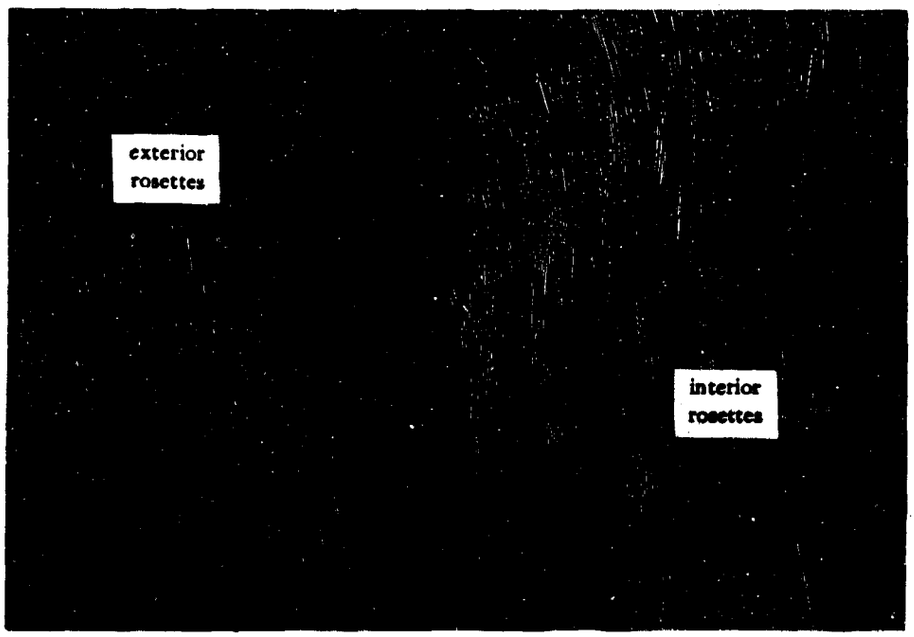

Figure 8. Typical installation of strain gage rosettes on the interior and exterior surfaces of the acrylic hull.

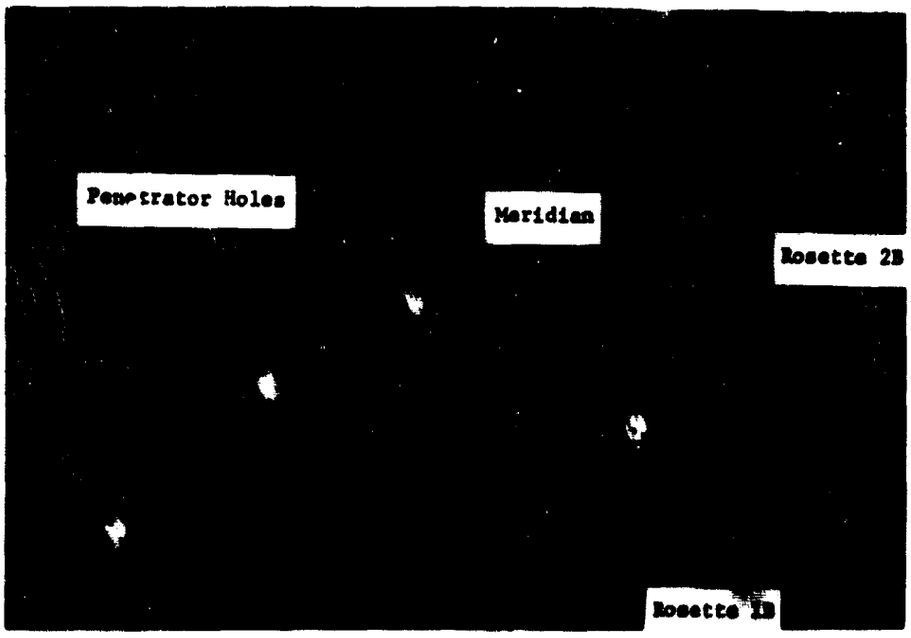

Figure 9. Typical installation of strain gage rosettes on the interior surface of the bottom steel plate.

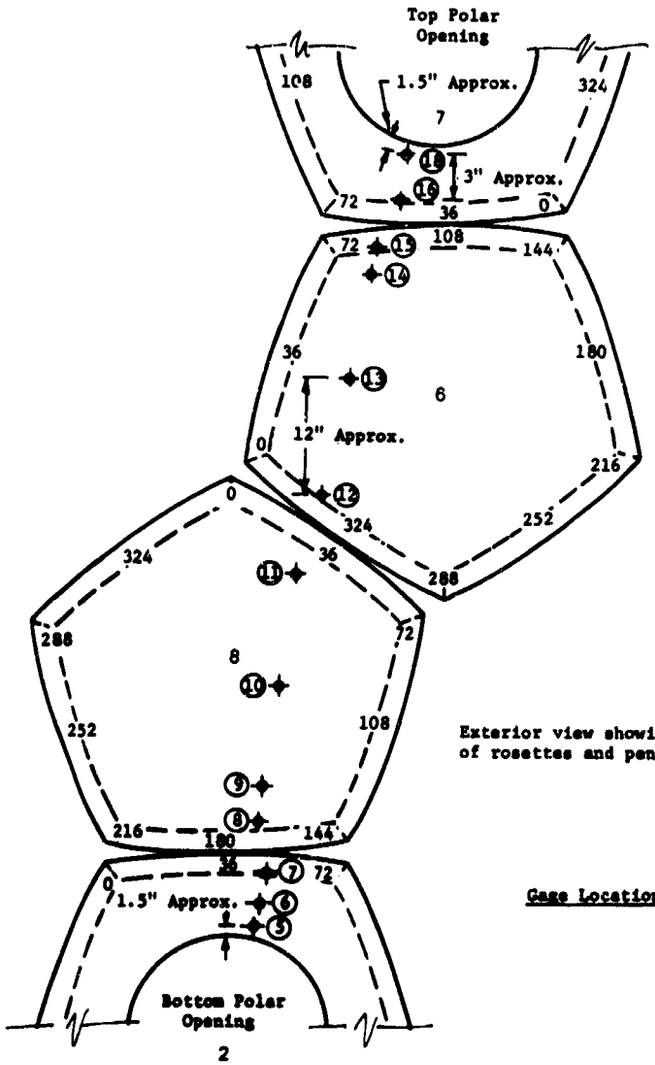

Rosette No.	Thickness of Acrylic (Inches)	Sphericity Deviation*
5	2.395	+.010
6	2.455	+.030
7	2.480	+.050
8	2.495	+.040
9	2.470	+.030
10	2.405	+.026
11	2.400	+.047
12	2.425	+.044
13	2.380	+.010
14	2.500	+.013
15	2.500	+.048
16	2.520	+.042
18	2.460	+.007

* Denotes longer radius of curvature than the nominal 33.000 inch radius

Figure 10. Thickness and curvature of the acrylic hull under strain gage rosettes.

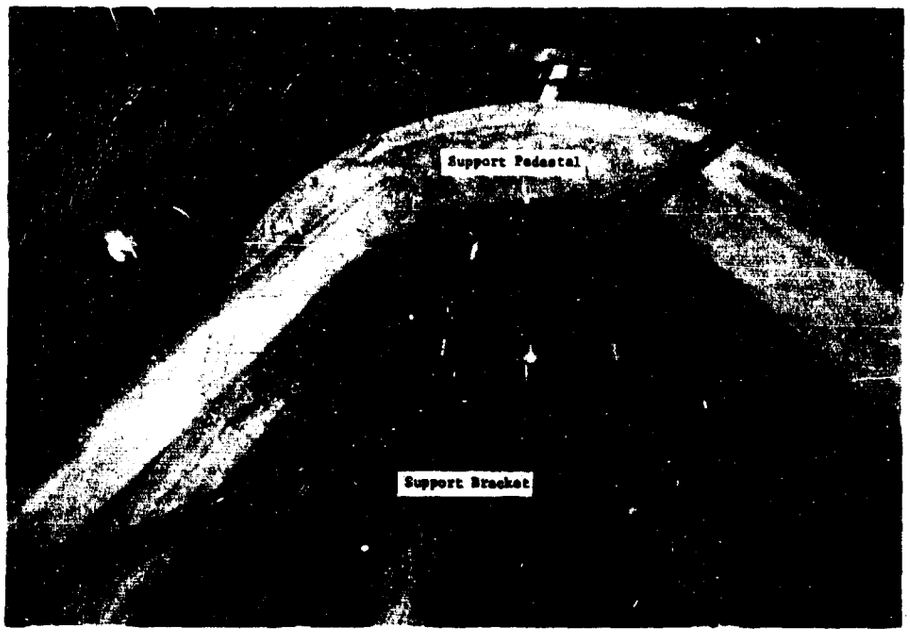

Figure 11. An exterior view of the bottom steel plate showing the support pedestal as well as the penetrators and cables for strain gages located on the interior of the capsule.

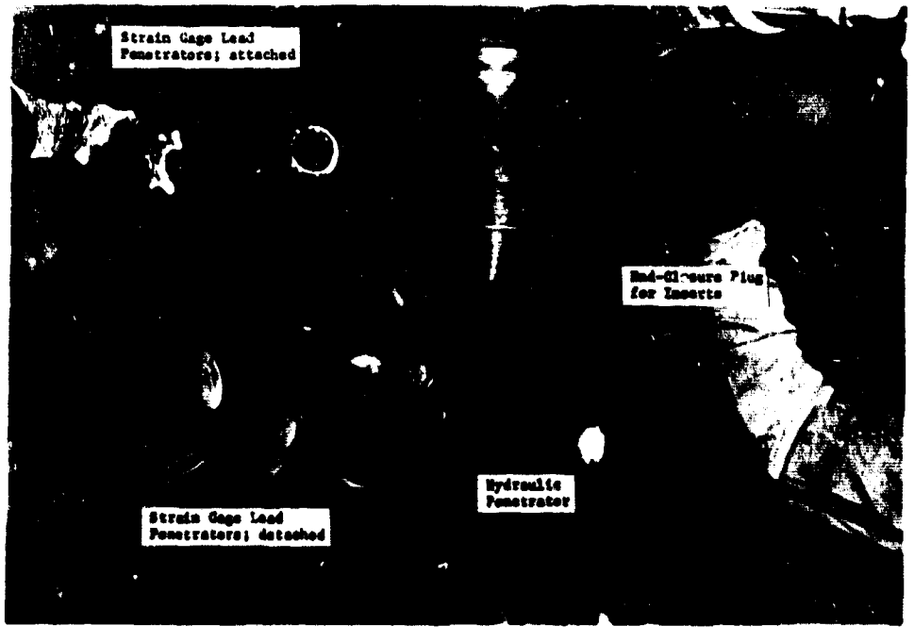

Figure 12. Pressure vessel head plug for accommodating electrical and hydraulic penetrators during hydrostatic testing of NEMO.

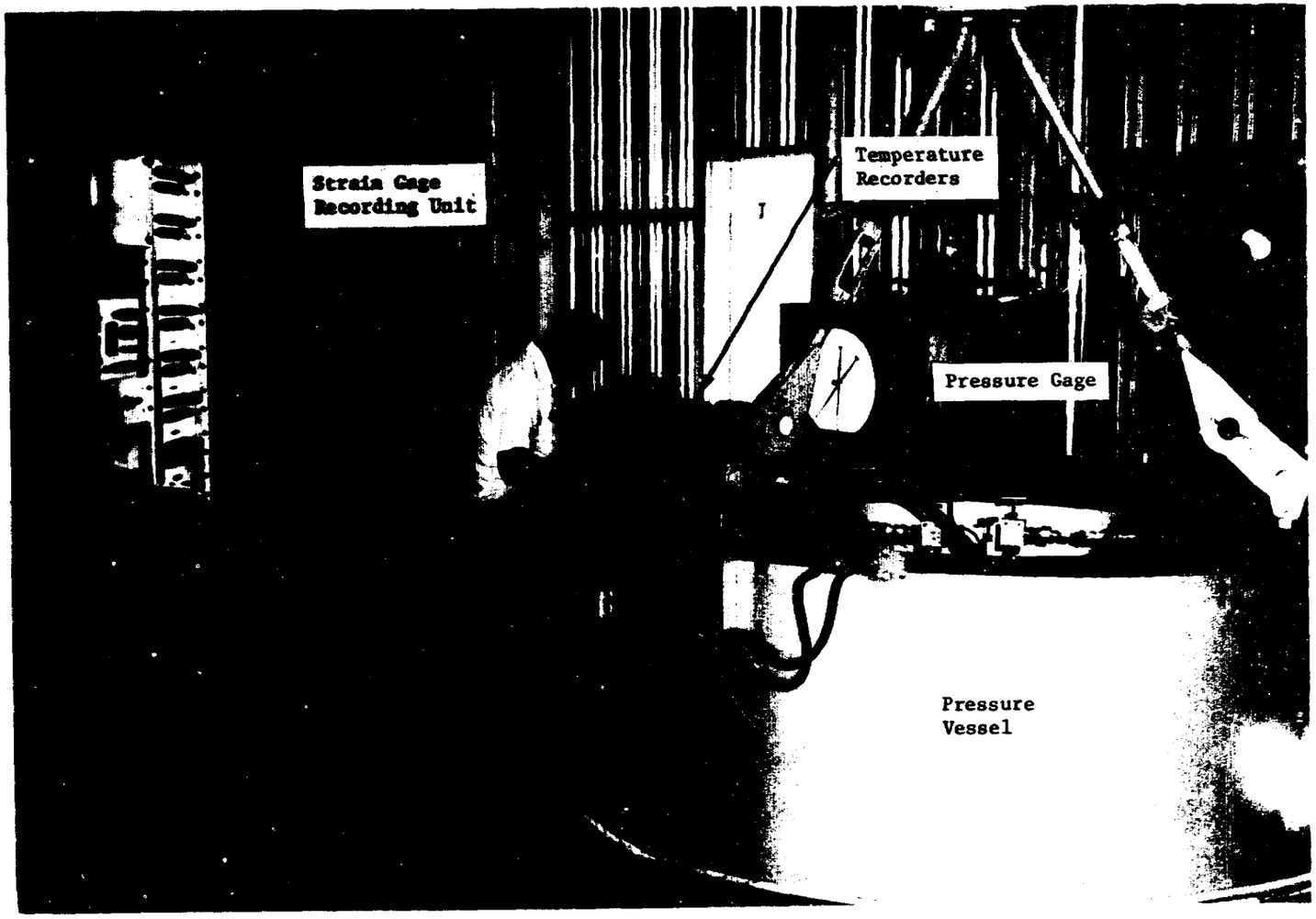

Figure 13. General view of instruments for monitoring the hydrostatic testing of NEMO inside the pressure vessel.

Figure 14a. Strains & Stresses During Short-Term Loading to 100 Psi (Phase 1a)

Press		ε_a	ε_b	ε_c	Principal Strains		$\frac{\tan 2\theta}{2}$	Principal Stresses		Shear Stress
50	1A	126.	119.	167.	167.2	107.3	1.222	5844.1	4513.4	2521.5
100	1A	135.	120.	187.	187.1	113.5	1.091	6471.5	4834.7	2790.3
50	2A	-10.	-10.	-18.	-7.3	-17.9	.866	-378.3	-615.3	231.5
100	2A	-33.	-20.	-16.	-12.7	-33.2	.115	-677.3	-1133.4	422.4
50	3A	17.	15.	-26.	30.0	-26.0	.789	680.8	-564.6	510.5
100	3A	4.	-9.	-61.	17.7	-61.7	.577	15.0	-1750.1	805.5
50	1B	11.	-33.	-20.	12.1	-40.1	-.150	50.3	-1109.7	580.0
100	1B	-41.	-53.	-53.	-41.0	-57.0	0.000	-1676.2	-2031.8	177.7
50	3B	-178.	-49.	-54.	-9.2	-178.0	-.017	-1668.9	-5419.3	1875.1
100	3B	-392.	-96.	-103.	-1.9	-392.0	-.010	-3119.7	-11788.3	4334.2
50	4B	10.	-129.	-65.	19.0	-141.6	-.258	-535.4	-4105.9	1785.2
100	4B	36.	-194.	-141.	39.4	-238.7	-.112	-680.6	-6861.7	3090.5
50	5A	-405.	-210.	-217.	-149.6	-405.0	-.015	-176.3	-261.4	86.8
100	5A	-732.	-293.	-294.	-147.3	-732.0	0.000	-260.7	-455.6	145.2
50	6A	-531.	-326.	-327.	-258.3	-531.0	-.002	-254.7	-345.5	123.5
100	6A	-949.	-537.	-545.	-404.9	-949.0	-.008	-431.8	-613.2	212.2
50	7A	-524.	-370.	-386.	-328.8	-524.4	-.047	-289.7	-354.8	130.9
100	7A	-974.	-658.	-645.	-543.8	-974.1	.017	-507.5	-651.0	233.1
50	8A	-492.	-438.	-342.	-336.2	-511.7	.407	-291.2	-349.7	129.5
100	8A	-895.	-720.	-616.	-580.8	-906.4	.198	-514.4	-622.9	225.1
50	9A	-423.	-378.	-376.	-361.6	-423.0	.018	-288.3	-308.7	117.3
100	9A	-795.	-710.	-671.	-652.1	-798.5	.161	-531.5	-580.4	215.6
50	10A	-385.	-413.	-400.	-383.1	-415.5	-.261	-297.9	-308.7	119.4
100	10A	-698.	-766.	-727.	-690.9	-769.7	-.348	-546.3	-572.5	216.6
50	11A	-410.	-411.	-435.	-402.3	-435.0	.799	-311.3	-322.2	125.7
100	11A	-745.	-761.	-801.	-735.6	-802.3	.481	-575.1	-597.3	229.1
50	12A	-393.	-399.	-433.	-383.4	-433.2	.640	-301.3	-317.9	122.4
100	12A	-759.	-783.	-848.	-743.4	-849.8	.498	-587.6	-623.1	238.4
50	13A	-389.	-418.	-420.	-388.9	-429.0	.028	-303.3	-316.7	122.5
100	13A	-763.	-802.	-801.	-762.9	-814.3	-.011	-591.2	-608.4	235.4
50	14A	-450.	-402.	-456.	-401.8	-470.1	-1.113	-317.3	-340.1	131.6
100	14A	-877.	-798.	-828.	-788.2	-880.3	-.202	-616.1	-646.8	250.5

Figure 14a. (cont'd)

Press		ε_a	ε_b	ε_c	Principal Strains		$\frac{\tan 2\theta}{2}$	Principal Stresses		Shear Stress
50	16A	-468.	-360.	-444.	-358.5	-489.4	-.551	-298.6	-342.2	128.6
100	16A	-959.	-705.	-793.	-670.0	-967.9	-.181	-571.2	-670.4	248.6
50	18A	-514.	-133.	-276.	-85.4	-529.9	-.200	-165.8	-314.0	107.9
100	18A	-1045.	-347.	-446.	-176.5	-1048.7	-.066	-332.6	-623.3	213.8
50	8B	-422.	-472.	-481.	-421.6	-495.0	.071	-305.0	-329.5	12.2
100	8B	-743.	-884.	-826.	-735.8	-899.4	-.224	-538.7	-593.3	27.2
50	9B	-413.	-471.	-471.	-413.0	-490.3	0.000	-299.8	-325.5	12.8
100	9B	-759.	-849.	-856.	-758.8	-883.7	.032	-547.7	-589.4	20.8
50	10B	-462.	-464.	-482.	-456.6	-482.0	.708	-320.6	-329.1	4.2
100	10B	-885.	-868.	-878.	-867.1	-886.8	-.360	-603.8	-610.4	3.2
50	11B	-481.	-471.	-519.	-461.0	-519.5	1.484	-329.7	-349.2	9.7
100	11B	-976.	-983.	-1040.	-959.1	-1040.2	.695	-678.5	-705.5	13.5
50	12B	-444.	-469.	-496.	-439.6	-499.6	.303	-315.1	-335.1	10.0
100	12B	-926.	-952.	-1012.	-912.4	-1014.2	.463	-649.9	-683.8	16.9
50	13B	-449.	-476.	-501.	-445.3	-505.3	.274	-319.0	-339.0	10.0
100	13B	-906.	-992.	-1018.	-904.3	-1039.6	.113	-650.3	-695.4	22.5
50	14B	-362.	-467.	-482.	-361.5	-512.4	.057	-277.3	-327.7	25.1
100	14B	-783.	-934.	-900.	-780.8	-963.7	-.109	-573.4	-634.4	30.4
50	15B	-325.	-442.	-437.	-324.9	-477.7	-.018	-252.3	-303.3	25.4
100	15B	-690.	-871.	-817.	-685.3	-899.9	-.151	-513.0	-584.5	35.7
100	3A	+ 4.	- 9.	- 61.	+ 18.	- 62.	1.15	- 358.	-2122.	900
100	2B	-125.	- 67	- 63.	- 45.	-125.	0.058	- 390.	-3400.	

Figure 14b. Strains & Stresses During Short-Term Loading to 500 Psi (Phase 1e)

Press		ε_a	ε_b	ε_c	Principal Strains		$\frac{\tan 2\theta}{2}$	Principal Stresses		Shear Stress
100	1B	-150.	-20.	-50.	5.2	-151.9	-.112	-1028.1	-4521.4	1746.6
200	1B	-310.	-10.	-130.	24.3	-324.3	-.216	-1801.0	-9550.2	3874.5
300	1B	-330.	-30.	-150.	4.3	-344.3	-.216	-2557.8	-10307.0	3874.5
400	1B	-370.	-60.	-180.	-22.8	-383.8	-.207	-3682.7	-11704.6	4010.9
450	1B	-360.	-80.	-190.	-47.1	-372.8	-.211	-4326.1	-11565.7	3619.7
500	1B	-410.	-80.	-200.	-37.1	-422.8	-.192	-4416.6	-12988.7	4286.0
100	2B	-60.	-60.	10.	9.9	-83.3	.866	-350.3	-2424.4	1037.0
200	2B	-150.	-130.	-40.	-39.0	-174.3	.599	-2532.4	-5530.5	1503.5
300	2B	-240.	-180.	-120.	-110.7	-249.2	.288	-5271.2	-8350.4	1539.6
400	2B	-380.	-250.	-160.	-135.6	-391.0	.222	-7125.8	-12802.0	2838.1
450	2B	-380.	-250.	-170.	-144.2	-389.0	.203	-7370.4	-12809.7	2719.6
500	2B	-430.	-280.	-190.	-160.0	-439.9	.199	-8240.2	-14462.4	3111.1
100	3B	-250.	-150.	-50.	-34.5	-265.4	.288	-3109.6	-8241.6	2566.0
200	3B	-430.	-240.	-150.	-108.2	-438.3	.165	-6674.3	-14010.3	3667.0
300	3B	-540.	-310.	-240.	-182.1	-544.5	.114	-9720.4	-17775.0	4027.3
400	3B	-660.	-370.	-330.	-245.3	-661.2	.055	-12531.9	-21774.3	4621.1
450	3B	-700.	-400.	-370.	-279.2	-700.7	.041	-13858.9	-23223.0	4682.5
500	3B	-810.	-440.	-420.	-303.0	-810.2	.022	-15427.5	-26698.5	5635.4
100	4B	40.	-190.	-90.	53.1	-213.1	-.240	-67.7	-5086.2	2959.2
200	4B	50.	-310.	-230.	54.9	-381.6	-.108	-1329.6	-11030.7	4850.5
300	4B	90.	-400.	-360.	90.8	-537.5	-.036	-1468.6	-15432.2	6981.8
400	4B	120.	-520.	-460.	121.4	-694.8	-.042	-1777.0	-19916.6	9069.7
450	4B	150.	-540.	-520.	150.1	-756.8	-.012	-1400.1	-21554.8	10077.3
500	4B	190.	-590.	-590.	190.0	-850.0	0.000	-930.9	-24042.0	11555.5
100	1A	0.	30.	10.	30.9	-4.3	-.433	861.3	77.4	417.2
200	1A	-10.	10.	-10.	9.9	-16.6	-.366	99.8	-492.6	241.6
300	1A	10.	0.	-20.	14.3	-20.9	.433	160.4	-623.4	321.3
400	1A	-10.	-20.	-40.	-5.6	-40.9	.433	-631.4	-1415.3	434.0
450	1A	-20.	-10.	-40.	-5.6	-40.9	2.598	-649.9	-1432.9	423.8
500	1A	-40.	-10.	-40.	-10.0	-49.9	-.866	-866.3	-1755.2	526.5

Figure 14b. (cont'd)

Press		ϵ_a	ϵ_b	ϵ_c	Principal Strain		tan 2θ / 2	Principal Stresses		Shear Stress
100	2A	0.	30.	30.	40.0	0.0	0.000	1166.0	277.1	530.2
200	2A	-10.	20.	10.	24.3	-10.9	-.173	573.9	-200.9	366.8
300	2A	-20.	10.	0.	14.3	-20.9	-.173	160.4	-623.4	321.3
400	2A	-30.	-10.	-10.	-3.3	-29.9	0.000	-474.8	-1067.4	296.2
450	2A	-40.	0.	-10.	7.3	-40.7	-.123	-254.5	-1322.8	463.9
500	2A	-30.	0.	-10.	4.3	-30.9	-.173	-288.2	-1072.1	330.7
100	6A	-980.	-570.	-600.	-452.7	-980.5	-.032	-462.0	-637.9	223.7
200	6A	-1900.	-1010.	-1030.	-726.5	-1900.1	-.000	-821.3	-1212.5	416.4
300	6A	-2790.	-1430.	-1480.	-1009.5	-2790.4	-.016	-1180.1	-1773.7	604.8
400	6A	-3750.	-1880.	-1960.	-1309.1	-3750.8	-.018	-1559.9	-2373.8	809.1
450	6A	-4130.	-2070.	-2170.	-1448.7	-4131.2	-.021	-1726.7	-2620.9	889.9
500	6A	-4490.	-2180.	-2400.	-1551.1	-4495.4	-.043	-1871.5	-2853.0	964.0
100	7A	-1000.	-550.	-750.	-506.3	-1027.0	-.247	-497.8	-671.3	238.9
200	7A	-1980.	-1030.	-1340.	-890.5	-2009.4	-.168	-925.0	-1298.0	455.4
300	7A	-3000.	-1580.	-1930.	-1315.7	-3024.2	-.121	-1379.9	-1948.5	682.9
400	7A	-3970.	-2290.	-2580.	-1909.7	-3983.6	-.081	-1909.7	-2601.0	918.1
450	7A	-4320.	-2560.	-2860.	-2159.4	-4333.8	-.080	-2127.5	-2852.4	1005.1
500	7A	-5020.	-2930.	-3200.	-2404.0	-5029.2	-.059	-2404.7	-3279.8	1159.3
100	8A	-860.	-740.	-590.	-573.7	-886.2	.333	-507.1	-611.2	220.3
200	8A	-1750.	-1400.	-1230.	-1153.8	-1766.1	.169	-1016.4	-1220.5	440.4
300	8A	-2600.	-2110.	-1870.	-1763.7	-2622.9	.170	-1536.7	-1823.2	660.3
400	8A	-3500.	-2840.	-2550.	-2401.1	-3525.5	.155	-2079.5	-2454.3	802.3
450	8A	-3930.	-3190.	-2860.	-2693.9	-3959.3	.157	-2334.4	-2756.2	1001.6
500	8A	-4340.	-3610.	-3260.	-3100.3	-4372.9	.167	-2644.9	-3068.2	1122.9
100	9A	-880.	-770.	-770.	-733.3	-879.9	0.000	-587.8	-636.7	242.9
200	9A	-1680.	-1450.	-1450.	-1373.3	-1679.9	0.000	-1113.5	-1215.7	456.1
300	9A	-2470.	-2160.	-2160.	-2056.6	-2469.9	0.000	-1659.5	-1797.3	575.9
400	9A	-3290.	-2910.	-2900.	-2776.6	-3290.0	.011	-2229.8	-2490.9	904.7
450	9A	-3690.	-3250.	-3240.	-3096.6	-3690.0	.000	-2492.6	-2690.4	1011.7
500	9A	-4200.	-3670.	-3650.	-3479.8	-4200.1	.016	-2807.6	-3047.7	1147.4

Figure 14b. (cont'd)

Press		ε_a	ε_b	ε_c	Principal Strains		$\frac{\tan 2\theta}{2}$	Principal Stresses		Shear Stress
100	10A	-760.	-800.	-820.	-758.0	-828.6	.173	-591.3	-614.8	237.1
200	10A	-1450.	-1550.	-1540.	-1449.7	-1576.9	-.045	-1134.1	-1176.5	450.2
300	10A	-2080.	-2290.	-2240.	-2076.6	-2329.9	-.117	-1644.7	-1729.1	654.9
400	10A	-2780.	-3000.	-2900.	-2766.1	-3020.5	-.254	-2176.9	-2269.8	857.9
450	10A	-3120.	-3380.	-3330.	-3117.3	-3435.9	-.092	-2457.6	-2563.8	971.4
500	10A	-3480.	-3750.	-3710.	-3478.4	-3814.9	-.069	-2737.7	-2849.9	1081.2
100	11A	-830.	-830.	-830.	-830.0	-830.0	0.000	-628.4	-628.4	248.8
200	11A	-1520.	-1550.	-1610.	-1507.0	-1612.9	.433	-1170.9	-1205.3	465.3
300	11A	-2240.	-2310.	-2350.	-2235.7	-2364.2	.192	-1732.4	-1775.2	684.8
400	11A	-2950.	-2990.	-3010.	-2948.0	-3018.6	.173	-2260.9	-2292.5	865.7
450	11A	-3350.	-3430.	-3460.	-3347.6	-3478.9	.136	-2583.4	-2627.2	1015.1
500	11A	-3780.	-3840.	-3880.	-3775.2	-3891.4	.216	-2903.7	-2942.4	1141.2
100	12A	-730.	-770.	-910.	-694.1	-912.4	.551	-573.6	-646.3	242.0
200	12A	-1440.	-1520.	-1710.	-1396.5	-1716.8	.470	-1132.0	-1238.7	466.0
300	12A	-2130.	-2290.	-2480.	-2097.6	-2502.3	.322	-1686.4	-1821.2	686.8
400	12A	-2720.	-2900.	-3070.	-2694.5	-3098.7	.277	-2153.4	-2288.1	859.2
450	12A	-3180.	-3430.	-3640.	-3150.7	-3682.5	.256	-2519.0	-2696.3	1018.6
500	12A	-3570.	-3830.	-4060.	-3536.9	-4103.0	.265	-2819.4	-3008.2	1139.3
100	13A	-800.	-850.	-850.	-800.0	-866.6	0.000	-619.6	-641.8	250.1
200	13A	-1510.	-1580.	-1580.	-1510.0	-1603.3	0.000	-1160.8	-1200.9	464.2
300	13A	-2250.	-2290.	-2290.	-2250.0	-2303.3	0.000	-1728.8	-1746.5	677.0
400	13A	-2850.	-2950.	-2940.	-2849.7	-2976.9	-.045	-2211.1	-2253.5	863.0
450	13A	-3300.	-3440.	-3420.	-3299.2	-3474.0	-.066	-2557.7	-2616.0	1006.6
500	13A	-3700.	-3830.	-3820.	-3699.8	-3866.8	-.034	-2860.6	-2916.3	1125.0
100	14A	-920.	-880.	-880.	-866.6	-919.9	0.000	-663.4	-681.1	269.6
200	14A	-1740.	-1590.	-1590.	-1540.0	-1740.0	0.000	-1209.7	-1276.4	491.9
300	14A	-2600.	-2350.	-2340.	-2259.9	-2600.0	.016	-1787.1	-1900.5	728.5
400	14A	-3390.	-2990.	-3010.	-2869.7	-3390.2	-.022	-2295.5	-2469.0	936.2
450	14A	-3920.	-3440.	-3440.	-3280.0	-3920.0	0.000	-2627.9	-2841.2	1079.4
500	14A	-4430.	-3850.	-3850.	-3656.6	-4429.9	0.000	-2939.5	-3197.3	1214.1

Figure 14b. (cont'd)

Press		ε_a	ε_b	ε_c	Principal Strains		$\frac{\tan 2\theta}{2}$	Principal Stresses		Shear Stress
100	16A	-1100.	-740.	-800.	-657.2	-1102.7	-.078	-588.8	-737.3	271.9
200	16A	-2020.	-1380.	-1480.	-1229.1	-2024.2	-.073	-1101.3	-1366.3	498.7
300	16A	-3010.	-2080.	-2160.	-1821.5	-3011.7	-.038	-1636.2	-2032.9	740.5
400	16A	-3950.	-2750.	-2860.	-2420.6	-3952.6	-.04[illegible]	-2166.2	-2676.8	974.5
450	16A	-4410.	-3080.	-3200.	-2713.8	-4412.8	-.04[illegible]	-2426.0	-2992.3	1088.7
500	16A	-4960.	-3450.	-3600.	-3042.7	-4963.9	-.0[illegible]	-2720.5	-3360.9	1224.7
100	18A	-1250.	-470.	-540.	-255.0	-1251.6	-.040	-409.2	-741.4	261.6
200	18A	-2090.	-820.	-810.	-389.9	-2090.0	.003	-682.8	-1249.4	428.4
300	18A	-2910.	-1170.	-1130.	-563.1	-2910.2	.009	-972.6	-1755.0	593.9
400	18A	-3780.	-1540.	-1450.	-732.4	-3780.8	.017	-1269.6	-2285.7	769.8
450	18A	-4180.	-1700.	-1610.	-812.5	-4180.8	.015	-1409.3	-2532.1	850.0
500	18A	-4690.	-1910.	-1760.	-881.3	-4691.9	.022	-1563.3	-2833.5	952.9
100	8B	-810.	-980.	-970.	-809.8	-1030.1	-.026	-600.2	-673.6	36.7
200	8B	-1520.	-1840.	-1840.	-1520.0	-1946.6	0.000	-1128.8	-1271.1	71.1
300	8B	-2190.	-2670.	-2680.	-2189.9	-2836.7	.008	-1632.2	-1847.7	107.7
400	8B	-2910.	-3580.	-3570.	-2909.9	-3796.7	-.006	-2173.7	-2469.3	147.7
450	8B	-3210.	-4020.	-4020.	-3210.0	-4290.0	0.000	-2416.1	-2776.1	179.9
500	8B	-3620.	-4530.	-4520.	-3619.9	-4826.6	-.004	-2722.7	-3124.9	201.1
100	9B	-830.	-910.	-960.	-824.2	-975.7	.206	-597.8	-648.3	25.2
200	9B	-1580.	-1800.	-1810.	-1579.8	-1880.1	.019	-1147.6	-1247.7	50.0
300	9B	-2290.	-2670.	-2660.	-2289.9	-2790.0	-.011	-1675.1	-1841.8	83.3
400	9B	-2990.	-3500.	-3570.	-2987.7	-3718.9	.055	-2199.6	-2443.3	121.8
450	9B	-3340.	-3950.	-4020.	-3338.1	-4201.8	.046	-2466.0	-2753.9	143.9
500	9B	-3730.	-4400.	-4510.	-3725.8	-4700.8	.065	-2754.4	-3079.4	162.4
100	10B	-940.	-910.	-920.	-905.6	-940.9	-.173	-633.3	-645.1	5.8
200	10B	-1770.	-1800.	-1790.	-1769.0	-1804.3	-.173	-1231.0	-1242.8	5.8
300	10B	-2640.	-2660.	-2660.	-2640.0	-2666.6	0.000	-1832.4	-1841.3	4.4
400	10B	-3440.	-3540.	-3490.	-3432.2	-3547.7	-.288	-2396.9	-2435.3	19.2
450	10B	-3940.	-4050.	-3930.	-3896.4	-4050.2	-1.039	-2725.1	-2776.3	25.6
500	10B	-4410.	-4520.	-4450.	-4395.7	-4524.2	-.404	-3066.2	-3109.1	21.4

Figure 14b. (cont'd)

Press		ε_a	ε_b	ε_c	Principal Strains		$\frac{\tan 2\theta}{2}$	Principal Stresses		Shear Stress
100	11B	-930.	-850.	-1110.	-809.5	-1117.1	2.251	-615.6	-718.1	51.2
200	11B	-1840.	-1810.	-2060.	-1745.7	-2060.9	1.139	-1265.1	-1370.2	52.5
300	11B	-2790.	-2800.	-3030.	-2716.5	-3030.1	.796	-1936.9	-2041.4	52.2
400	11B	-3640.	-3710.	-3930.	-3585.2	-3934.7	.529	-2544.8	-2661.3	58.2
450	11B	-4090.	-4070.	-4560.	-3919.7	-4560.2	.943	-2828.6	-3042.1	106.7
500	11B	-4660.	-4680.	-5090.	-4529.7	-5090.2	.789	-3236.5	-3423.4	93.4
100	12B	-1020.	-980.	-1080.	-968.5	-1084.7	4.330	-691.3	-730.1	19.3
200	12B	-1960.	-1820.	-2080.	-1803.0	-2103.5	-11.258	-1302.2	-1402.3	50.0
300	12B	-2860.	-2640.	-3000.	-2623.7	-3042.8	-3.897	-1891.6	-2031.3	69.8
400	12B	-3110.	-3430.	-3890.	-3023.9	-3929.4	.362	-2256.0	-2557.8	150.9
450	12B	-4200.	-4010.	-4470.	-3959.7	-4493.5	4.979	-2837.1	-3015.1	88.9
500	12B	-4680.	-4470.	-5010.	-4405.6	-5034.3	3.897	-3162.9	-3372.4	104.7
100	13B	-990.	-1000.	-1020.	-985.6	-1020.9	.433	-688.7	-700.4	5.8
200	13B	-1870.	-1890.	-1920.	-1864.2	-1922.3	.371	-1301.0	-1320.4	9.6
300	13B	-2700.	-2800.	-2910.	-2682.0	-2924.6	.307	-1900.3	-1981.1	40.4
400	13B	-3520.	-3600.	-3840.	-3461.0	-3845.6	.519	-2465.1	-2593.3	64.0
450	13B	-4060.	-4190.	-4440.	-4006.9	-4453.0	.424	-2854.1	-3002.7	74.3
500	13B	-4530.	-4670.	-4970.	-4463.7	-4982.9	.447	-3183.4	-3356.5	86.5
100	14B	-890.	-960.	-960.	-890.0	-983.3	0.000	-632.9	-664.0	15.5
200	14B	-1650.	-1860.	-1820.	-1647.9	-1905.4	-.091	-1187.0	-1272.9	42.9
300	14B	-2480.	-2780.	-2680.	-2470.2	-2823.0	-.173	-1773.5	-1891.1	58.7
400	14B	-3290.	-3540.	-3560.	-3289.6	-3637.0	.033	-2339.7	-2455.5	57.9
450	14B	-3750.	-4160.	-3980.	-3726.0	-4200.6	-.243	-2664.7	-2822.5	79.0
500	14B	-4190.	-4640.	-4440.	-4162.9	-4683.6	-.247	-2975.5	-3149.0	86.7
100	15B	-700.	-960.	-890.	-694.6	-1005.3	-.134	-536.6	-640.2	51.7
200	15B	-1440.	-1790.	-1620.	-1414.5	-1818.7	-.277	-1051.8	-1186.5	67.3
300	15B	-2210.	-2620.	-2440.	-2186.0	-2660.6	-.243	-1598.5	-1756.7	79.0
400	15B	-2910.	-3490.	-3170.	-2854.5	-3525.4	-.329	-2096.6	-2320.2	111.8
450	15B	-3260.	-3920.	-3570.	-3202.0	-3964.6	-.312	-2353.6	-2607.8	127.0
500	15B	-3620.	-4370.	-3980.	-3556.8	-4423.1	-.304	-2617.9	-2906.6	144.3
500	3A	+50.	-200.	-200.	+50.0	-283.0	0	-886.0	-8292.0	3834.0

Figure 14c. Strains & Stresses During Short-Term Loading to 800 Psi (Phase Ih)

Press		ε_a	ε_b	ε_c	Principal Strains		$\frac{\tan 2\theta}{2}$	Principal Stresses		Shear Stress
100	1A	-50.	-10.	-10.	3.3	-49.9	0.000	-325.4	-1510.6	618.0
200	1A	-30.	0.	0.	10.0	-30.0	0.000	-4.2	-893.0	380.9
300	1A	-70.	-30.	-30.	-16.6	-69.9	0.000	-1152.4	-2337.6	834.7
400	1A	-100.	-50.	-40.	-26.2	-100.4	.078	-1712.0	-3361.7	1210.5
500	1A	-100.	-60.	-60.	-46.6	-100.0	0.000	-2357.8	-3543.0	1251.1
600	1A	-130.	-80.	-70.	-56.2	-130.4	.078	-2917.4	-4567.1	1625.6
700	1A	-160.	-80.	-80.	-53.3	-159.9	0.000	-3096.7	-5467.1	1944.2
800	1A	-130.	-100.	-90.	-82.6	-130.7	.123	-3782.9	-4851.2	1712.6
100	2A	-20.	-10.	0.	1.5	-21.5	.288	-156.9	-670.1	256.1
200	2A	40.	10.	20.	40.9	5.6	-.173	1204.5	420.6	574.1
300	2A	0.	-10.	-40.	7.3	-40.7	.519	-201.8	-1270.1	481.6
400	2A	-70.	-40.	-30.	-22.6	-70.7	.123	-1372.1	-2440.4	832.4
500	2A	-10.	-30.	-30.	-10.0	-36.6	0.000	-762.2	-1354.8	357.2
600	2A	-40.	-60.	-50.	-38.4	-61.5	-.288	-1846.1	-2359.3	737.9
700	2A	-30.	-40.	-50.	-28.4	-51.5	.288	-1502.8	-2016.0	541.0
800	2A	-50.	-60.	-70.	-48.4	-71.5	.288	-2294.7	-2807.9	850.9
100	8A	-730.	-740.	-600.	-599.8	-780.1	1.010	-501.4	-561.6	204.6
200	8A	-1500.	-1380.	-1190.	-1176.1	-1537.1	.382	-986.7	-1107.0	401.8
300	8A	-2410.	-2070.	-1830.	-1766.8	-2439.8	.225	-1505.5	-1729.8	627.2
400	8A	-3220.	-2730.	-2410.	-2315.5	-3257.7	.213	-1987.5	-2301.6	831.5
500	8A	-4020.	-3410.	-2980.	-2866.5	-4073.4	.225	-2470.3	-2872.6	1025.7
600	8A	-40.	-4120.	-3530.	-17.1	-5109.5	-.067	-1248.9	-2946.4	988.3
700	8A	-5710.	-4820.	-4150.	-3989.6	-5796.9	.236	-3463.3	-4065.8	1463.9
800	8A	-6510.	-5580.	-4680.	-4533.4	-6646.5	.282	-3948.5	-4652.9	1673.4
100	9A	-670.	-780.	-750.	-667.6	-798.9	-.136	-539.6	-583.4	218.0
200	9A	-1390.	-1470.	-1410.	-1375.2	-1471.4	-.519	-1077.0	-1109.1	420.7
300	9A	-2260.	-2210.	-2130.	-2124.2	-2275.7	.384	-1659.3	-1709.8	652.3
400	9A	-3000.	-2890.	-2790.	-2772.0	-3014.6	.270	-2178.0	-2258.8	857.0
500	9A	-3810.	-3590.	-3490.	-3440.9	-3819.0	.160	-2719.2	-2845.3	1076.0
600	9A	-4630.	-4320.	-4190.	-4118.9	-4641.0	.150	-3268.3	-3442.3	1299.5
700	9A	-5460.	-5090.	-4910.	-4829.5	-5477.1	.169	-3836.6	-4052.5	1530.5
800	9A	-6240.	-5840.	-5660.	-5570.5	-6256.1	.159	-4410.3	-4638.8	1756.5

Figure 14c. (cont'd)

Press	ε_a	ε_b	ε_c	Principal Strains		$\frac{\tan 2\theta}{2}$	Principal Stresses		Shear Stress
100 10A	-650.	-700.	-730.	-646.6	-739.9	.199	-518.2	-549.4	204.7
200 10A	-1250.	-1420.	-1400.	-1249.3	-1463.9	-.054	-1011.1	-1082.6	399.9
300 10A	-1950.	-2100.	-2140.	-1947.6	-2178.9	.101	-1551.4	-1628.5	608.3
400 10A	-2560.	-2790.	-2820.	-2559.0	-2887.5	.053	-2046.0	-2155.5	802.1
500 10A	-3230.	-3500.	-3540.	-3228.6	-3618.0	.059	-2574.3	-2704.1	1008.8
600 10A	-3890.	-4210.	-4270.	-3887.4	-4359.2	.074	-3099.0	-3256.3	1215.6
700 10A	-4540.	-4930.	-5000.	-4537.1	-5109.5	.071	-3620.7	-3811.5	1422.5
800 10A	-5230.	-5660.	-5760.	-5224.8	-5875.1	.090	-4164.6	-4381.4	1637.9
100 11A	-720.	-780.	-780.	-720.0	-800.0	0.000	-566.6	-593.3	226.3
200 11A	-1340.	-1460.	-1490.	-1338.3	-1521.6	.096	-1067.1	-1128.2	423.4
300 11A	-2120.	-2220.	-2250.	-2118.0	-2275.2	.112	-1656.1	-1708.5	651.3
400 11A	-2820.	-2930.	-2960.	-2818.2	-2988.4	.103	-2197.0	-2253.7	859.9
500 11A	-3490.	-3650.	-3680.	-3488.7	-3724.6	.074	-2726.8	-2805.4	1067.6
600 11A	-4190.	-4370.	-4430.	-4185.7	-4474.2	.123	-3272.6	-3368.8	1281.9
700 11A	-4890.	-5090.	-5150.	-4886.1	-5200.5	.112	-3816.0	-3920.8	1492.7
800 11A	-5600.	-5830.	-5910.	-5594.1	-5965.8	.128	-4370.3	-4494.2	1711.3
100 12A	-630.	-630.	-700.	-606.6	-699.9	.866	-490.5	-521.7	191.6
200 12A	-1250.	-1310.	-1420.	-1227.1	-1426.2	.414	-992.9	-1059.3	390.0
300 12A	-1900.	-2020.	-2170.	-1873.7	-2186.2	.333	-1514.8	-1618.9	598.1
400 12A	-2490.	-2670.	-2930.	-2441.2	-2952.0	.363	-1997.1	-2167.4	795.2
500 12A	-3120.	-3400.	-3630.	-3088.4	-3678.2	.252	-2513.2	-2709.8	997.6
600 12A	-3720.	-4080.	-4360.	-3682.8	-4423.7	.242	-3005.7	-3252.7	1195.3
700 12A	-4320.	-4790.	-5100.	-4283.1	-5190.1	.214	-3504.9	-3807.3	1397.6
800 12A	-4950.	-5490.	-5850.	-4906.9	-5953.0	.216	-4015.6	-4364.3	1602.7
100 13A	-690.	-680.	-700.	-678.4	-701.5	0.000	-527.6	-535.3	203.2
200 13A	-1330.	-1350.	-1400.	-1318.3	-1401.6	.481	-1035.3	-1063.1	400.0
300 13A	-2000.	-2060.	-2130.	-1988.2	-2138.4	.319	-1564.9	-1615.0	607.8
400 13A	-2610.	-2710.	-2800.	-2596.9	-2816.4	.268	-2052.6	-2125.8	796.0
500 13A	-3270.	-3430.	-3520.	-3260.4	-3552.8	.190	-2578.9	-2676.4	1002.7
600 13A	-3910.	-4110.	-4260.	-3890.5	-4296.0	.236	-3089.3	-3224.5	1205.4
700 13A	-4540.	-4790.	-4920.	-4526.9	-4973.0	.178	-3591.0	-3739.7	1397.8
800 13A	-5210.	-5500.	-5650.	-5195.0	-5711.6	.177	-4120.0	-4292.2	1605.6

Figure 14c. (cont'd)

Press		ϵ_a	ϵ_b	ϵ_c	Principal Strains		tan 2θ / 2	Principal Stresses		Shear Stress
100	16A	-1180.	-830.	-960.	-785.7	-1194.2	-.197	-671.1	-807.3	306.1
200	16A	-2120.	-1450.	-1630.	-1332.9	-2133.7	-.134	-1174.2	-1441.1	532.8
300	16A	-3060.	-2060.	-2310.	-1875.7	-3077.5	-.123	-1675.8	-2076.4	760.0
400	16A	-4040.	-2690.	-3000.	-2426.8	-4059.8	-.112	-2188.5	-2732.9	995.5
500	16A	-5040.	-3330.	-3710.	-2989.8	-5063.4	-.108	-2711.3	-3402.5	1236.6
600	16A	-6000.	-3910.	-4410.	-3513.1	-6033.5	-.117	-3207.6	-4047.7	1466.4
700	16A	-7000.	-4530.	-5150.	-4076.1	-7043.8	-.124	-3731.5	-4720.7	1708.8
800	16A	-7910.	-5120.	-5940.	-4667.5	-7979.1	-.149	-4256.5	-5360.3	1940.6
100	18A	-1890.	-800.	-690.	-360.6	-1892.6	.041	-578.5	-1089.1	403.4
200	18A	-2760.	-1140.	-980.	-489.5	-2763.7	.040	-854.8	-1612.8	576.7
300	18A	-3610.	-1470.	-1270.	-618.8	-3614.4	.038	-1127.6	-2126.1	745.8
400	18A	-4470.	-1870.	-1590.	-809.5	-4477.1	.044	-1434.1	-2656.6	921.4
500	18A	-5380.	-2230.	-1900.	-951.8	-5388.1	.043	-1724.4	-3203.2	1104.1
600	18A	-6250.	-2580.	-2220.	-1108.2	-6258.4	.040	-2014.7	-3731.4	1279.1
700	18A	-7030.	-2940.	-2520.	-1286.4	-7040.2	.042	-2300.2	-4218.1	1436.8
800	18A	-8000.	-3350.	-2850.	-1453.9	-8012.7	.044	-2614.5	-4800.8	1634.0
100	8B	-660.	-970.	-990.	-659.6	-1086.9	.027	-533.4	-675.8	71.2
200	8B	-1290.	-1810.	-1840.	-1289.5	-2003.7	.024	-1020.9	-1259.0	119.0
300	8B	-2020.	-2720.	-2740.	-2019.8	-2966.8	.012	-1568.3	-1883.9	157.8
400	8B	-2670.	-3570.	-3610.	-2669.5	-3897.1	.018	-2068.4	-2477.6	204.5
500	8B	-3370.	-4420.	-4490.	-3368.8	-4817.7	.027	-2592.3	-3075.3	241.4
600	8B	-4020.	-5380.	-5380.	-4020.0	-5833.3	0.000	-3108.5	-3712.9	302.2
700	8B	-4690.	-6310.	-6290.	-4689.9	-6836.7	-.005	-3632.2	-4347.7	357.7
800	8B	-5330.	-729	-7280.	-5329.9	-7936.6	-.002	-4157.8	-5026.7	434.4
100	9B	-820.	-930.	-880.	-813.0	-940.2	-.254	-585.7	-628.1	21.1
200	9B	-1500.	-1770.	-1770.	-1500.0	-1860.0	0.000	-1103.0	-1223.0	59.9
300	9B	-2200.	-2630.	-2700.	-2197.3	-2822.6	.065	-1633.4	-1841.9	104.2
400	9B	-2920.	-3460.	-3500.	-2919.2	-3667.3	.030	-2155.3	-2404.6	124.6
500	9B	-3610.	-4310.	-4490.	-3599.8	-4673.4	.098	-2684.9	-3042.7	178.9
600	9B	-4300.	-5170.	-5330.	-4293.2	-5573.3	.072	-3202.0	-3628.7	213.3
700	9B	-5010.	-6090.	-6230.	-5005.7	-6547.5	.052	-3742.2	-4256.2	256.9
800	9B	-5700.	-7060.	-7200.	-5696.5	-7610.0	.042	-4287.2	-4925.0	318.9

Figure 14c. (cont'd)

Press	ε_a	ε_b	ε_c	Principal Strains		$\frac{\tan 2\theta}{2}$	Principal Stresses		Shear Stress
100 10B	-910.	-890.	-890.	-883.3	-909.9	0.000	-616.3	-625.2	4.4
200 10B	-1750.	-1710.	-1730.	-1706.9	-1753.0	-.288	-1189.9	-1205.3	7.6
300 10B	-2630.	-2650.	-2600.	-2597.6	-2655.7	4.330	-1808.7	-1828.1	9.6
400 10B	-3480.	-3490.	-3460.	-3459.0	-3494.3	2.598	-2401.0	-2412.8	5.8
500 10B	-4370.	-4370.	-4310.	-4310.0	-4389.9	.866	-2998.2	-3024.8	13.3
600 10B	-5260.	-5270.	-5210.	-5209.5	-5283.7	1.2.9	-3619.9	-3644.6	12.3
700 10B	-6160.	-6190.	-6120.	-6116.1	-6197.2	6.062	-4248.7	-4275.8	13.5
800 10B	-7100.	-7130.	-7050.	-7046.6	-7139.9	3.464	-4895.2	-4926.3	15.5
100 11B	-930.	-930.	-960.	-920.0	-959.9	.866	-644.1	-657.4	6.6
200 11B	-1820.	-1840.	-1930.	-1795.6	-1930.9	.599	-1267.4	-1312.5	22.5
300 11B	-2760.	-2800.	-2960.	-2717.7	-2962.2	.577	-1925.4	-2006.8	40.7
400 11B	-3640.	-3740.	-3920.	-3602.8	-3930.5	.410	-2553.0	-2662.3	54.6
500 11B	-4580.	-4660.	-4960.	-4502.0	-4964.6	.564	-3199.8	-3354.0	77.1
600 11B	-5520.	-5650.	-5940.	-5455.0	-5951.6	.456	-3865.7	-4031.2	82.7
700 11B	-6490.	-6620.	-7000.	-6397.3	-7009.3	.514	-4538.7	-4742.7	102.0
800 11B	-7470.	-7600.	-8070.	-7348.8	-8077.8	.557	-5218.5	-5461.4	121.4
100 12B	-940.	-830.	-1000.	-823.7	-1022.8	-2.944	-606.0	-672.4	33.1
200 12B	-1840.	-1710.	-1970.	-1689.8	-1990.1	0.000	-1223.8	-1323.8	50.0
300 12B	-2750.	-2570.	-2930.	-2542.1	-2957.8	0.000	-1834.5	-1973.1	69.2
400 12B	-3570.	-3440.	-3870.	-3372.0	-3881.3	2.190	-2425.8	-2595.6	84.8
500 12B	-4470.	-4330.	-4880.	-4229.9	-4890.0	1.764	-3046.9	-3266.9	110.0
600 12B	-5350.	-5200.	-5850.	-5073.6	-5859.6	1.608	-3653.6	-3915.6	130.9
700 12B	-6230.	-6080.	-6860.	-5912.0	-6867.9	1.407	-4264.5	-4583.1	159.3
800 12B	-7140.	-7010.	-7910.	-6791.6	-7915.0	1.217	-4903.5	-5278.0	187.2
100 13B	-910.	-910.	-910.	-910.0	-910.0	0.000	-629.9	-629.9	0.0
200 13B	-1790.	-1780.	-1830.	-1769.4	-1830.5	1.443	-1235.9	-1256.3	10.1
300 13B	-2670.	-2700.	-2750.	-2660.0	-2753.3	.393	-1858.2	-1889.4	15.5
400 13B	-3490.	-3530.	-3630.	-3466.7	-3633.2	.481	-2429.9	-2485.4	27.7
500 13B	-4360.	-4420.	-4520.	-4340.0	-4526.6	.393	-3038.1	-3100.3	31.1
600 13B	-5220.	-5300.	-5410.	-5199.8	-5420.1	.352	-3639.4	-3712.8	36.7
700 13B	-6080.	-6160.	-6270.	-6059.8	-6280.1	.352	-4234.8	-4308.2	36.7
800 13B	-6960.	-7140.	-7190.	-6956.9	-7236.3	.105	-4866.5	-4959.6	46.5

Figure 14c. (cont'd)

Press		ε_a	ε_b	ε_c	Principal Strains		$\frac{\tan 2\theta}{2}$	Principal Stresses		Shear Stress
100	15B	-550.	-820.	-740.	-543.1	-863.4	-.150	-433.5	-540.3	53.3
200	15B	-1220.	-1550.	-1350.	-1181.3	-1565.2	-.376	-886.7	-1014.7	63.9
300	15B	-1860.	-2260.	-1930.	-1770.0	-2263.3	-.608	-1313.9	-1478.3	82.2
400	15B	-2450.	-2970.	-2480.	-2296.2	-2970.4	-.771	-1710.7	-1935.4	112.3
500	15B	-3080.	-3690.	-3040.	-2849.3	-3690.6	-.987	-2123.6	-2404.0	140.2
600	15B	-3570.	-4340.	-3520.	-3279.2	-4340.7	-.986	-2460.7	-2814.6	176.9
700	15B	-4110.	-5020.	-3980.	-3715.6	-5024.3	-1.154	-2807.2	-3243.4	218.1
800	15B	-4610.	-5690.	-4390.	-4093.2	-5700.1	-1.309	-3122.1	-3657.8	267.8
100	1B	-130.	-80.	-70.	-56.2	-130.4	.078	-2706.6	-4356.3	824.8
200	1B	-190.	-350.	-80.	-49.8	-363.4	-4.676	-4335.9	-11303.6	3483.8
300	1B	-240.	-140.	-110.	-84.7	-241.9	.112	-4433.5	-7926.8	1746.6
400	1B	-270.	-160.	-150.	-116.4	-270.2	.037	-5606.7	-9023.8	1708.5
500	1B	-280.	-180.	-170.	-139.7	-280.2	.041	-6385.1	-9506.7	1560.8
600	1B	-300.	-190.	-190.	-153.3	-299.9	0.000	-6946.9	-10206.2	1629.6
700	1B	-310.	-210.	-230.	-188.8	-311.1	-.096	-8101.6	-10817.2	1357.8
800	1B	-330.	-220.	-240.	-195.6	-330.9	-.086	-8460.4	-11467.5	1503.5
100	2B	-90.	-70.	-30.	-28.0	-98.6	.433	-1612.4	-3180.3	783.9
200	2B	-140.	-80.	-50.	-37.0	-142.9	.173	-2229.5	-4581.2	1175.8
300	2B	-220.	-120.	-110.	-79.7	-220.2	.041	-4114.8	-7236.5	1560.8
400	2B	-290.	-140.	-140.	-90.0	-290.0	0.000	-4966.9	-9411.4	2222.2
500	2B	-360.	-150.	-150.	-80.0	-360.0	0.000	-5213.2	-11435.4	3111.1
600	2B	-410.	-160.	-180.	-89.5	-410.4	-.036	-5894.6	-13024.2	3564.8
700	2B	-440.	-160.	-200.	-91.8	-441.5	-.066	-6204.1	-13975.9	3885.8
800	2B	-450.	-220.	-250.	-162.2	-451.0	-.060	-8395.2	-14811.9	3208.3
100	3B	-20.	-90.	10.	25.9	-92.5	-2.165	55.5	-2578.0	1316.7
200	3B	-160.	-120.	-20.	-16.7	-183.2	.481	-1933.4	-5634.1	1850.3

Figure 14c. (cont'd)

Press		ε_a	ε_b	ε_c	Principal Strains		$\frac{\tan 2\theta}{2}$	Principal Stresses		Shear Stress
300	3B	-280.	-140.	-70.	-39.8	-286.8	.173	-3436.4	-8923.9	2743.7
400	3B	-460.	-180.	-110.	-36.1	-463.8	.096	-4707.1	-14211.7	4752.3
500	3B	-590.	-230.	-150.	-52.6	-593.9	.086	-6220.0	-18248.3	6014.1
600	3B	-720.	-240.	-180.	-38.2	-721.7	.050	-6783.7	-21973.0	7594.6
700	3B	-850.	-250.	-200.	-15.6	-850.9	.034	-7114.9	-25677.8	9281.4
800	3B	-990.	-260.	-230.	3.6	-990.3	.017	-7622.9	-29710.4	11043.7
100	4B	-60.	-80.	10.	11.2	-97.9	1.558	-426.9	-2852.2	1212.6
200	4B	0.	-130.	-50.	15.7	-135.7	-.384	-587.6	-3952.9	1682.6
300	4B	30.	-240.	-170.	35.1	-288.4	-.128	-1197.3	-8388.2	3595.4
400	4B	50.	-360.	-270.	55.4	-442.1	-.106	-1785.9	-12844.6	5529.3
500	4B	120.	-450.	-360.	123.8	-583.8	-.074	-839.6	-16565.7	7863.0
600	4B	130.	-520.	-450.	131.9	-691.9	-.049	-1439.3	-19749.8	9155.2
700	4B	170.	-570.	-540.	170.3	-796.9	-.017	-1108.2	-22603.4	10747.6
800	4B	210.	-560.	-620.	211.1	-857.7	.032	-357.4	-24111.0	11876.8
800	3A	190.	100.	50.	195.0	31.0	0.376	5828.0	2187.0	2120.0
800	6A	-7500.	-4200.	-4100.	-3033.0	-7500.0	0.0258	-3332.0	-4822.0	1660.0

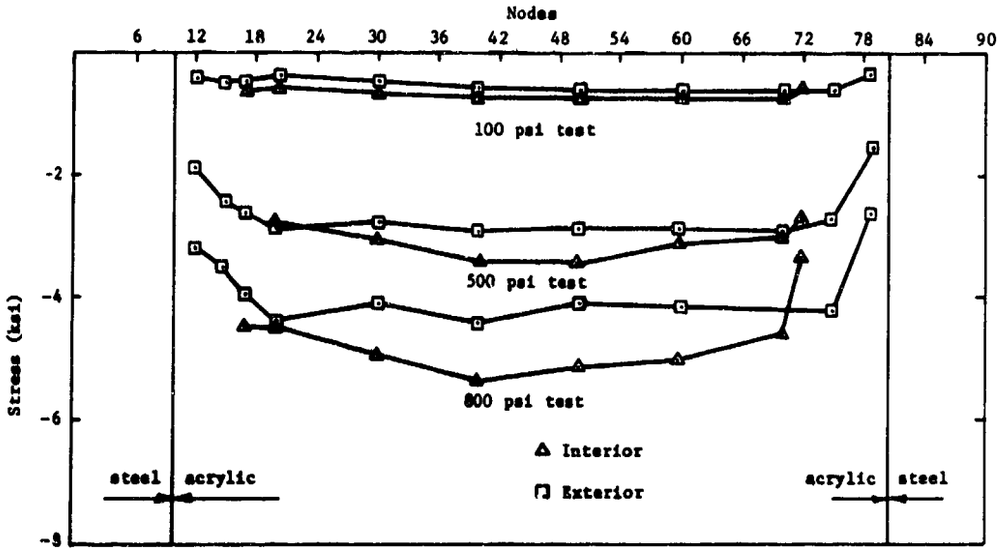

Figure 15a. Distribution of Hoop Stresses on the NEMO acrylic hull.

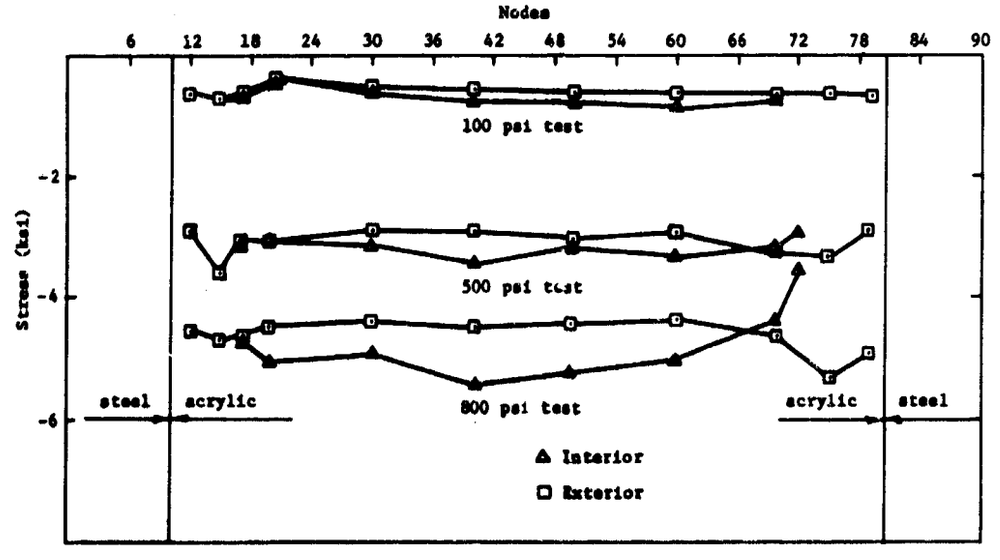

Figure 15b. Distribution of Meridional Stresses on the NEMO acrylic hull.

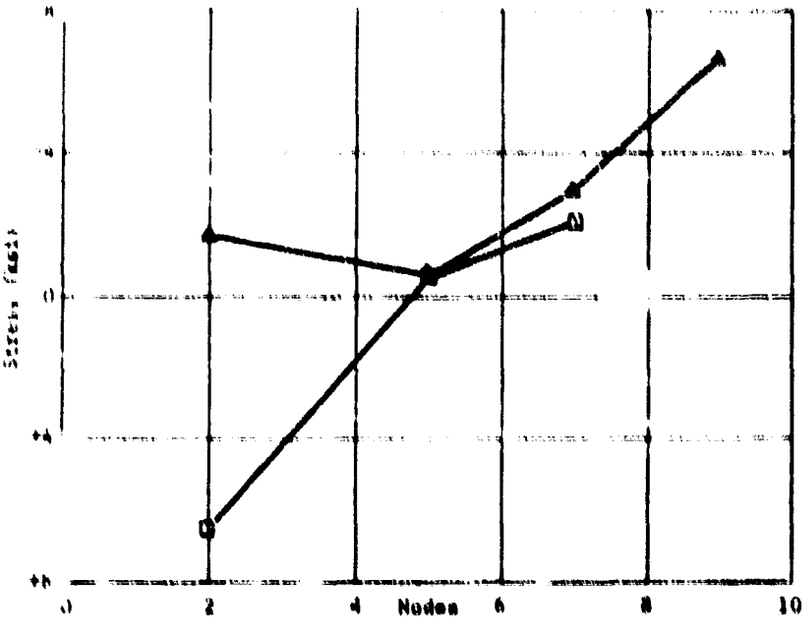

Figure 10a. Hoop stresses on bottom steel plate under 100 psi hydrostatic loading.

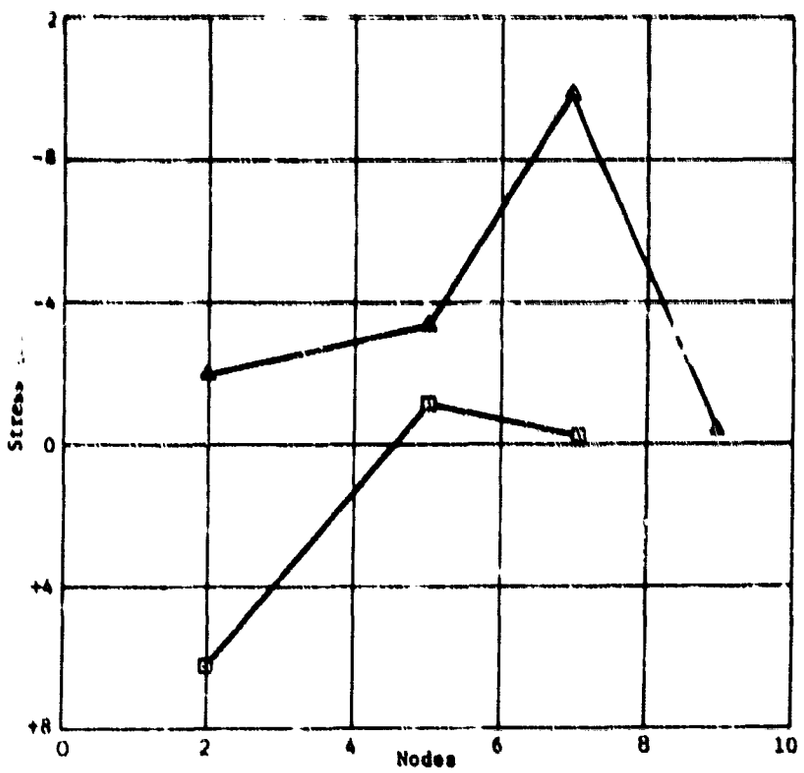

Figure 10b. Meridional Stresses on Bottom Steel Plate Under 100 psi Hydrostatic Loading.

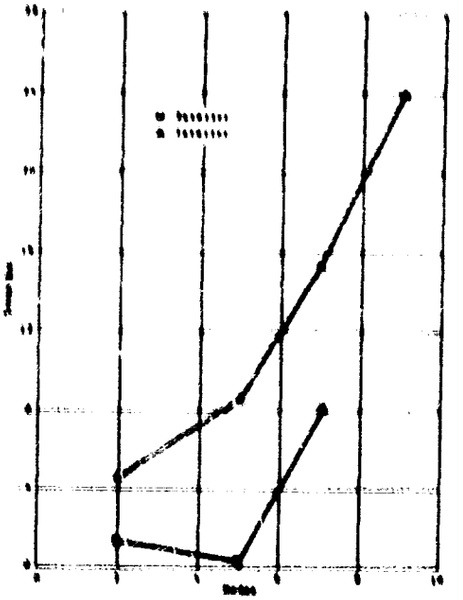

Figure 18a. Hoop stresses on bottom steel plate under 500 psi hydrostatic loading.

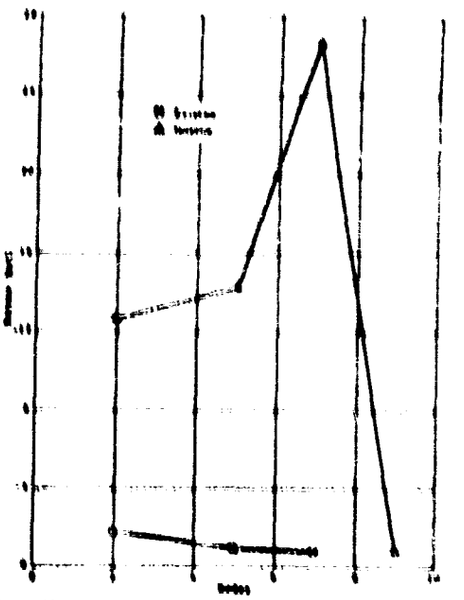

Figure 18b. Meridional stresses on bottom steel plate under 500 psi hydrostatic loading.

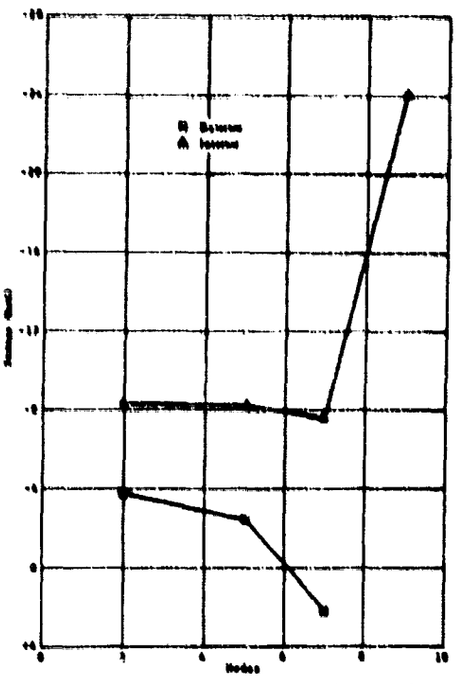

Figure 18a. Hoop stresses on the bottom steel plate under 800 psi hydrostatic loading.

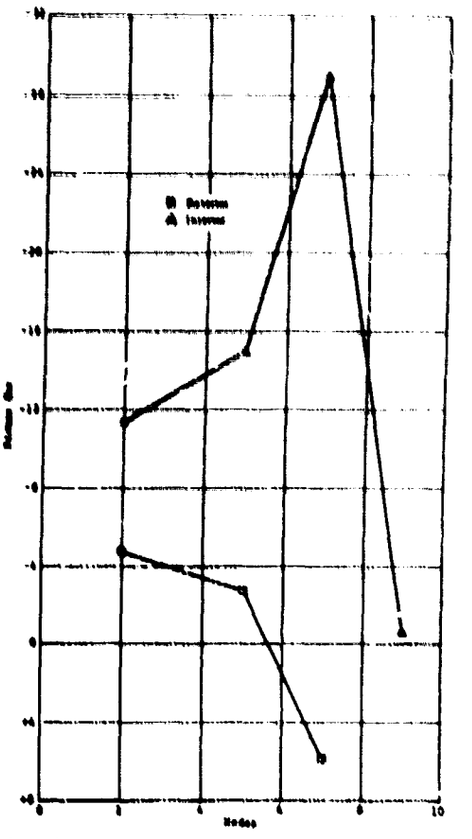

Figure 18b. Meridional stresses in bottom steel plate under 800 psi hydrostatic loading.

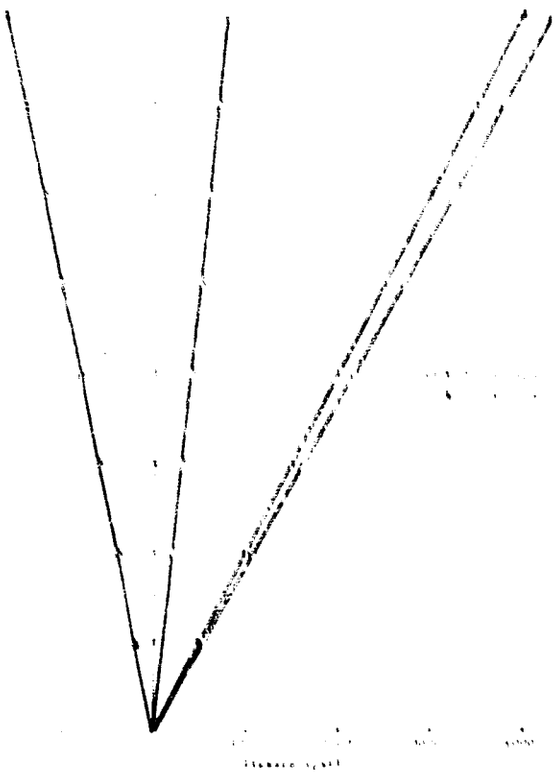

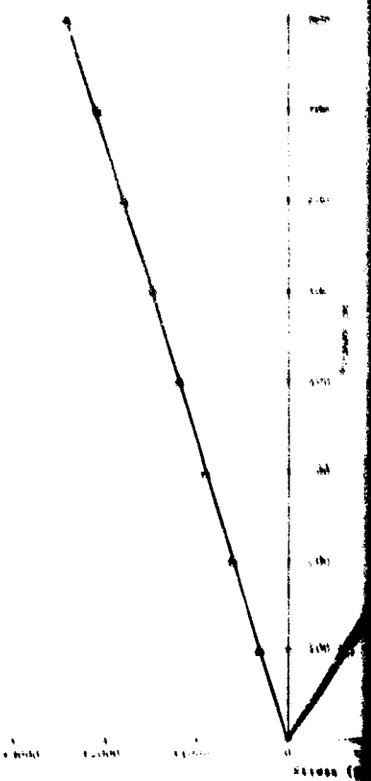

Figure 19d. Typical stresses on the equatorial region; Remotts 1/A to 800 psi

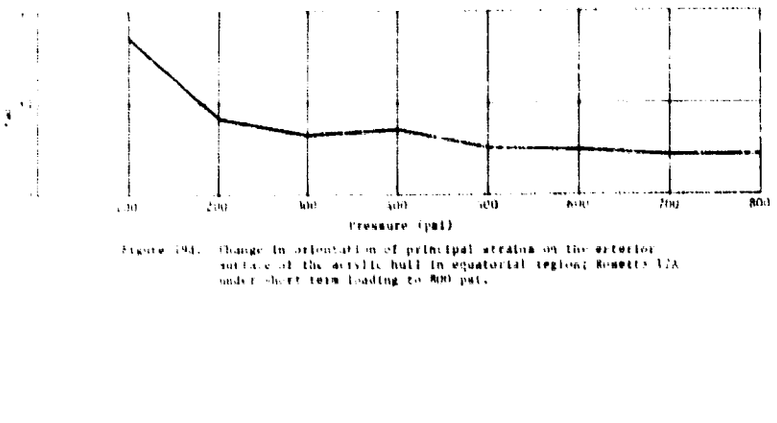

Figure 19d. Change in orientation of principal strains on the exterior surface of the acrylic hull in equatorial region; Remotts 1/A under short term loading to 800 psi.

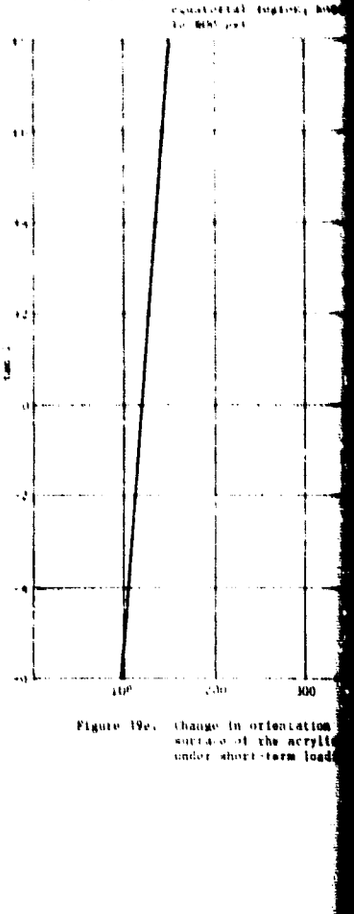

Figure 19e. Change in orientation surface of the acryli under short-term load

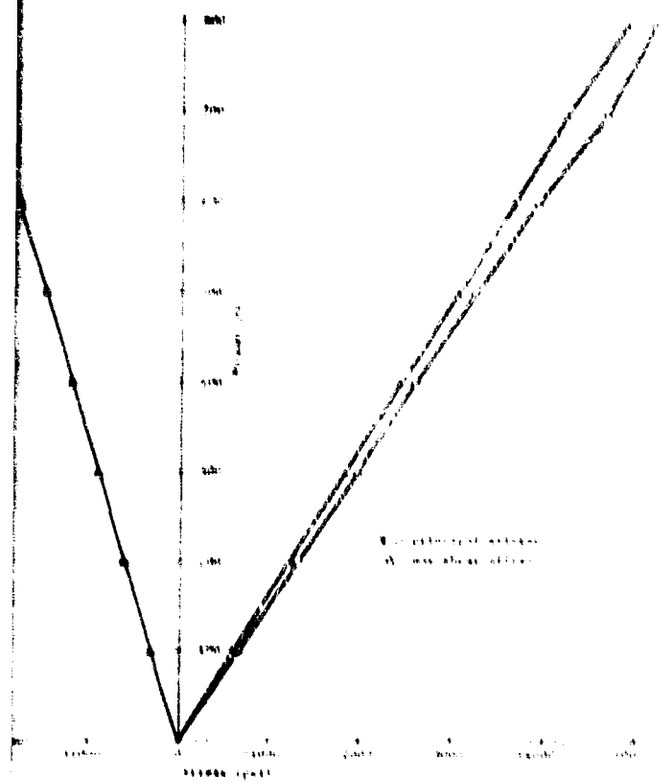

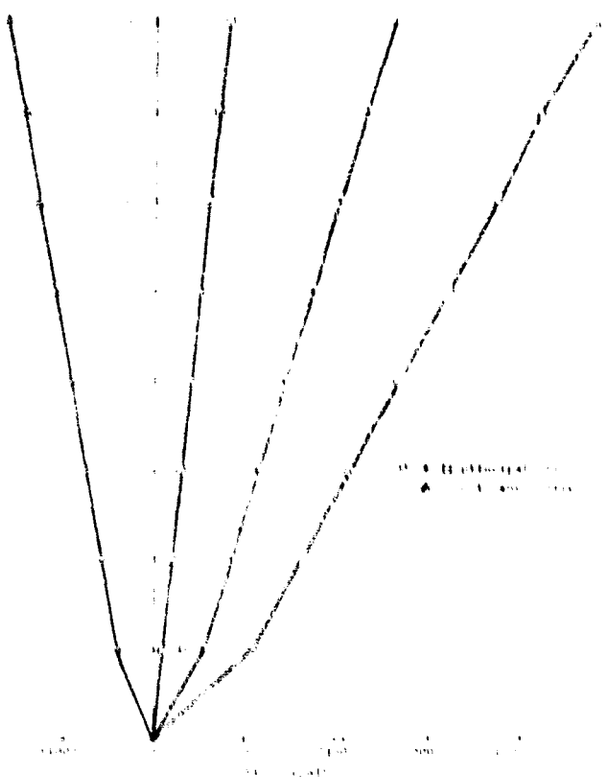

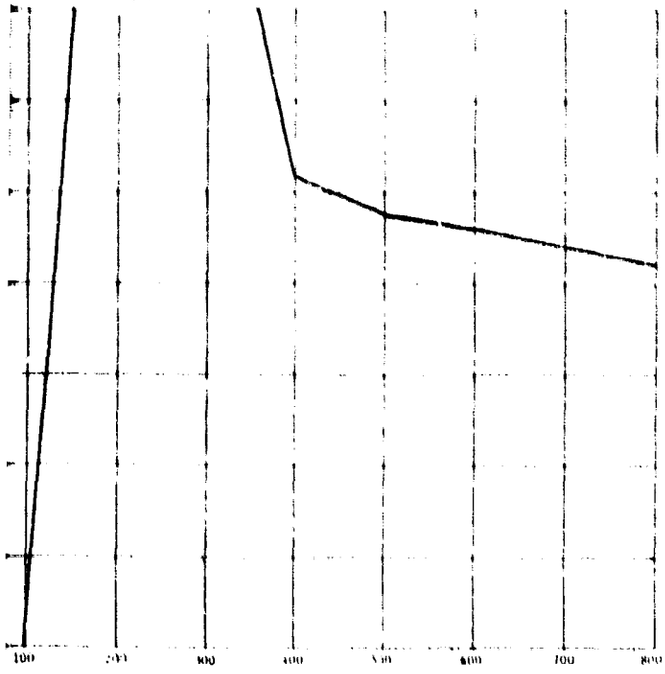

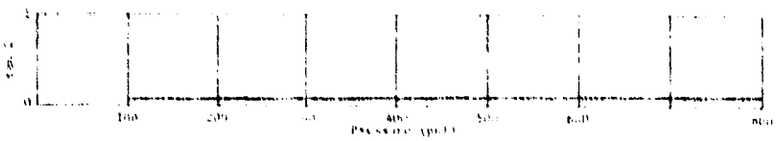

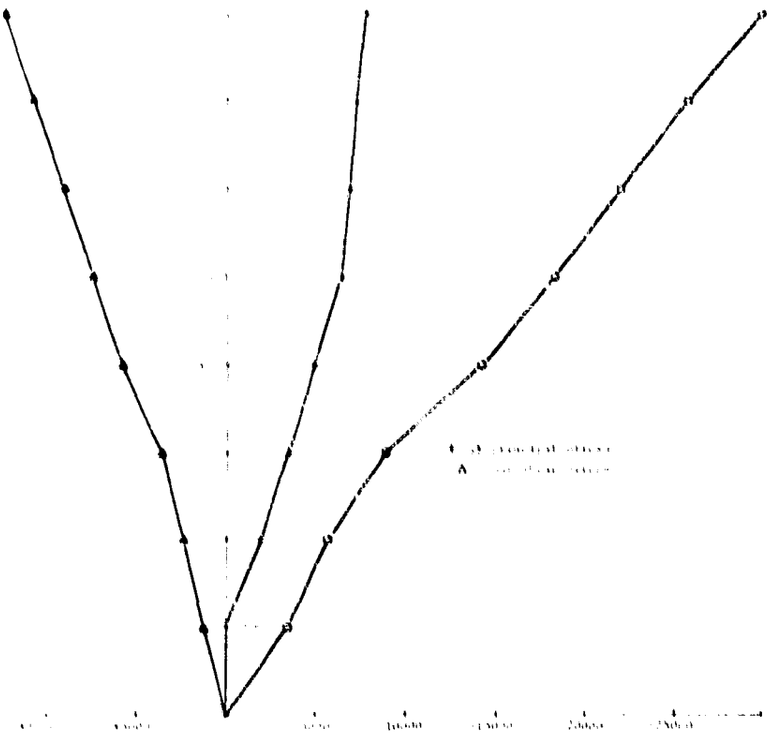

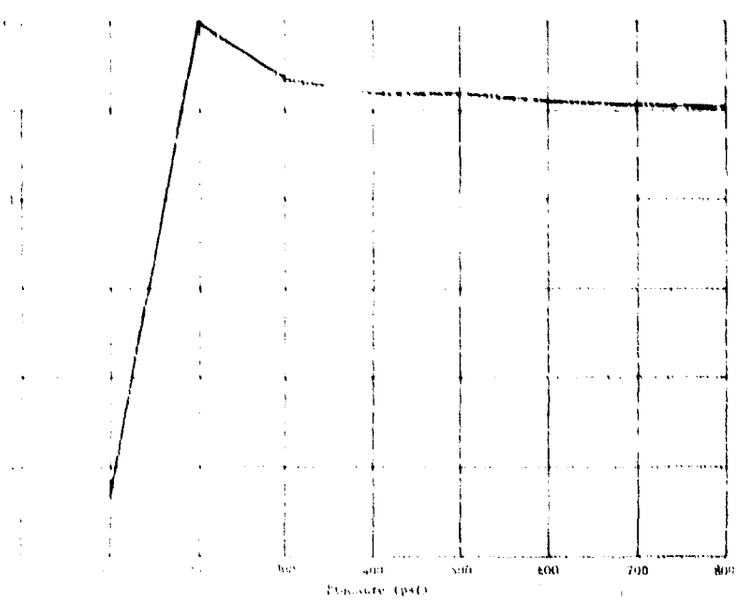
500
600
700
800

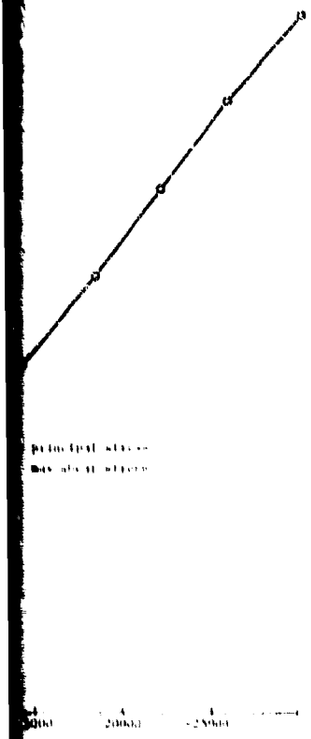

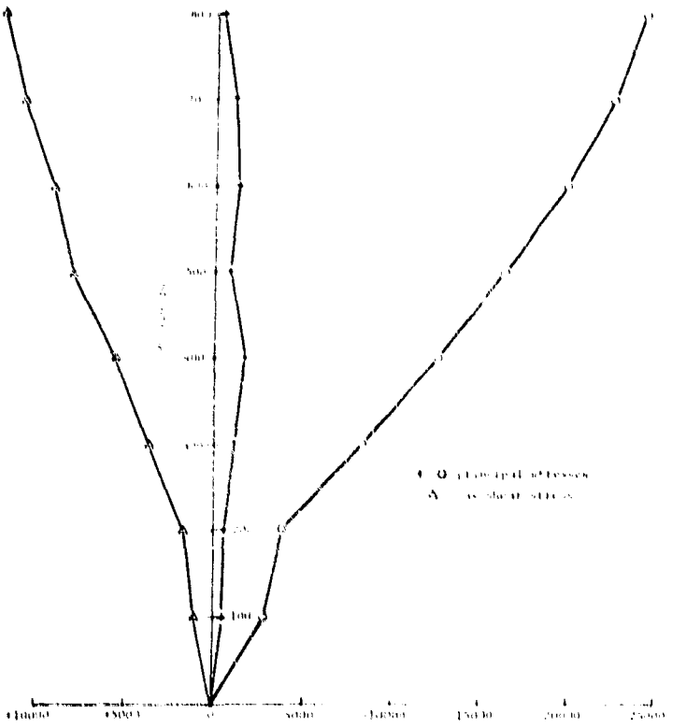

Figure 20b. Stresses on the interior surface of steel bottom plate flange; Rosette 48 under short-term loading to 800 psi

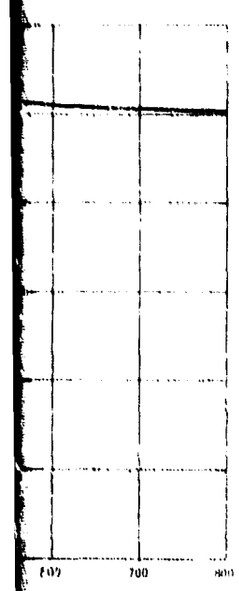

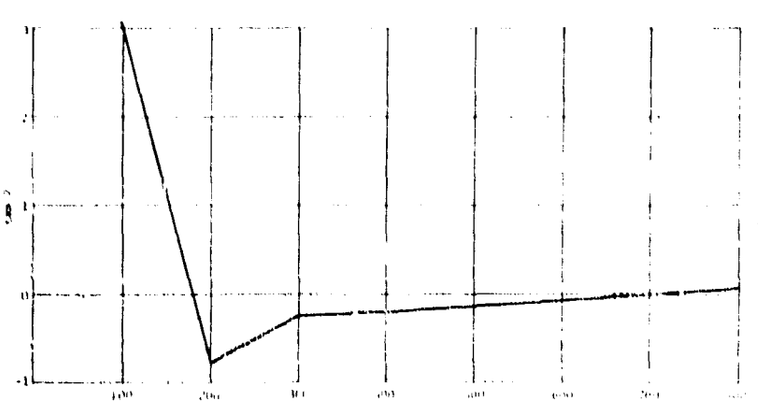

Figure 20c. Change in orientation of principal strains on the interior surface of the steel plate; Rosette 48 under short-term loading to 800 psi

BLANK PAGE

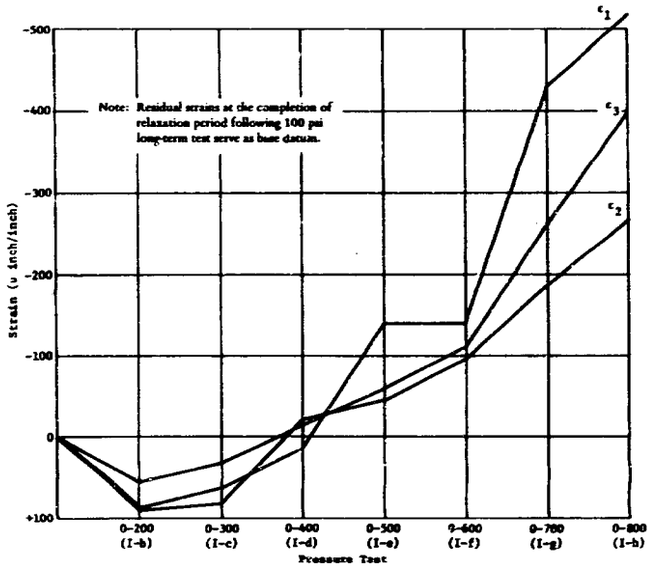

Figure 21a. Residual strains on the exterior of the hull in the equatorial region at the conclusion of each long-term test; Rosette 12A

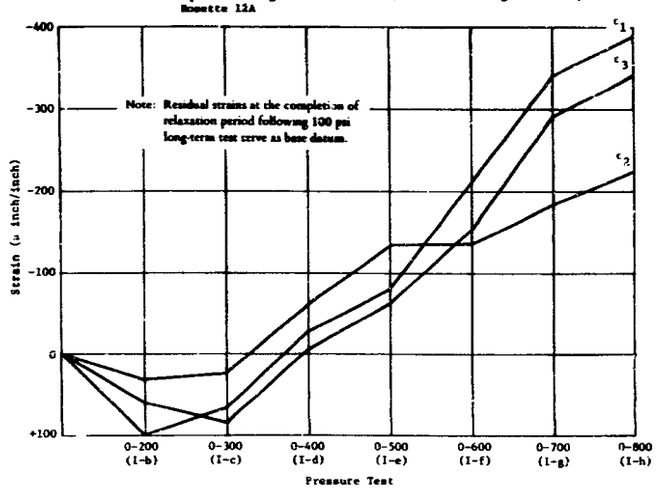

Figure 21b. Residual strains on the interior of the hull in equatorial region at the conclusion of each long-term test; Rosette 12B.

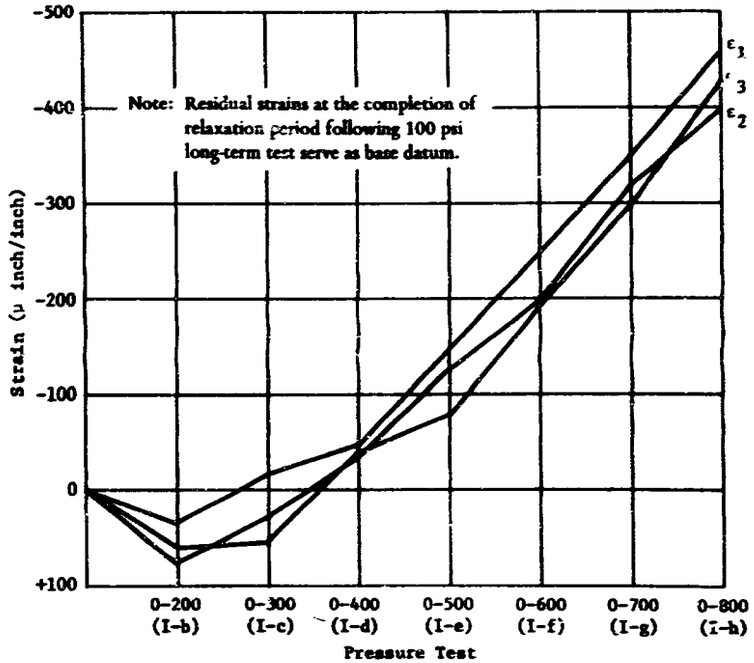

Figure 21c. Residual strains on the exterior of the acrylic hull at the polar penetration at the conclusion of each long-term test; Rosette 18A.

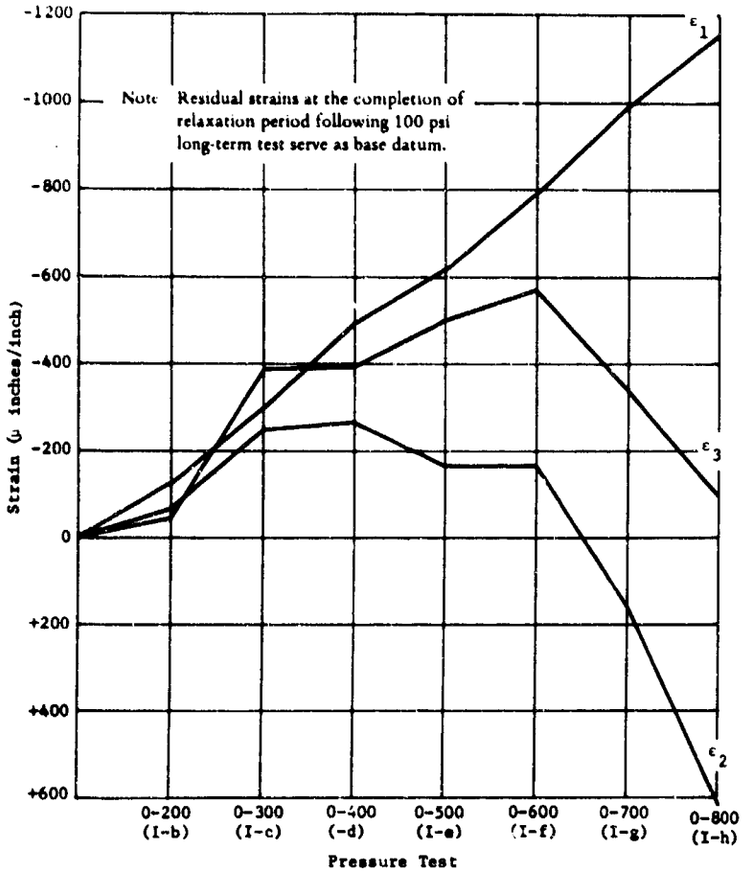

Figure 22a. Residual strains on the interior of bottom steel plate at the conclusion of each long-term test; Rosette 3B.

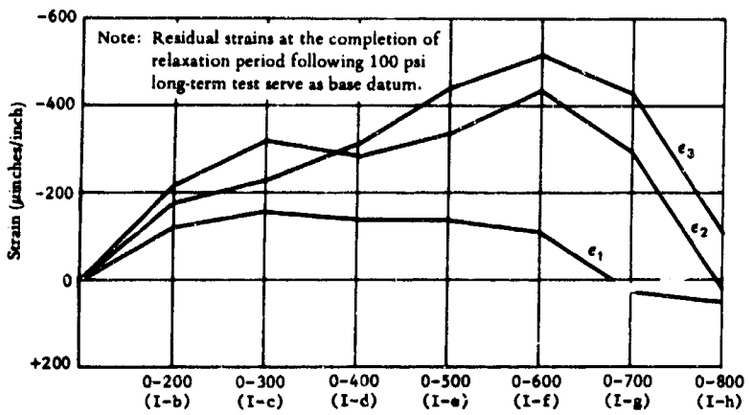

Figure 22b. Residual strains on the interior surface of steel bottom plate flange; Rosette 4B under short-term loading to 800 psi.

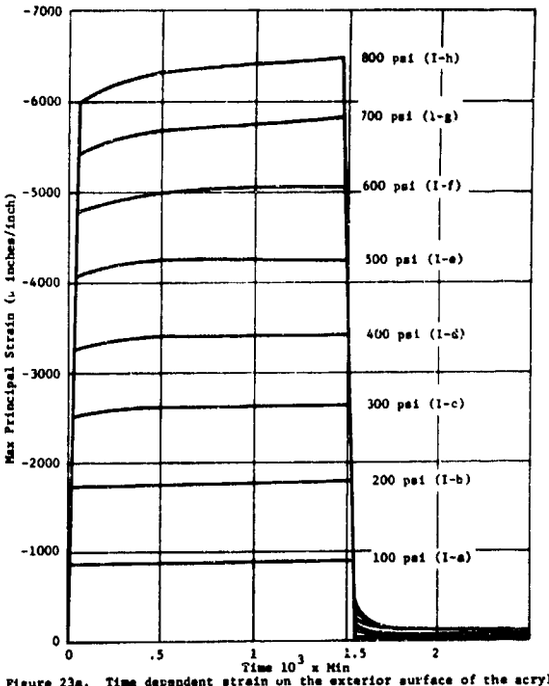

Figure 23a. Time dependent strain on the exterior surface of the acrylic hull in equatorial region; Rosette 12A under long-term hydrostatic loadings to different pressures.

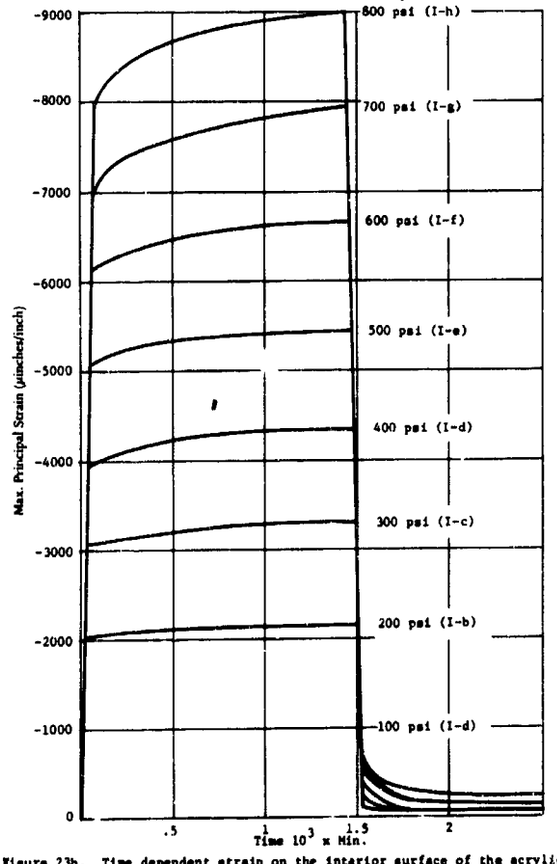

Figure 23b. Time dependent strain on the interior surface of the acrylic hull in the equatorial region; Rosette 12B under long-term hydrostatic loadings to different pressures.

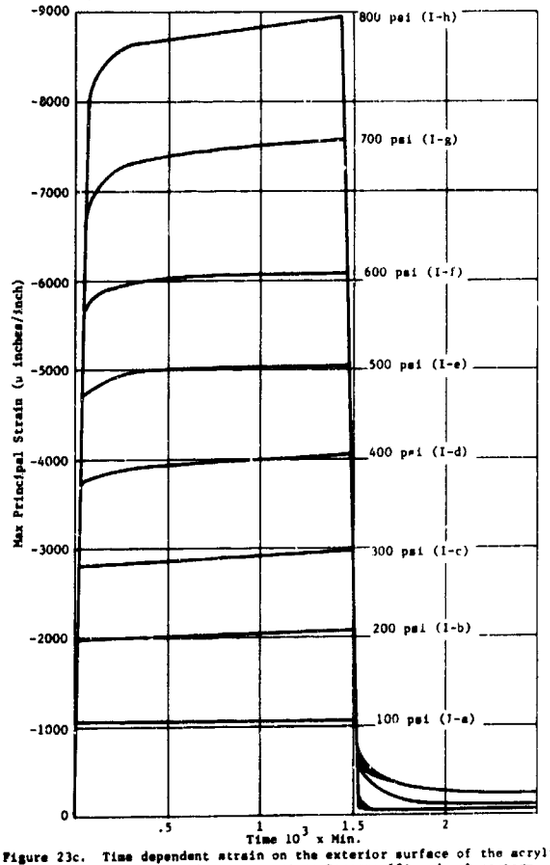

Figure 23c. Time dependent strain on the exterior surface of the acrylic hull near polar penetration; Rosette 18A under long-term hydrostatic loadings to different pressures.

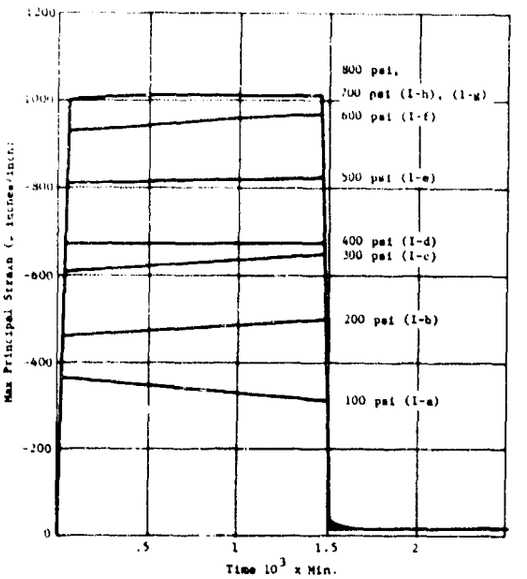

Figure 24a. Time dependent strain on the internal surfaces of the bottom steel plate; Rosette 3B under long-term hydrostatic loadings to different pressures.

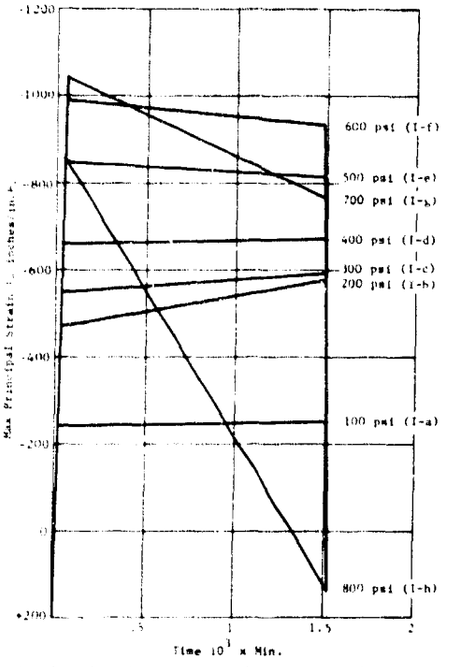

Figure 24b. Time dependent strain on the internal surface of the bottom steel plate flange; Rosette 4B under long-term hydrostatic loadings to different pressures.

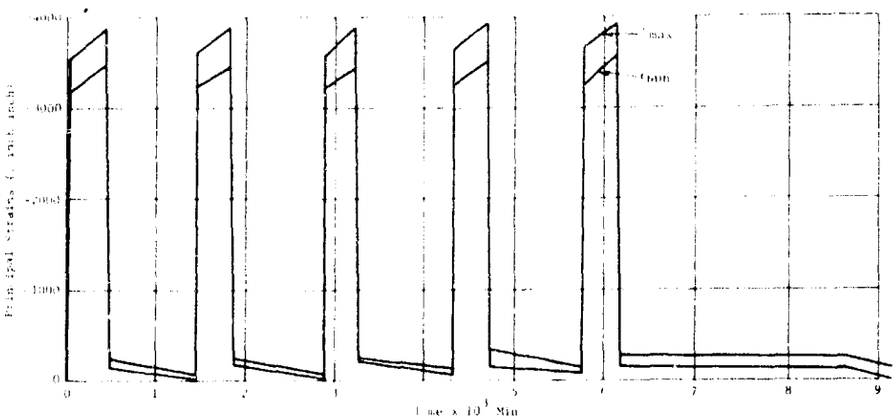

Figure 25a. Cyclic strains on the exterior surface of the acrylic hull in equatorial region; Rosette 10A under pressure cycles of 500 psi magnitude and 6-hour duration.

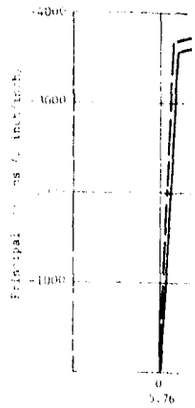

Figure 25c. Compa exter Roset 6-hou

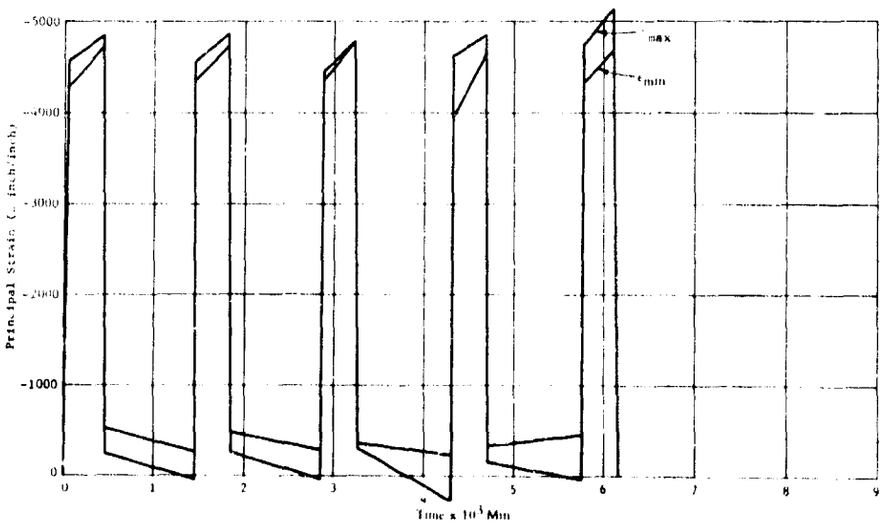

Figure 25b. Cyclic strains on the interior surface of the acrylic hull in equatorial region; Rosette 10B under pressure cycles of 500 psi magnitude and 6-hour duration.

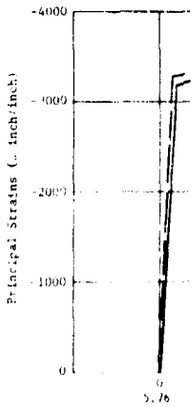

Figure 25d. Compa exter Roset 6-hou

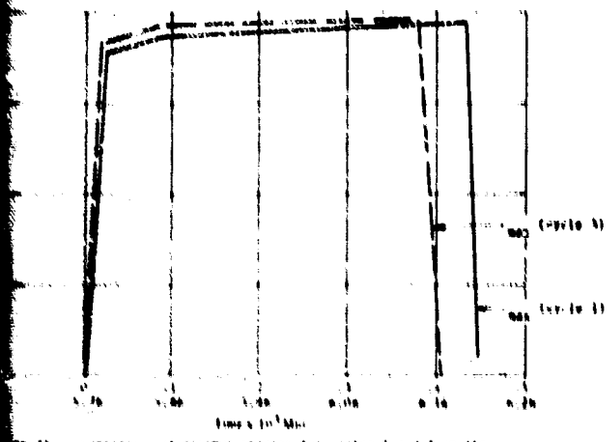

Figure 23c. [illegible] of maximum strains for cycles 1 and 3 on the exterior surface of the acrylic hull in equatorial region; Rocette 104 under pressure cycles of 500 psi magnitude and 6-hour duration.

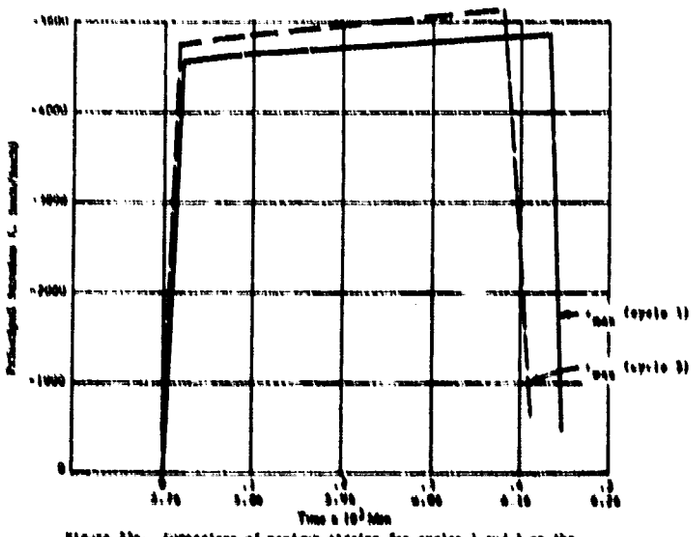

Figure 23b. Comparison of maximum strains for cycles 1 and 3 on the interior surface of the acrylic hull in equatorial region; Rocette 104 under pressure cycles of 500 psi magnitude and 6-hour duration.

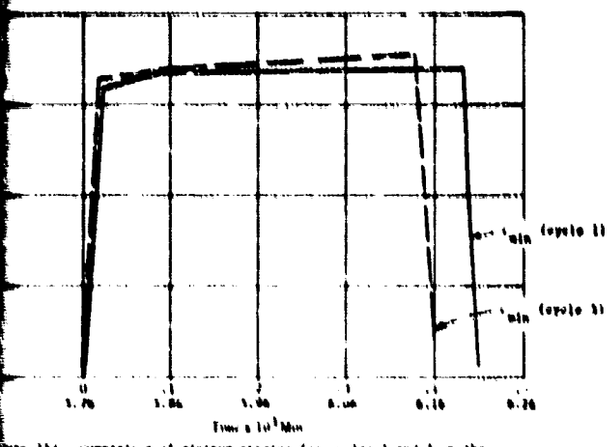

Figure 23d. [illegible] of minimum strains for cycles 1 and 3 on the exterior surface of the acrylic hull in equatorial region; Rocette 104 under pressure cycles of 500 psi magnitude and 6-hour duration.

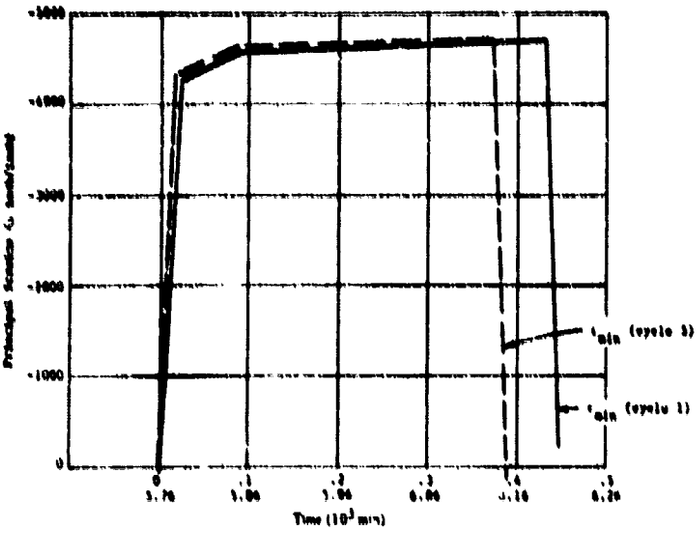

Figure 23a. Comparison of minimum strains for cycles 1 and 3 on the interior surface of the acrylic hull in equatorial region; Rocette 104 under pressure cycles of 500 psi magnitude and 6-hour duration.

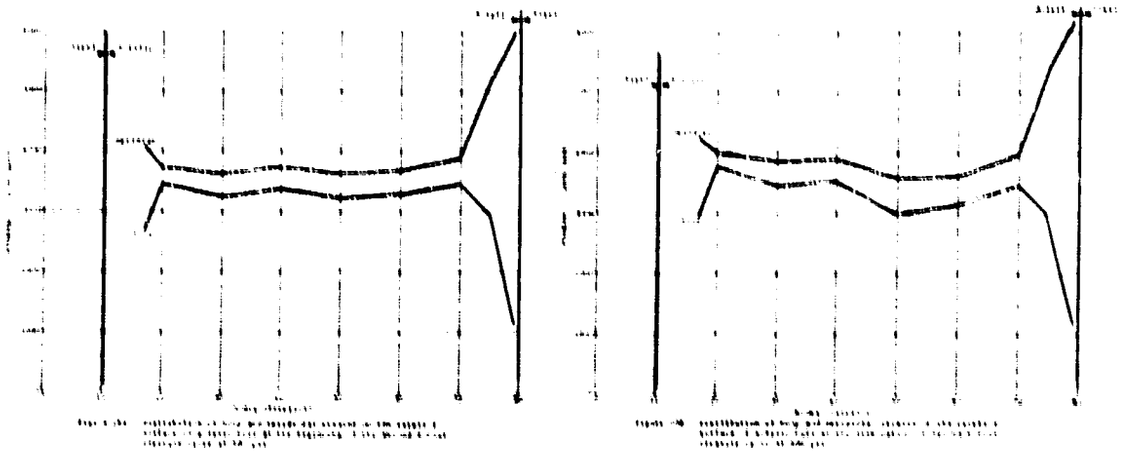

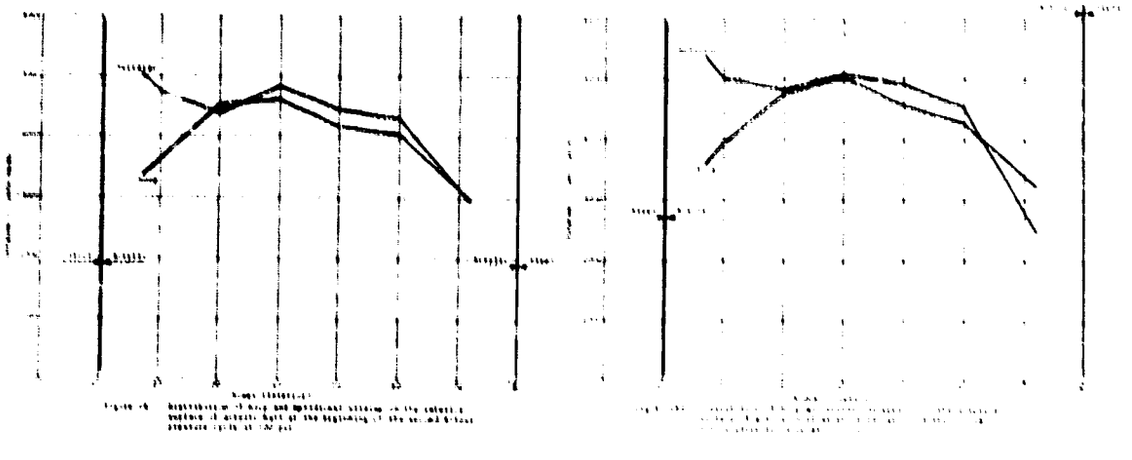

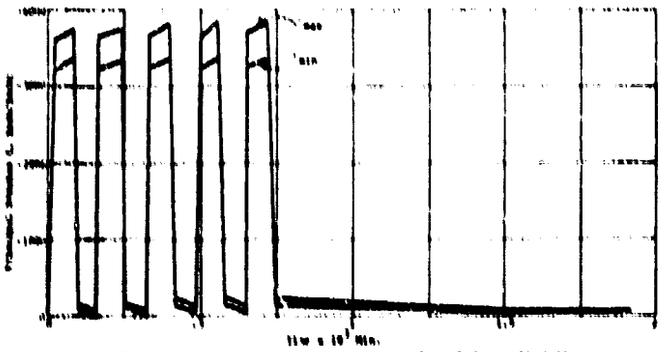

Figure 27a. Cyclic strains on the exterior surface of the acrylic hull in equatorial region; Rosette 10A under pressure cycles of 500 psi magnitude and 1-hour duration.

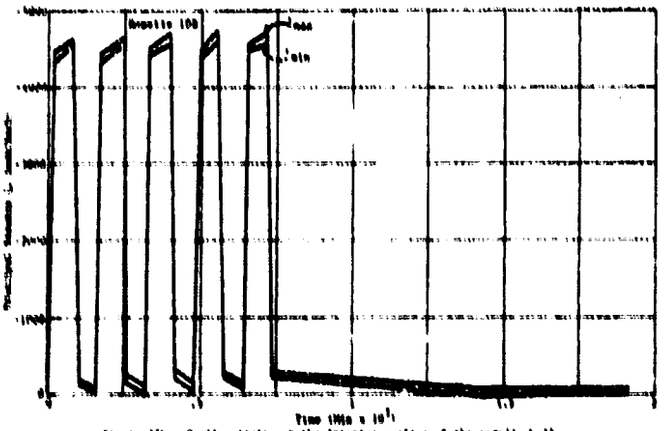

Figure 27b. Cyclic strains on the interior surface of the acrylic hull in equatorial region; Rosette 10A under pressure cycles of 500 psi magnitude and 1-hour duration.

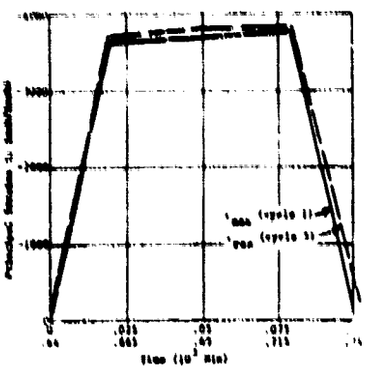

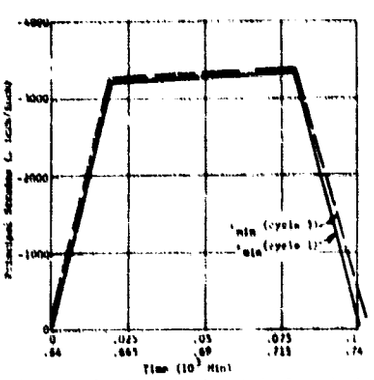

Figure 27c. Comparison of maximum and minimum strains for cycles 1 and 5 on the exterior surface of the acrylic hull in equatorial region; Rosette 10A under pressure cycles of 500 psi magnitude and 1-hour duration.

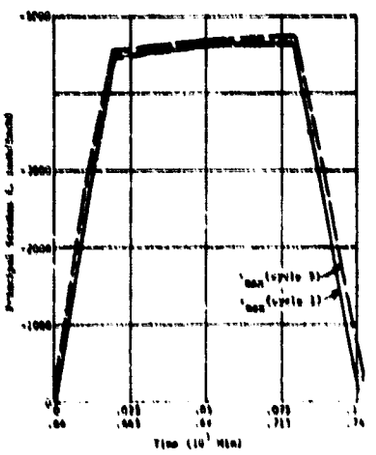

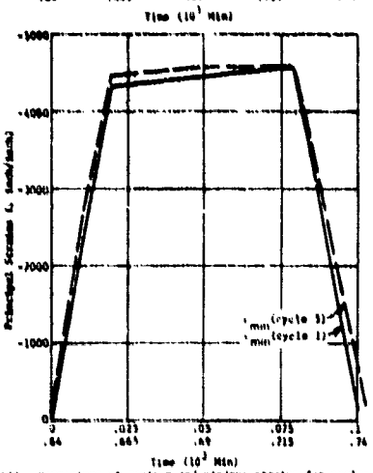

Figure 27d. Comparison of maximum and minimum strains for cycles 1 and 5 on the interior surface of the acrylic hull in equatorial region; Rosette 10A under pressure cycles of 500 psi magnitude and 1-hour duration.

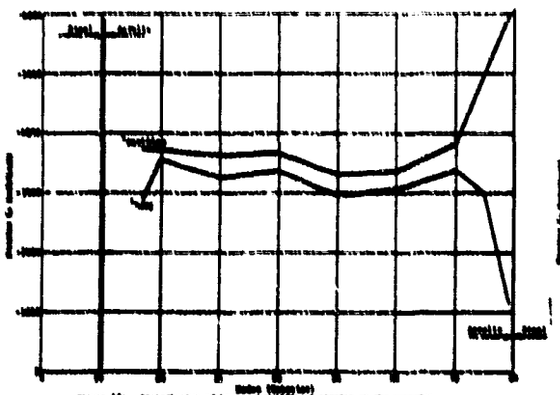

Figure 58a. Distribution of hoop and meridional stress on the exterior surface of acrylic ball at the beginning of the second 1-hour pressure cycle at 500 psi.

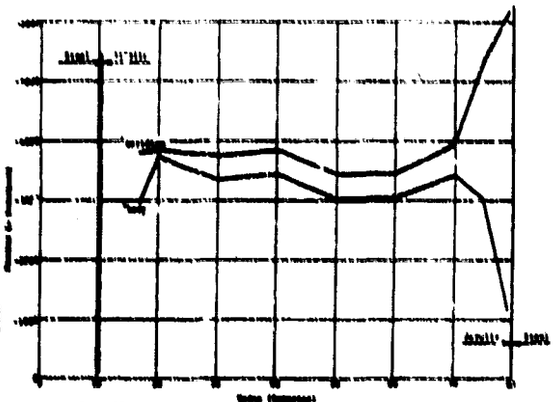

Figure 58b. Distribution of hoop and meridional stress on the exterior surface of acrylic ball at the termination of the second 1-hour pressure cycle at 500 psi.

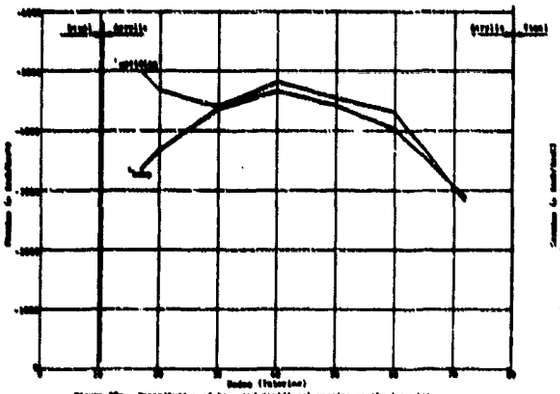

Figure 59a. Distribution of hoop and meridional stress on the interior surface of acrylic ball at the beginning of the second 1-hour pressure cycle at 500 psi.

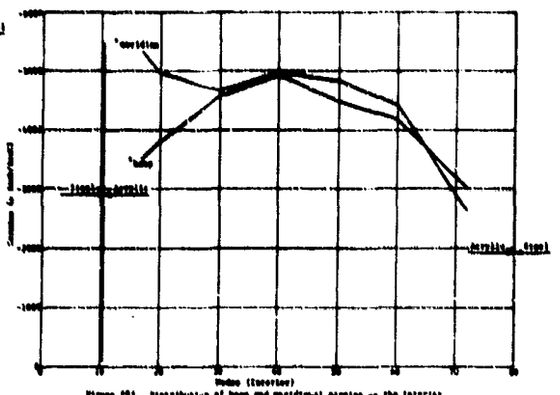

Figure 59b. Distribution of hoop and meridional stress on the interior surface of acrylic ball at the termination of the second 1-hour pressure cycle at 500 psi.

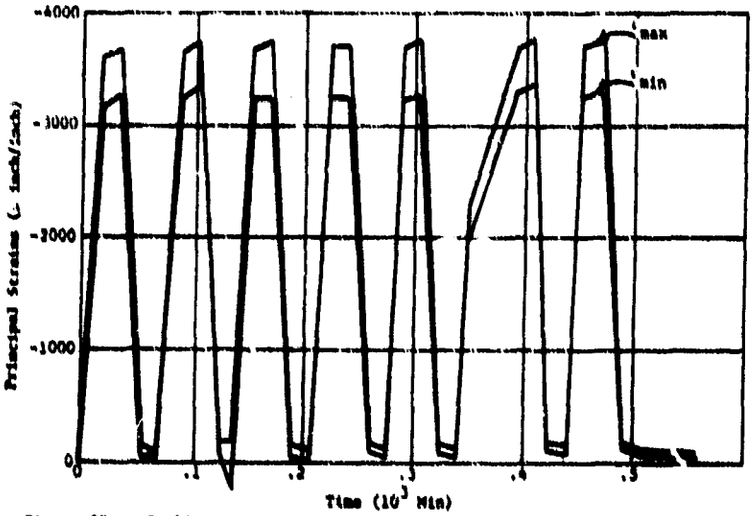

Figure 28a. Cyclic strains on the exterior surface of the acrylic hull in equatorial region; Rosette 10A under pressure cycles of 500 psi magnitude and 15-minute duration.

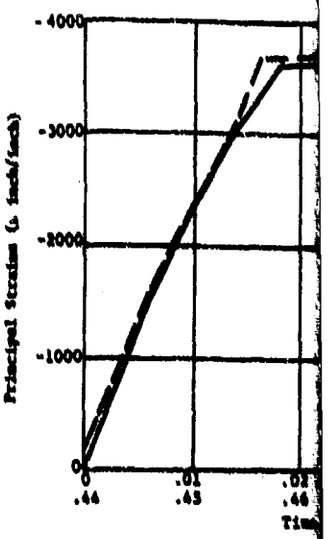

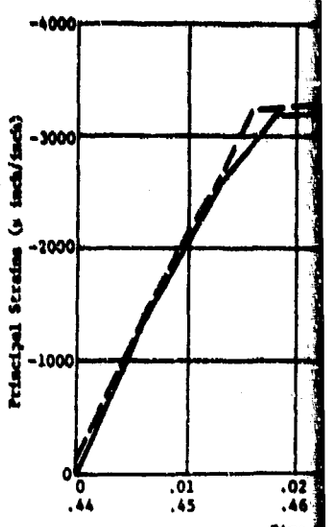

Figure 29c. Comparison of maximum
7 on the exterior su
region; Rosette 10A
tude and 15-minute d

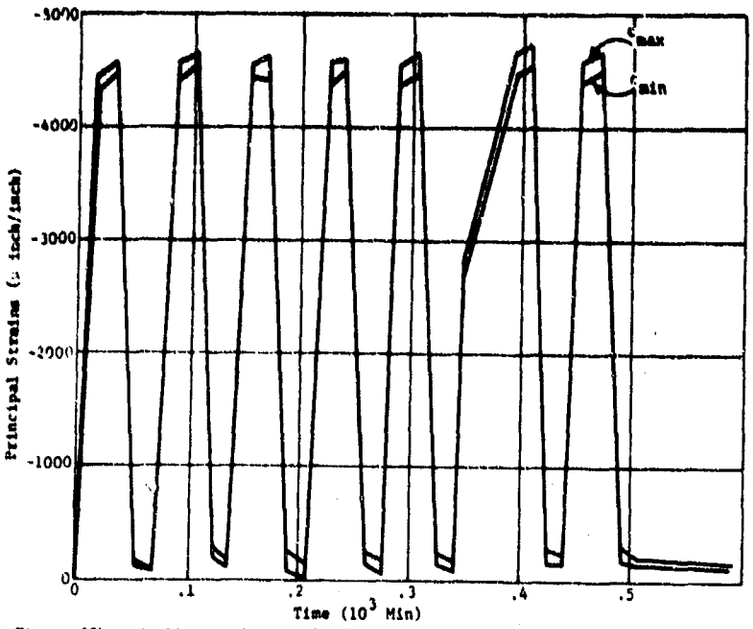

Figure 29b. Cyclic strains on the interior surface of the acrylic hull in equatorial region; Rosette 10B under pressure cycles of 5000 psi magnitude and 15-minute duration.

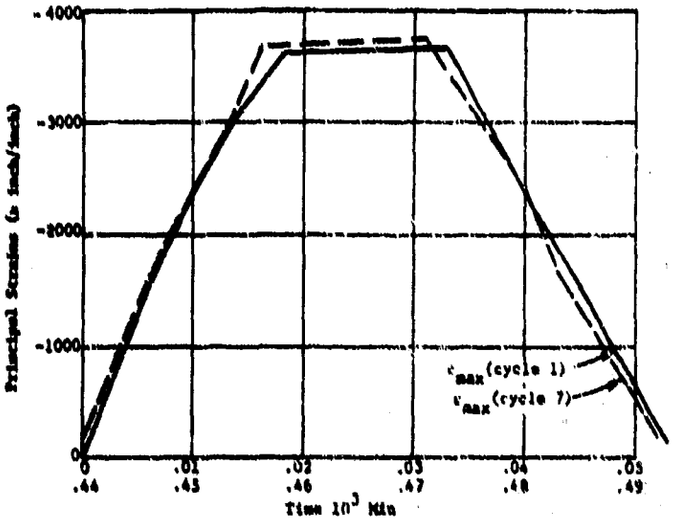

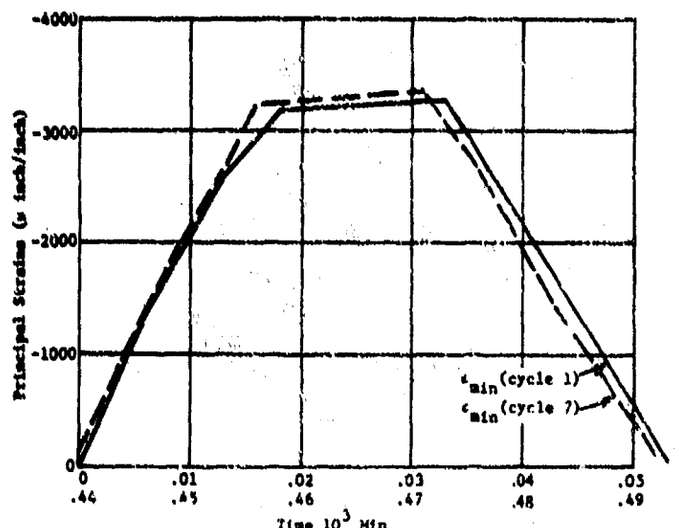

Figure 29c. Comparison of maximum and minimum strains for cycles 1 and 7 on the exterior surface of the acrylic hull in equatorial region; Rosette 10A under pressure cycles of 500 psi magnitude and 15-minute duration.

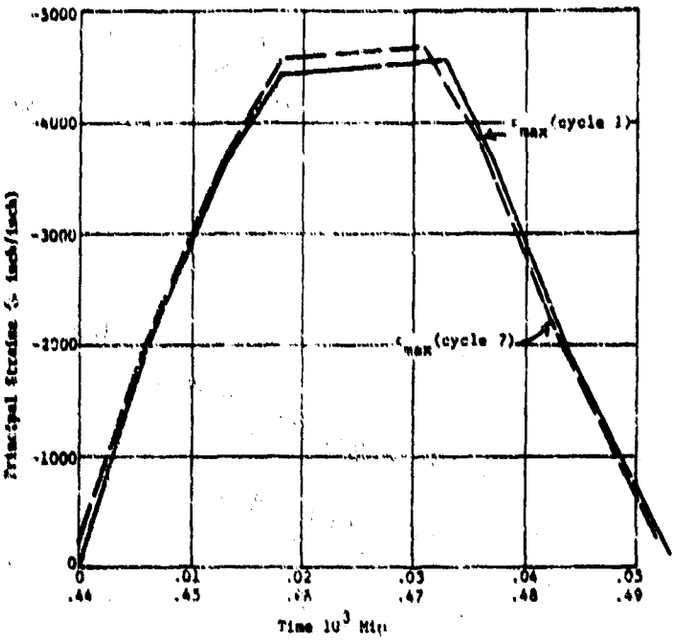

Figure 29d. Comparison of maximum strains for cycles 1 and 7 on the interior surface of the acrylic hull in equatorial region; Rosette 10B under pressure cycles of 500 psi magnitude and 15-minute duration.

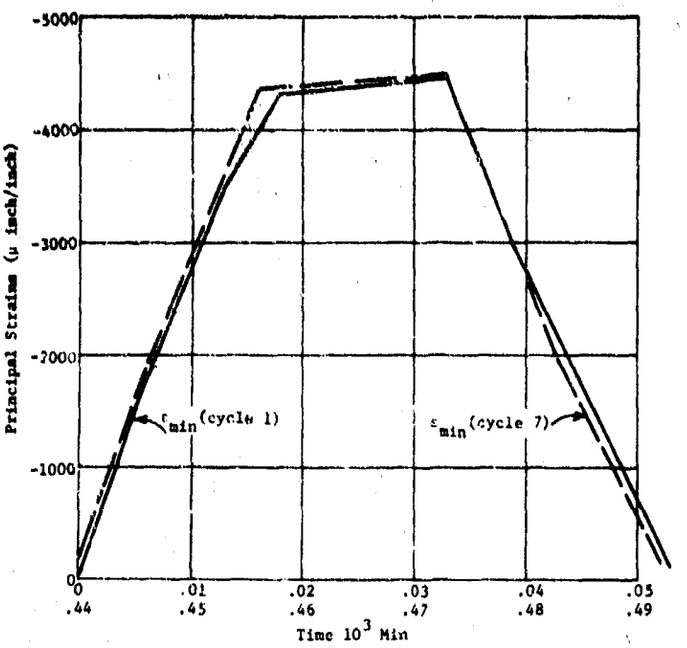

Figure 29e. Comparison of minimum strains for cycles 1 and 7 on the interior surface of the acrylic hull in equatorial region; Rosette 10B under pressure cycles of 500 psi magnitude and 15-minute duration.

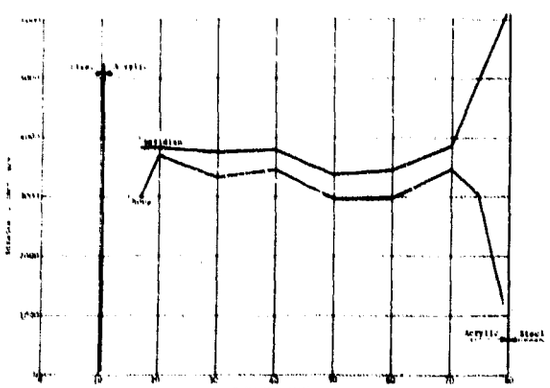

Figure 30b. Distribution of hoop and meridional strains on the exterior surface of acrylic hull at the termination of the second 15-minute pressure cycle at 900 psi.

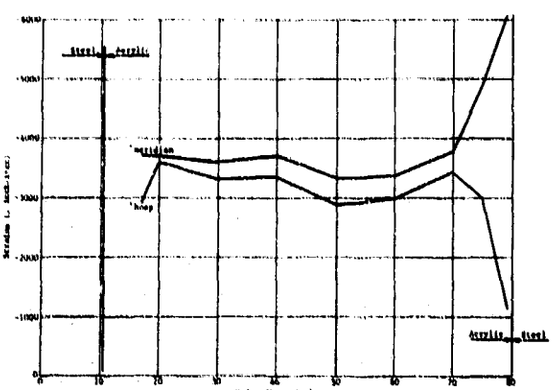

Figure 30a. Distribution of hoop and meridional strains on the exterior surface of acrylic hull at the beginning of the second 15-minute pressure cycle at 900 psi.

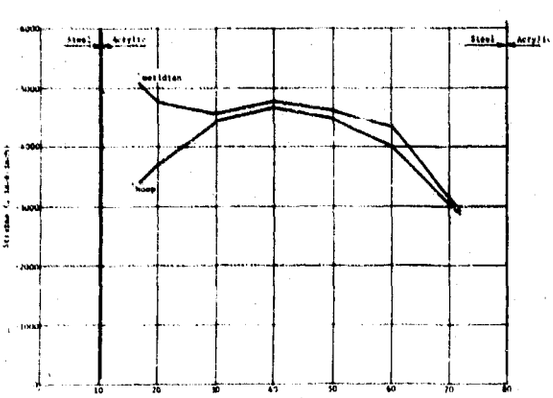

Figure 30c. Distribution of hoop and meridional strains on the interior surface of acrylic hull at the beginning of the second 15-minute pressure cycle at 900 psi.

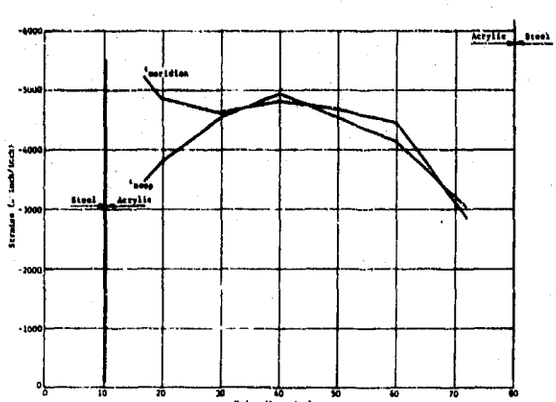

Figure 30d. Distribution of hoop and meridional strains on the interior surface of acrylic hull at the termination of the second 15-minute pressure cycle at 900 psi.

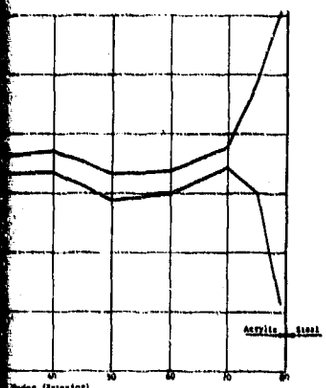

...dose (Exterior)
...op and meridional strains on the exterior
... hull at the beginning of the second
... cycle at 500 psi.

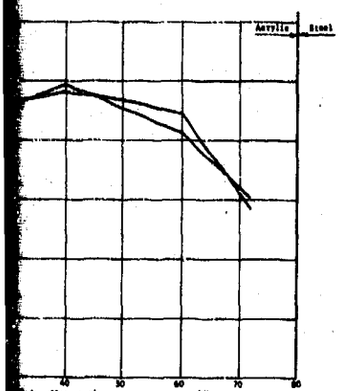

...dose (Interior)
...op and meridional strains on the interior
... hull at the termination of the second
... cycle at 500 psi.

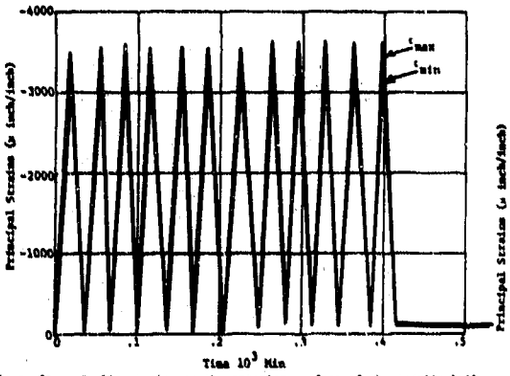

Figure 31a. Cyclic strains on the exterior surface of the acrylic hull in equatorial region; Rosette 10A under pressure cycles of 500 psi magnitude and 2-minute duration.

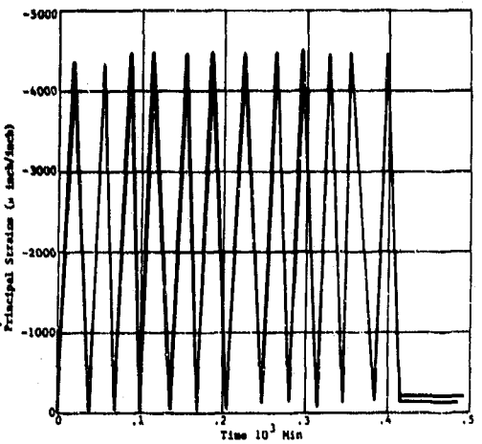

Figure 31b. Cyclic strains on the interior surface of the acrylic hull in equatorial region; Rosette 10B under pressure cycles of 500 psi magnitude and 2-minute duration.

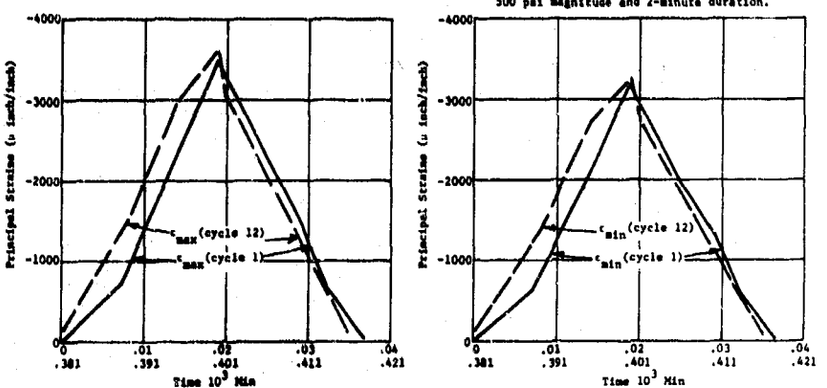

Figure 31c. Comparisons of maximum and minimum strains for cycles 1 and 12 on the exterior surface of the acrylic hull in equatorial region; Rosette 10A under pressure cycles of 500 psi magnitude and 2-minute duration.

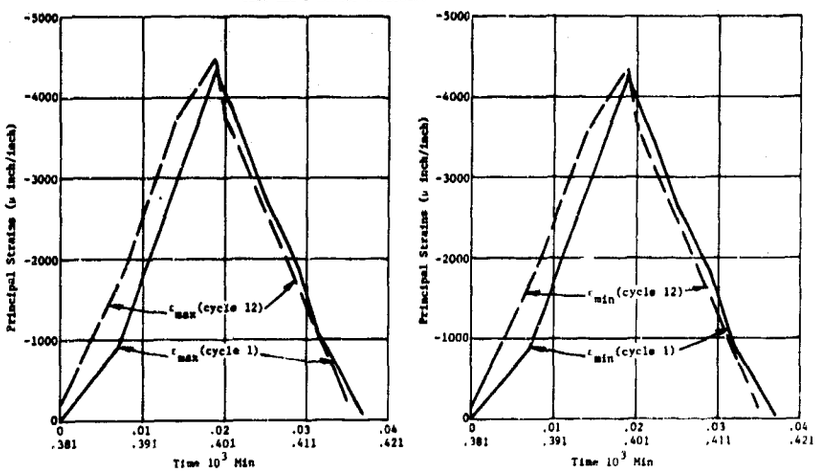

Figure 31d. Comparison of maximum and minimum strains for cycles 1 and 12 on the interior surface of the acrylic hull in equatorial region; Rosette 10B under pressure cycles of 500 psi magnitude and 2-minute duration.

BLANK PAGE

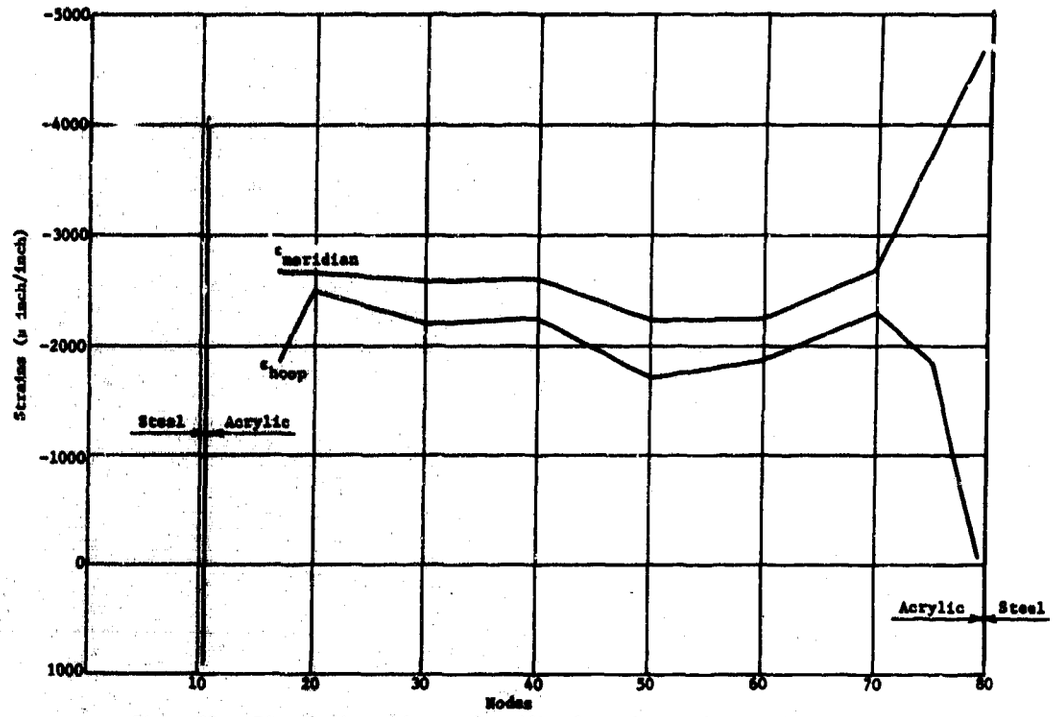

Figure 32a. Distribution of hoop and meridional strains on the exterior surface of acrylic hull at the midpoint of the second 2-minute pressure cycle at 500 psi.

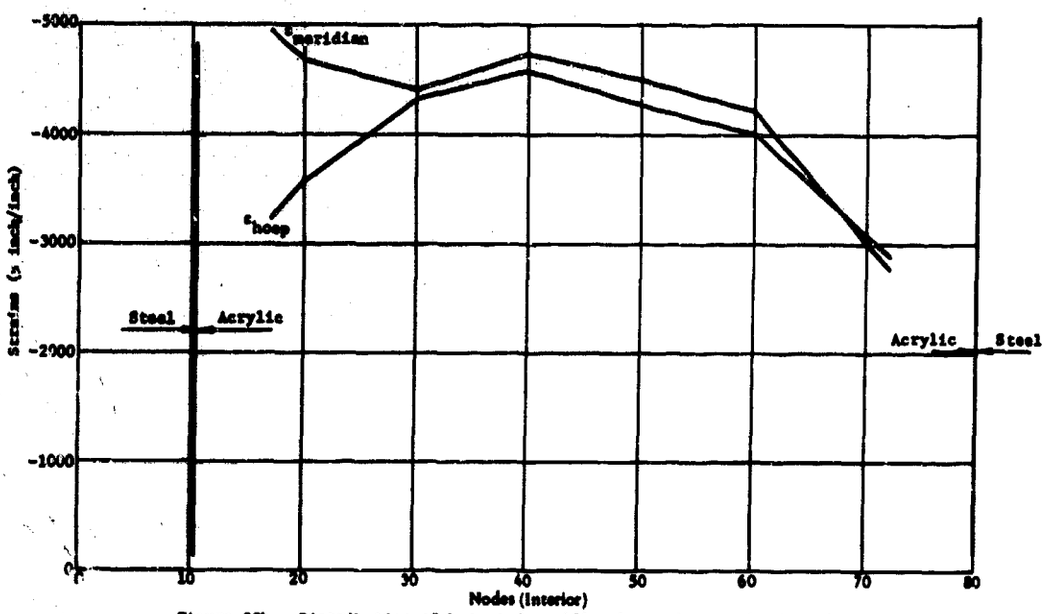

Figure 32b. Distribution of hoop and meridional strains on the interior surface of acrylic hull at the midpoint of the second 2-minute pressure cycle at 500 psi.

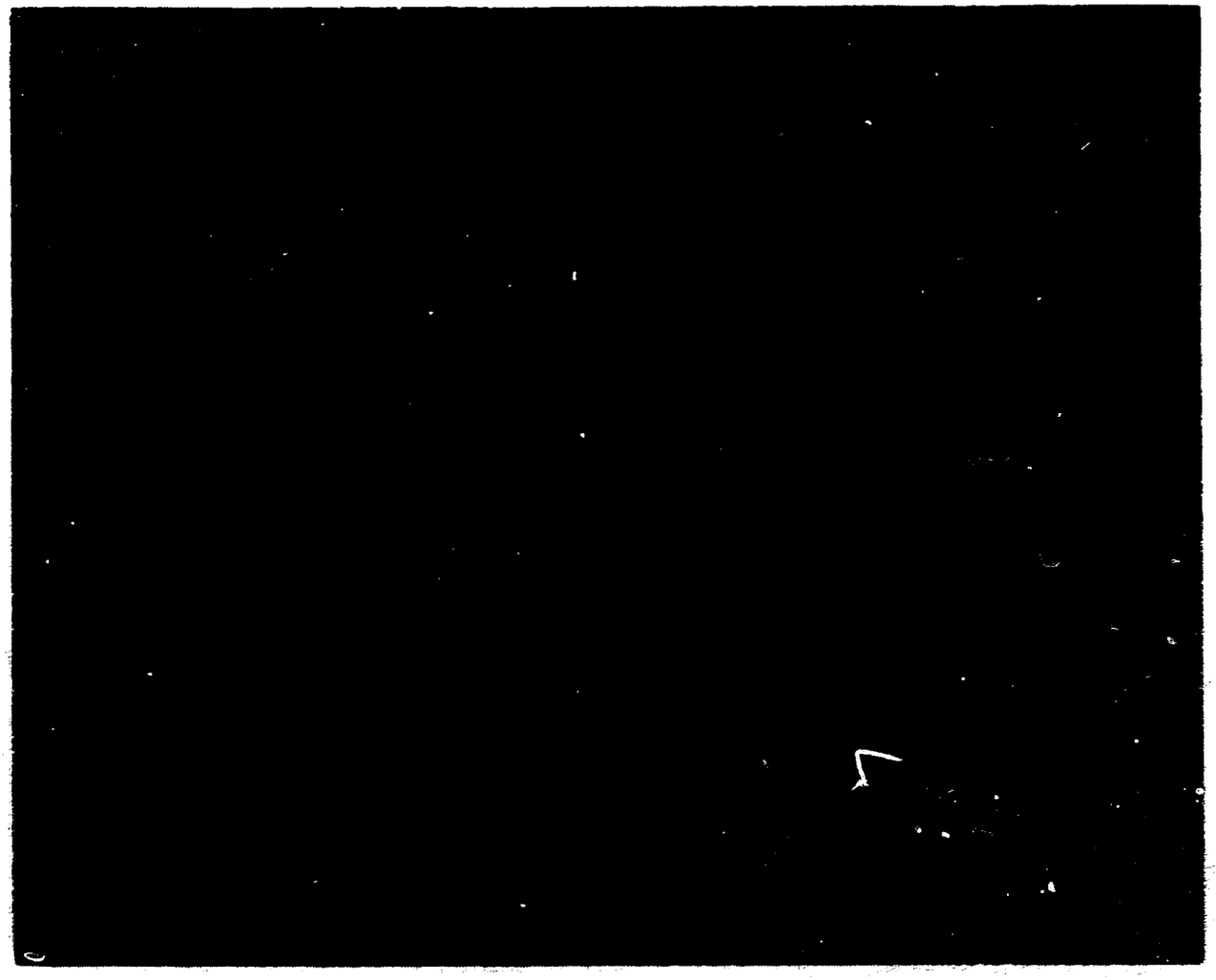

Figure 33. Fragments of imploded [redacted] capsule.

Figure 34a. Fragment from the polar pentagon in contact with the bottom steel penetration plate; exterior surface.

Figure 34b. Fragment from the polar pentagon in contact with the bottom steel penetration plate; interior surface. Note extensive spalling on the acrylic bearing surface in contact with steel plate.

Figure 35a. Fragment from the polar pentagon in contact with the top hatch ring; interior surface. Note only minor cracking on the acrylic bearing surface.

Figure 35b. Section through the top polar pentagon in contact with the top hatch ring. Note that the crack is in the plane of hull and approximately at middle of its thickness.

Figure 36a. Plastically deformed steel parts from the imploded NEMO hull.

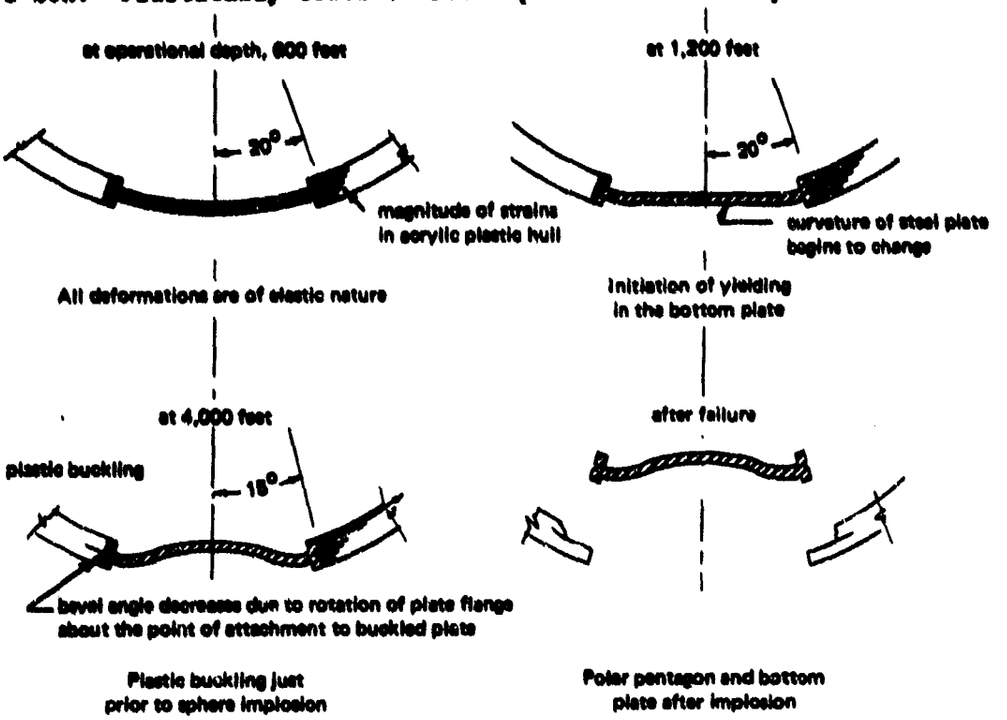

Figure 36b. Mechanism of spalling in the bottom polar acrylic pentagon reconstructed from observation of deformation in the bottom steel plate and fracture in the bottom polar acrylic pentagon.

Figure 37a. Typical air cavities in the NEMO joints bonded with PS-18 self-polymerizing adhesive.

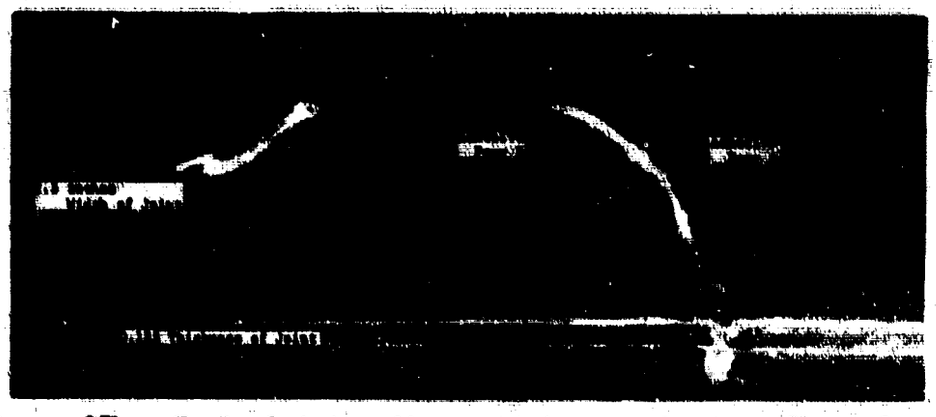

Figure 37b. Typical joint discontinuity at the interface of two successive adhesive pours.

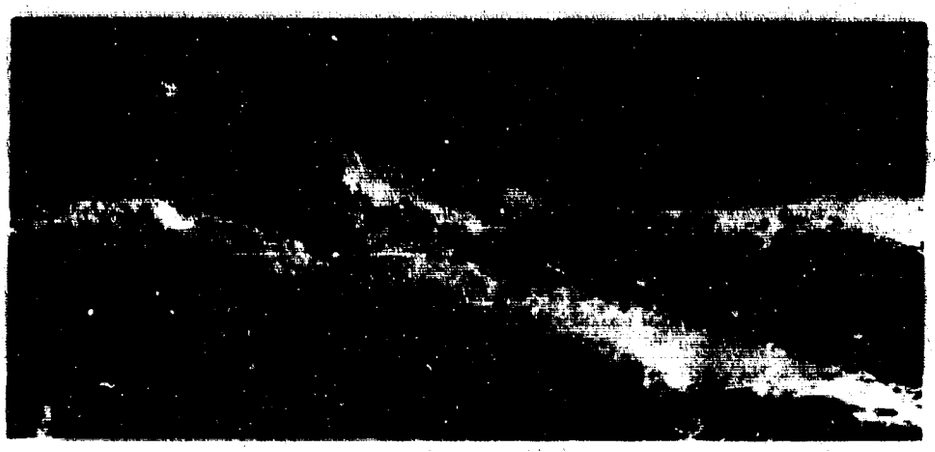

Figure 37c. Typical joint discontinuity that has been routed out and refilled with new adhesive. Note the presence of fine incipient cracks at the edges of the refilled cavity.

UNCLASSIFIED

Security Classification

DOCUMENT CONTROL DATA - R & D

(Security classification of title, body of abstract and indexing annotation must be entered when the overall report is classified)

1. ORIGINATING ACTIVITY (Corporate author) Naval Civil Engineering Laboratory Port Hueneme, California 93041	2a. REPORT SECURITY CLASSIFICATION UNCLASSIFIED 2b. GROUP

3. REPORT TITLE

THE SPHERICAL ACRYLIC PRESSURE HULL FOR HYDROSPACE APPLICATION; PART II - EXPERIMENTAL STRESS EVALUATION OF PROTOTYPE NEMO CAPSULE

4. DESCRIPTIVE NOTES (Type of report and inclusive dates)

5. AUTHOR(S) (First name, middle initial, last name)

J. D. Stachiw and K. L. Mack

6. REPORT DATE	7a. TOTAL NO. OF PAGES	7b. NO. OF REFS
October 1970	66	3

8a. CONTRACT OR GRANT NO.	9a. ORIGINATOR'S REPORT NUMBER(S)
b. PROJECT NO. YF 38.535.005.01.006	TN-1113
c.	9b. OTHER REPORT NO(S) (Any other numbers that may be assigned this report)
d.	

10. DISTRIBUTION STATEMENT

This document has been approved for public relase and sale; it's distribution is unlimited.

11. SUPPLEMENTARY NOTES	12. SPONSORING MILITARY ACTIVITY
	Naval Facilities Engineering Command

13. ABSTRACT

The prototype 66-inch diameter spherical hull of NEMO* with 2.5 inch wall thickness has been subjected to a series of hydrostatic tests under simulated hydrospace environment to determine its structural integrity. After repeated long term and cyclic tests in the 220 to 2400 foot depth range, the hull was tested to implosion at 4150 feet. The magnitude of strains measured on the hull during cyclic and long term loadings, as well as the short term implosion depth of 4150 feet indicate that the hull satisfies the 1000 foot design depth requirement and can be without any further tests incorporated into any man-rated system approved for operation in the 0 to 600 foot depth range.

* Naval Experimental Manned Observatory

DD FORM 1 NOV 65 1473 (PAGE 1)

S/N 0101-807-6801

UNCLASSIFIED

Security Classification

14 KEY WORDS	LINK A		LINK B		LINK C	
	ROLE	WT	ROLE	WT	ROLE	WT
Acrylic Resins						
Spheres						
Pressure vessels						
Deep water						
Underwater structures						
Hydrostatic pressure						
Failure						
Bucking						
Implosions						